

STATUS OF THESIS

Title of thesis

Characterization and Electrochemical Performance of Mesoporous Tin Phosphate based Anode for Lithium-Ion Cells.

I, **SITI MUNIRAH HASANALY**, hereby allow my thesis to be placed at the Information Resource Centre (IRC) of Universiti Teknologi PETRONAS (UTP) with the following conditions:

1. The thesis becomes the property of UTP
2. The IRC of UTP may make copies of the thesis for academic purposes only.
3. This thesis is classified as

☐

Confidential

☐

Non-confidential

If this thesis is confidential, please state the reason:

The contents of the thesis will remain confidential for _____ years.

Remarks on disclosure:

Endorsed by

Signature of Author

Siti Munirah Hasanaly
AMREC, SIRIM BERHAD
Lot 34, Jalan Hi-Tech 2/3
Kulim Hi-Tech Park
09000 Kulim, Kedah

Signature of Supervisor

Assoc. Prof. Dr. Muhammad Azmi Bustam
Department of Chemical Engineering
Universiti Teknologi PETRONAS

Date : _____

Date : _____

UNIVERSITI TEKNOLOGI PETRONAS

CHARACTERIZATION AND ELECTROCHEMICAL PERFORMANCE

OF MESOPOROUS TIN PHOSPHATE BASED ANODE

FOR LITHIUM-ION CELLS

by

SITI MUNIRAH HASANALY

The undersigned certify that they have read, and recommend to the Postgraduate Studies Programme for acceptance this thesis for the fulfilment of the requirements for the degree stated.

Signature:

Main Supervisor:

Assoc. Prof. Dr. Muhammad Azmi Bustam

Signature:

Head of Department:

Dr. Shuhaimi Mahadzir

Date:

CHARACTERIZATION AND ELECTROCHEMICAL PERFORMANCE
OF MESOPOROUS TIN PHOSPHATE BASED ANODE
FOR LITHIUM-ION CELLS

by

SITI MUNIRAH HASANALY

A Thesis

Submitted to the Postgraduate Studies Programme

as a Requirement for the Degree of

MASTER OF SCIENCE

CHEMICAL ENGINEERING

UNIVERSITI TEKNOLOGI PETRONAS

BANDAR SERI ISKANDAR,

PERAK

JULY 2010

DECLARATION OF THESIS

Title of thesis

Characterization and Electrochemical Performance of Mesoporous Tin Phosphate based Anode for Lithium-Ion Cells.

I, SITI MUNIRAH HASANALY, hereby declare that the thesis is based on my original work except for quotations and citations which have been duly acknowledged. I also declare that it has not been previously or concurrently submitted for any other degree at UTP or other institutions.

Witnessed by

Signature of Author

Siti Munirah Hasanaly
AMREC, SIRIM BERHAD
Lot 34, Jalan Hi-Tech 2/3
Kulim Hi-Tech Park
09000 Kulim, Kedah

Signature of Supervisor

Assoc. Prof. Dr. Muhammad Azmi Bustam
Department of Chemical Engineering
Universiti Teknologi PETRONAS

Date : _____

Date : _____

ACKNOWLEDGEMENTS

I would like to thank my supervisor, Assoc. Prof. Dr. Mohamad Azmi Bustam @Khalil for introducing me to the intriguing world of rechargeable Lithium-ion battery. He has provided insightful, technical guidance during the course of this research and has also taught me the finer points of scientific analysis and polished my analytical thinking skills. Special thanks go to Pn. Suhana Shahbudin from the Chemical Engineering Department and Pn. Kamaliah Mohd from the Postgraduate Office for facilitating administrative matters concerning my progress reports and presentations.

I am grateful to the management of AMREC, SIRIM Berhad in Kulim, Kedah for providing me access to research facilities available in the laboratories of AMREC, SIRIM Berhad. I thank Dr. Kamisah Mohammad Mahbor and En. Abdul Hakim Hashim for providing stimulating discussion on the subject of electrochemistry. Gratitude goes to technical staff that has helped me with my experiments; En. Sahhidan Daud for XRD measurements, En. Muhd Hazri Othman for physisorption measurements, En. Badrol Hisham Sihalmi for FESEM analysis and En. Mohd Fadzli Hashim together with En. Juri Che Hat for electrochemical cell assembly.

Words cannot express the unwavering support my family has given me all these years. My deepest gratitude for my father, Hasanaly Abdul Kader who has always supported my intellectual growth. A big thank you to my greatest supporters, my siblings; Wajiha Hasanaly, Bunyamin Hasanaly, Nusrat Hasanaly and Nahemah Hasanaly for always cheering me on in everything that I do. Most of all, I thank my husband, Mat Tamizi Zainuddin and my children, Lukman Hakeem and Nur Iman Zara for patiently enduring the high and lows during the course of my study and for providing me the inspiration, strength, understanding and love that enabled the completion of this thesis.

DEDICATION

For my husband, Mat Tamizi Bin Zainuddin for without his endless support and encouragement, this thesis would never be realized.

For my children, Lukman Hakeem and Nur Iman Zara who inspire me to greater heights.

ABSTRACT

The growth in demand for extra power in rechargeable batteries has encouraged intense research to develop new materials with even higher capacities. The main focus of this work is to investigate the electrochemical characteristics of mesoporous tin phosphate as alternative anode host material for Li-ion batteries. Mesoporous tin phosphate was synthesized based on a surfactant templating method, where an anionic surfactant, sodium dodecyl sulfate, was used as the structure directing agent and tin (IV) chloride (SnCl_4) as the inorganic source. The synthesized powder was characterized by means of thermal, X-ray diffraction (XRD), nitrogen gas sorption and scanning electron microscope (FE-SEM) techniques. The surfactant synthesized tin phosphate (SnP_2O_7) calcined from 200-400°C exhibited amorphous, mesoporous characteristics. Average pore size distribution obtained for the mesoporous SnP_2O_7 was around 10-18 nm. The electrochemical behaviour of the synthesized tin phosphate anode was studied using a combination of electrochemical analysis from cyclic voltammogram and differential capacity plots. The mesoporous SnP_2O_7 anode exhibited electrochemical reactions with lithium within the potential range of 0-2 V vs. Li^+/Li as indicated by cyclic voltammetry analysis. These reactions consist of the irreversible reaction to form lithium phosphate matrix phases and the reversible reaction of lithium insertion and extraction upon subsequent charging and discharging. The formation of the irreversible lithium phosphate phase leads to substantial losses of more than 50% in lithium ion storage capacity upon the first discharge cycle. The mesoporous SnP_2O_7 anodes performed averagely better in terms of delivering higher discharge capacity when compared to that of the non-mesoporous SnP_2O_7 anodes. A narrower cutoff operating voltage range within 0-1.2 V exhibited better galvanostatic cycling performance of the mesoporous SnP_2O_7 calcined at 400°C for 2 hours. This anode delivered a reversible discharge capacity (lithium ion storage capacity) of 780 mAh/g upon the second cycle and retained 134 mAh/g upon the fiftieth cycle. The mesoporous structure helps to absorb some volume change of the

tin particles during lithium alloying and de-alloying process thus improving cyclability.

ABSTRAK

Pasaran bateri cas semula kini menyaksikan permintaan yang semakin meningkat dalam bateri cas semula yang dapat memberikan kuasa yang lebih tinggi. Ini telah menggiatkan usaha penyelidikan yang lebih intensif dalam mengenalpasti dan membangunkan bahan-bahan baru yang berpotensi memberikan kapasiti yang lebih tinggi untuk diaplikasikan dalam bateri cas semula. Thesis ini menumpu kepada kajian pencirian sifat elektrokimia bahan mesoporos tin phosphat sebagai alternatif bahan anod dalam bateri cas semula lithium-ion. Mesoporos tin phosphat disintesis menggunakan kaedah pencontoh surfaktan ('surfactant templating method') di mana surfaktan anionik, sodium dodecyl sulfat digunakan sebagai agen pengarah struktur manakala precursor inorganik yang digunakan adalah tin (IV) klorida (SnCl_4). Serbuk yang dihasilkan dicirikan menggunakan teknik analisa termal, teknik pembelauan sinar-X (XRD), teknik penyerapan gas Nitrogen dan teknik imbasan elektron mikroskop (FESEM). Serbuk SnP_2O_7 yang dihasilkan dengan menggunakan surfaktan yang dibakar pada suhu 200-400°C mempunyai ciri-ciri amorfus dan mesoporos. Purata taburan saiz liang yang diperolehi dari serbuk SnP_2O_7 yang terhasil adalah sekitar 10-18 nm. Mekanisma tindakbalas elektrokimia bahan anod ini dikaji menggunakan kombinasi teknik analisis elektrokimia seperti kitaran voltamogram (cyclic voltammogram) and plot perbezaan kapasiti (yakni perubahan kapasiti dengan perubahan bezaupaya sel). Bahan anod mesoporos tin phosphat menunjukkan tindakbalas elektrokimia dengan lithium dalam julat bezaupaya 0-2V vs. Li^+/Li berdasarkan analisis kitaran voltamogram. Tindakbalas elektrokimia ini merujuk kepada tindakbalas tak berbalik membentuk fasa matrik lithium phosphat dan tindakbalas berbalik penyisipan dan pengekstrakan ion lithium semasa proses cas dan discas. Pembentukan fasa tak berbalik lithium phosphat ini menyebabkan kehilangan kapasiti muatan ion lithium yang amat besar iaitu lebih 50%, semasa proses discas dalam kitaran pertama. Julat operasi bezaupaya yang lebih kecil sekitar 0-1.2V dapat memberikan prestasi kitaran galvanostatik yang lebih baik bagi bahan mesoporos tin

phosphat yang dibakar pada suhu 400°C selama 2 jam. Bahan anod ini berupaya menghasilkan kapasiti discas (kapasiti muatan ion lithium) berbalik sebanyak 780 mAh/g pada kitaran yang kedua dan mampu mengekalkan kapasiti sebanyak 134 mAh/g pada kitaran ke-limapuluh. Struktur mesoporos ini didapati berupaya mengurangkan kesan perubahan isipadu partikel-partikel tin ketika proses berbalik pengalioian dan nyah-aloi justeru meningkat prestasi cas semula bahan anod ini.

COPYRIGHT

In compliance with the terms of the Copyright Act 1987 and the IP Policy of the university, the copyright of this thesis has been reassigned by the author to the legal entity of the university,

Institute of Technology PETRONAS Sdn Bhd.

Due acknowledgement shall always be made of the use of any material contained in, or derived from, this thesis.

© Siti Munirah Hasanally, 2010
Institute of Technology PETRONAS Sdn Bhd
All rights reserved.

TABLE OF CONTENTS

DECLARATION OF THESIS.....	iv
ACKNOWLEDGEMENTS.....	v
DEDICATION.....	vi
ABSTRACT.....	vii
ABSTRAK.....	ix
COPYRIGHT	xi
TABLE OF CONTENTS.....	xii
LIST OF TABLES.....	xv
LIST OF FIGURES.....	xvi

Chapter

1. INTRODUCTION.....	1
1.1. Age of Electricity.....	1
1.2. Battery.....	2
1.3. Types of Battery.....	3
1.4. Rechargeable Battery.....	3
1.5. The Lithium-Ion Battery.....	4
1.6. Research Motivation.....	6
1.7. Organization of Thesis.....	8
2. LITERATURE REVIEW.....	10
2.1. Historical Development of Lithium-Ion Battery.....	10
2.2. Reaction Mechanism of Rechargeable Lithium-Ion Battery.....	12
2.3. Characteristics of Electrode Materials.....	15
2.4. Anode Material for Lithium-Ion Cells.....	16
2.4.1. Graphite.....	16
2.4.2. Lithium Alloys.....	19
2.4.3. Tin Composite Oxide.....	22
2.4.4. Tin-Based Intermetallics.....	24
2.4.5. Tin Phosphate.....	27
2.5. Potential of Mesoporous Tin Phosphate as Anode Material for Lithium-Ion Battery.....	29

3. METHOD OF INVESTIGATION.....	32
3.1. Overview.....	32
3.2. Materials and Chemicals.....	33
3.3. Synthesis of Mesoporous Tin Phosphate by Sodium Dodecyl Sulfate Templating Method.....	34
3.4. Methods of Characterization.....	36
3.4.1. Thermal Analysis.....	36
3.4.2. Powder X-Ray Diffraction.....	36
3.4.3. Field-Emission Scanning Electron Microscope.....	38
3.4.4. Physisorption Study.....	40
3.4.5. Fourier Transform Infrared Spectroscopy.....	42
3.5. Electrode Fabrication and Cell Assembly.....	43
3.6. Electrochemical Performance Assessment.....	45
3.6.1. Cyclic Voltammetry.....	45
3.6.2. Galvanostatic Charge-Discharge Tests.....	46
4. STRUCTURAL AND MORPHOLOGICAL CHARACTERIZATION OF TIN PHOSPHATE.....	48
4.1. Overview	48
4.2. Synthesis of Mesoporous Tin Phosphate.....	48
4.3. Thermal Analysis on Tin Phosphate.....	50
4.4. X-Ray Powder Diffraction Analysis on Tin Phosphate.....	54
4.5. Physisorption Studies Based on Nitrogen Sorption Isotherm.....	60
4.6. FESEM Analysis on Tin Phosphate.....	68
4.7. Summary.....	72
5. ELECTROCHEMICAL PERFORMANCE OF MESOPOROUS TIN PHOSPHATE AS ANODE MATERIAL.....	73
5.1. Overview.....	73
5.2. Cyclic Voltammetry Analysis on Mesoporous and Non-Mesoporous Tin Phosphate Electrode.....	75
5.3. Voltage Profile on Initial Charge and Discharge Cycle of Mesoporous and Non-Mesoporous Tin Phosphate Anode.....	81
5.4. Ex-Situ Analysis of Mesoporous Tin Phosphate Anode Using Infrared Technique.....	88
5.5. Comparison on Cycling Behavior between Mesoporous and Non-Mesoporous Tin Phosphate Anodes.....	93
5.6. Ex-Situ FESEM Analysis on Cycled Mesoporous and Non-Mesoporous Tin Phosphate Anodes.....	100

5.7.	Effects of Voltage Cutoff on Charge-Discharge Performance of Mesoporous Tin Phosphate Anode.....	103
5.8.	Cycling Profile of Mesoporous Tin Phosphate Anode.....	110
5.9.	Summary.....	112
6.	STRUCTURAL INFLUENCE OF MESOPOROUS TIN PHOSPHATE ON ITS ELECTROCHEMICAL PROPERTIES.....	113
6.1.	Overview.....	113
6.2.	Crystallographic Features and the Electrochemical Properties of Tin Phosphate.....	114
6.3.	Mesoporous Morphology and the Electrochemical Properties of Tin Phosphate.....	116
6.4.	Summary.....	120
7.	CONCLUSION.....	121
7.1.	Review of Study.....	121
7.2.	Suggestions for Future Studies.....	124
	REFERENCES.....	125

LIST OF TABLES

Table 2.1:	Theoretical capacities for selected lithium alloy and graphite.....	20
Table 3.1:	Materials and chemicals used.....	33
Table 4.1:	BET surface areas of synthesized SnP_2O_7 powders.....	64
Table 4.2:	Structural properties of SDS synthesized SnP_2O_7 calcined at different temperature.....	59
Table 5.1:	Initial charge discharge capacity of SnP_2O_7 anodes cycled between 0.0-2.0 V.....	81
Table 5.2:	Discharge and charge capacities for MP200, MP300, MP400, MP4004 anodes.....	94
Table 5.3:	Discharge and charge capacities for MP500, TP500 and graphite anodes.....	95

LIST OF FIGURES

Figure 1.1:	Energy storage performance of different battery chemistries.....	5
Figure 2.1:	Schematic representation of a lithium-ion cell in charging mode.....	14
Figure 2.2:	Schematic representation of a lithium-ion cell in discharging mode....	14
Figure 2.3:	Structure of graphite.....	16
Figure 2.4:	The in-plane structure of LiC_6	17
Figure 3.1:	Flowchart on research phase and experimental techniques applied....	32
Figure 3.2:	Flowchart on the synthesis of mesoporous SnP_2O_7 by surfactant templating method.....	35
Figure 3.3:	Schematic representation of Bragg's law.....	37
Figure 3.4:	Schematic diagram of a three-electrode configuration electrochemical test cell.....	41
Figure 3.5:	Schematic diagram of a two-electrode configuration electrochemical test cell.....	41
Figure 3.6:	(a) WonATech WBCS Battery Cycler equipment (b) Two-electrode electrochemical cell being connected to the battery cycler equipment	47
Figure 4.1:	TG-DTA curves for tin phosphate.....	51
Figure 4.2:	TG-DTA curves for surfactant synthesized tin phosphate.....	52
Figure 4.3:	XRD pattern for tin phosphate synthesized without SDS surfactant (a) $2\theta = 1-10^\circ$ and (b) $2\theta = 10-80^\circ$	55
Figure 4.4:	XRD pattern of tin phosphate synthesized with SDS surfactant (a) $2\theta = 1-10^\circ$ and (b) $2\theta = 10-80^\circ$	57
Figure 4.5:	XRD pattern of mesostructured tin phosphate calcined at 400°C for 2h and 4h.....	59
Figure 4.6:	Nitrogen adsorption/desorption isotherms for SDS synthesized SnP_2O_7 calcined for 2hr at (a) 200°C ; (b) 300°C ; (c) 400°C (d) 400°C for 4h and (e) 500°C	61
Figure 4.7:	Nitrogen adsorption/desorption isotherms for non-SDSsynthesized SnP_2O_7 calcined at (a) 200°C ; (b) 300°C ; (c) 400°C and (d) 500°C ...	63

Figure 4.8:	Pore size distribution of mesoporous SnP_2O_7 calcined for 2h at 200, 300 and 400°C and for 4 h at 400°C.....	66
Figure 4.9:	FESEM images of SDS synthesized SnP_2O_7 calcined at (a) 200°C for 2 hr, (b) 300°C for 2 hr, (c) 400°C for 2 hr and (d) 400°C for 4 hr and (e) 500°C for 2 hr.....	69
Figure 4.10:	FESEM images of non-SDS synthesized SnP_2O_7 calcined at (a) 200°C for 2 hr, (b) 300°C for 2 hr, (c) 400°C for 2 hr and (d) 500°C for 2 hr.....	71
Figure 5.1:	Cyclic voltammograms of mesoporous SnP_2O_7 calcined at; (a) 200°C for 2 hr (MP200), (b) 300°C for 2 hr (MP300), (c) 400°C for 2 hr (MP400) and (d) 400°C for 4 hr (MP4004).....	77
Figure 5.2:	Cyclic voltammograms of (a) SDS synthesized SnP_2O_7 calcined at 500°C for 2 hr (MP500) and (b) non-SDS synthesized SnP_2O_7 calcined at 500°C (TP500).....	80
Figure 5.3:	First cycle data on charge discharge curve and differential capacity plot for mesoporous SnP_2O_7 anodes, MP200, MP300, MP400 and MP4004.....	83
Figure 5.4:	First cycle data on charge discharge curve and differential capacity plot for non-mesoporous SnP_2O_7 anodes, MP500 and TP500.....	85
Figure 5.5:	FTIR spectra of (a) pristine MP400 anode, (b) MP400 discharged to 1.1 V, (c) MP400 discharge to 0 V and (d) MP400 charged to 2.0 V.....	90
Figure 5.6:	Discharge capacity of mesoporous SnP_2O_7 anodes (MP200, MP300, MP400 and MP4004), non-mesoporous SnP_2O_7 anodes (MP500 and TP500) and graphite anode.....	93
Figure 5.7:	FESEM images of MP400 anode (a) before cycling, (b) after 1 cycle and (c) after 10 cycles.....	101
Figure 5.8:	FESEM images of TP500 anode (a) before cycling, (b) after 1 cycle and (c) after 10 cycles.....	101
Figure 5.9:	Voltage profile for MP400 cycled between (a) 0-1.2 V, (b) 0-1.6 V and (c) 0-2.0 V.....	105
Figure 5.10:	Discharge capacity vs. cycle number of MP400 anode cycled between 0-1.2 V, 0-1.6 V and 0-2.0 V. $R_{10/2}$ denotes the capacity retention index.....	106

Figure 5.11: Differential capacity plots of MP400 cycled within specified voltage range; (a) 2 nd cycle (0-1.2V), (a') 10 th cycle (0-1.2V), (b) 2 nd cycle (0-1.6V), (b') 10 th cycle (0-1.6V) and (c) 2 nd cycle (0-2.0V) and (c') 10 th cycle (0-2.0V).....	108
Figure 5.12: Charge-discharge capacity and Coulombic efficiency versus cycle number for MP400 cycled within 0-1.2 V.....	105

CHAPTER 1

INTRODUCTION

1.1 Age of Electricity

Energy is a key component of human society. The search for energy sources to provide comfort and smooth life style has taken place since the beginning of civilization. Global environmental concern over the reliance of fossil fuel has aroused a worldwide search for more efficient, pollution-free, economically viable and sustainable sources of energy. Electricity is a popular source of energy as it is clean, safe and convenient to use. The present age is often called the Age of Electricity because humanity has become dependent on electricity, a product that made technological advancements possible. The need for mobility has resulted in the advent of mobile technology in electric powered consumer devices such as mobile phones, laptops, camcorders etc. Since portable consumer electronic devices have been introduced into the market, they have continued to grow more important and indispensable from everyday human lives as we step into the new and modern age. Mobile electronic devices from mobile phones and laptops to wearable or implanted medical devices have already become or will soon become a necessity in people's lives. The increasing interest and dependency of the modern society on mobile electronic devices has generated the need for portable energy storage. Portable electrochemical energy storage systems include batteries, fuel cells and electrochemical capacitors. Battery is a popular choice of portable energy storage system to supply power to the components in the mobile device to operate. Almost all portable electronic gadgets today contain a battery.

1.2 Battery

When a chemical reaction is caused by an external voltage or if a voltage is caused by a chemical reaction, it is called an electrochemical reaction. A battery is defined as a self-supporting energy storage medium that store chemical energy contained in its active materials (positive and negative electrodes) and on demand, converts it directly into electrical energy to power an intended device [1]. A battery is composed of one or several electrochemical cells that are connected in series and/or in parallel to provide the required voltage and capacity, respectively [2].

The electrochemical cell is the working chemical unit inside a battery. Each cell consists of a positive electrode and a negative electrode, separated by an electrolyte solution containing dissociated salts which enable ion transfer between the two electrodes [2]. The battery functions by providing separate pathways for electrons and ions to move between the site of oxidation and the site of reduction. The electrons pass through the external circuit where they can provide work such as powering a portable device. The ions, on the other hand, pass through the ionically conducting and electronically insulating electrolyte that lies between the two electrodes inside the battery. The ionic current is separated from the electronic current. When a battery is in use or discharged, an electrochemical oxidation reaction takes place at the negative electrode (anode) where ions and electrons are generated. Electrons travel through the external circuit while ions flow through the electrolyte to the positive electrode (cathode). A simultaneous electrochemical reduction reaction proceeds at the cathode where electrons are accepted from the external circuit, thereby completing the electrical circuit. The amount of ionic charge carried through the electrolyte is the same as the electronic charge carried through the external circuit.

1.3 Types of Battery

Batteries can be classified into three general classes: primary, secondary and specialty batteries. Primary battery generates electrical energy from chemical reaction until exhausted. It is designed to be used once and discarded. Primary batteries are often called disposable batteries. Discharge is the process of a battery during operation and primary batteries are assembled in the charged state [1]. Common types of primary batteries include zinc-carbon batteries and alkaline batteries. Secondary battery, also known as rechargeable battery is discharged during operation and could be restored to its original condition by applying an electric current which reverses the chemical reactions that occur during discharge [1]. Devices to supply the appropriate current are called chargers or rechargers. Secondary batteries are usually assembled in the discharged state; they have to be charged first before they can undergo discharge in a secondary process [1]. Examples of rechargeable batteries are lead acid batteries, nickel cadmium batteries, nickel-metal hydrides batteries and lithium-ion batteries. Specialty battery is a primary battery that is designed to fulfil a specific purpose. These batteries are mainly for military and medical applications that have limited and specified market production [1].

1.4 Rechargeable Battery

Every year billions of batteries are produced and sold worldwide. Many are alkaline batteries which are discarded after single use. Ongoing research and advances in battery technology have steadily replaced single use alkaline batteries with higher capacity and environmentally friendly rechargeable batteries that last far longer and can be used hundreds of times. The rapid outbreak of technology in consumer electronics has been paralleled by achievements in energy storage devices. The increasing demand for portable devices such as laptops, mobile phones, audio digital players (e.g. MP3, iPods) and cordless power tools has boosted the sales of rechargeable batteries in recent years.

The concept of rechargeable battery has been around since 1859 when French physicist Gaston Plante invented the lead acid cell which was the world's first rechargeable battery [3]. The same chemistry is still used in today's car battery. Different types of rechargeable batteries utilise different chemistry systems to store electricity. The nickel cadmium (Ni-Cd) battery uses nickel oxide hydroxide and metallic cadmium as electrodes [3]. This battery was banned for most uses by European Union in 2004 as cadmium is a toxic element. These batteries have been almost completely superseded by nickel-metal hydride (Ni-MH) batteries. The Ni-MH battery uses hydrogen-absorbing alloy and nickel oxide hydroxide as electrodes and has two to three times the capacity of an equivalent size nickel cadmium battery [3]. The lithium-ion (Li-ion) battery uses graphite and a layered oxide material such as lithium cobalt oxide as electrodes. The energy is stored in these batteries through the movement of lithium ions [3].

1.5 The Lithium-Ion Battery

When Li-ion batteries were introduced into the market in 1991 by Sony Corporation, it represented a revolution in the power source industry. Sony developed a carbon anode that is capable of reversibly intercalating and de-intercalating lithium ions and paired it with a high voltage positive electrode material using lithiated cobalt oxide. A comparison on energy density characteristics showed that Li-ion batteries outperform other competing rechargeable battery systems, as observed in Figure 1 [4]. Lithium polymer batteries are technologically improved version of the Li-ion battery where the lithium salt electrolyte is being held by a polymer membrane instead of an organic solvent. Lithium polymer battery is more flexible and robust to physical damage. *Energy density* is a characteristic parameter of a battery indicating the amount of electrical energy stored per unit weight or volume [4]. Weight based energy density is often called *specific energy* or *gravimetric energy density* [1]. Volume based energy density is often called *energy density* or *volumetric energy density* [1]. The energy density is typically expressed as watt-hour/kilogram (W h kg^{-1}) or watt-hour/liter (W h l^{-1}).

The Li-ion battery has several advantages over the Ni-Cd and Ni-MH batteries. A Li-ion battery can store more than twice the energy compared with other conventional rechargeable batteries of the same size and weight. The Li-ion battery provides a higher average potential of 3.6 V which is almost three times than that of NiCd and NiMH batteries and delivers twice higher capacity compared to that of Ni-Cd and Ni-Mh batteries. The Li-ion batteries have no memory effect which means that they do not have to completely be discharged before recharging as with other rechargeable batteries. Self-discharge refers to the loss of charge when a battery is not in use. A lithium-ion battery have a low self-discharge rate of approximately 5% per month compared to a 20% per month and 30% per month in NiCd batteries and NiMH batteries, respectively [3].

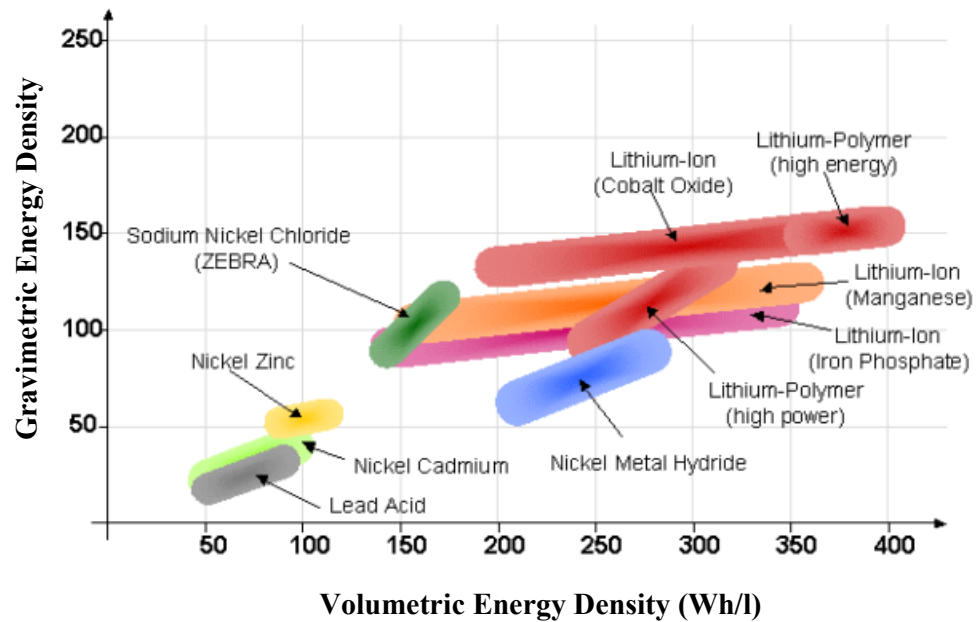


Figure 1.1: Energy storage performance of different battery chemistries (adapted from [4]).

A market research carried out by SBI Reports reported that rechargeable batteries are a continuing strong market, with worldwide sales of USD \$36 billion in 2008 [5]. The rechargeable battery market will rise to USD \$51 billion by 2013. Whether it is a

battery for the latest laptop, energy storage for a hybrid electric vehicle, or backup power for a remote telecommunications site, everyone wants a battery that has the highest energy density, best safety factor, and longest life in term of discharge cycles and ease of maintenance while still being environmentally friendly. These are the drivers behind rechargeable battery research around the world today. Lithium-ion is the battery chemistry of choice for future generations of portable electronics and hybrid and plug-in hybrid electric vehicles. In 2008, lithium-ion battery research had more funding than all other battery technologies combined [5]. Nanotechnology and chemistry advances in electrode design are the key research topics that companies are using to push lithium-ion to be the dominant energy storage technology in the future. The portable rechargeable battery market, of which lithium-ion has a 75% share, is the fastest growing segment of the rechargeable battery market, showing world market growth of 20% in 2008 [5]. Nickel-cadmium (Ni-Cd) batteries are still important for power tools and back-up systems but will decline rapidly in market share by 2013 due to stricter environmental controls on cadmium [5].

1.6 Research Motivation

Despite the huge success in mass production of millions of Li-ion battery, this battery technology still has a long way to go. As improvements continue to progress in the communication and consumer electronics sector together with the emerging hybrid vehicle technology, Li-ion batteries are expected to evolve in order to meet the ongoing market innovations. Many on-going research activities are focussed on the development of electrode materials that could enhance the performance of Li-ion batteries.

The specific capacity (quoted in mAh/g) of cathode material is often lower than anode material. Batteries of increased capacity can be designed by using the high capacity anode material to accommodate more of the low capacity cathode material. The graphite anodes that are currently employed in the commercial Li-ion batteries will soon be unable to meet the ever-increasing capacity requirements of innovative

portable electronic devices due to its restricted theoretical capacity of 372 mAh/g. New host materials with even higher lithium ion storage capacity than graphite need to be developed. One possible candidate as anode material is the tin-based materials with a high theoretical capacity of 993 mAh/g and low potential of lithium insertion of less than 1 V [6]. Unfortunately, efforts to commercialize them have been hindered by severe volume change in lithium ion insertion and extraction reactions that occur during charging and discharging. The mechanical stress induced by the volume change causes the disintegration of the anode material and loss of material cyclability [6]. Several approaches have been developed by researchers to resolve the effects of volume changes of tin based materials during cycling such as by reducing the particle size of the active tin particles as well as using intermetallic multiphase alloys and mixed-conductor composite materials [6].

This research work employs a mesoporous, active-inactive tin based material concept to compensate the detrimental effect of volume changes experienced by the active tin material during repeated charge-discharge cycles. A mesoporous tin phosphate was synthesized and its electrochemical reaction with lithium was studied in this work. Tin phosphate has been reported to be able to reversibly insert and extract lithium ions within its structure [7]. Phosphate serves as an inactive matrix that supports and holds the lithium-tin regions together with minimal volume change [7]. Mesoporous materials have been widely investigated for their potential application as catalysts, electrical insulators and optics. Their application as electrode materials in Li-ion battery is not widely studied. It is postulated that a mesoporous anode may further reduce the extent of electrode disintegration by alleviating the volume expansion caused during cycling. Hence, mesoporous tin phosphate anode may offer benefits of a more stable cycling performance. The objective of this work is to assess the electrochemical behaviour of mesoporous tin phosphate upon reaction with lithium and deliberate on its potential application as anode material for lithium-ion batteries.

1.7 Organisation of Thesis

This thesis presents findings based on experimental work carried out on the laboratorial synthesized mesoporous tin phosphate. This thesis has been sectioned into several chapters, starting with Introduction and coherently followed by chapters detailing on the research methodology and results obtained. Brief descriptions on the subsequent chapters are as follows;

Chapter Two contains a brief background on rechargeable lithium ion battery science, comprehensive literature review based on researches carried out on alternative anode materials from tin based materials to provide new insights to investigate the potential of mesoporous tin phosphate as the next generation of anode material for Li-ion battery.

Chapter Three provides explanation on the experimental methodology used in this work. Synthesis of mesoporous tin phosphate was carried out using an anionic surfactant, sodium dodecyl sulphate whereas the non-mesoporous tin phosphate was synthesized without the presence of the surfactant. Characterization tools that were used to analyze the physical and electrochemical properties of the synthesized tin phosphate are elaborated here.

In Chapter Four, the physical and morphological characterization results of the synthesized tin phosphate are discussed extensively. The mesostructured characteristics of the tin phosphate synthesized in the presence of the surfactant was indicated by means of powder X-Ray Diffraction (XRD) and physisorption technique. The particle surface morphologies of the mesoporous and non-mesoporous tin phosphate was examined using Field Emission Scanning Electron Microscope (FESEM).

In Chapter Five, the electrochemical performance of the mesoporous and non-mesoporous tin phosphate was analyzed by means of cyclic voltammetry and charge-discharge measurements. The electrochemical mechanism entailing the irreversible and reversible reaction was further discussed using various analysis perspective based

on the electrochemical performance data. Ex-situ analysis using infrared spectroscopic and microscopic techniques were carried out on cycled anode to determine the after effects of the electrochemical redox reaction with lithium.

Chapter Six summarizes and concludes the findings of this research together with some suggestions for future work in this research subject.

CHAPTER 2

REVIEW OF LITERATURE

2.1 Historical Development of Lithium-Ion Battery

The first concept of rechargeable Lithium battery, developed based on the insertion compound chemistry was proposed by Whittingham in 1970s where an insertion material (titanium sulphide) was used as the lithium-ion accepting cathode material, metallic lithium metal as the negative material and lithium perchlorate in dioxolane as the electrolyte [8]. The electrode materials could host lithium ions inside its structure and at the same time reduce transitional metals from their higher oxidation state. This electrochemical reaction would occur reversibly without major phase changes. However, this system was undermined by safety issues associated with dendritic lithium formation during charging and discharging cycles which can cause short circuits and explosion hazards. Two research approaches were taken to overcome the safety concerns in handling lithium metal in rechargeable lithium batteries. The first is to replace the lithium metal negative electrode with an electrode made of lithium insertion compound. A second approach was to use conducting polymers instead of organic liquids as electrolytes. Conducting polymers do not react with metallic lithium as organic liquid so the safety issues could be eliminated.

In 1976, Besenhard and Fritz studied the reversible electrochemical intercalation of lithium into graphite and established that graphite can intercalate one lithium atom for every six carbon atoms [9]. In 1980, Lazzari and Scrosati proposed the *rocking chair* concept which describes the use of two insertion compounds based on lithium tungsten oxide and lithium titanium sulphide [10]. The lithium insertion compounds are capable of acting as host solid for reversible insertion of lithium guest ions. The rocking chair battery functioned on the principle of simultaneous lithium-

ion insertion and extraction in both electrodes. During discharge, lithium ions are removed from the host anode insertion compound and are inserted into the host cathode insertion compound. Upon reversing the current flow where the charging process occurs, the reverse reaction takes place. The charge-discharge process involves the cyclic transfer of lithium ions (similar to rocking) from the anode to the cathode and vice-versa. This system was much safer as lithium is utilised in its ionic state rather than in metallic state. However, this cell was only working at an average voltage of 1.8 V. In 1983, Basu investigated the performance of lithium intercalated graphite (LiC_6) anode in an electrolyte containing lithium hexafluoroarsenate (LiAsF_6) dissolved in dioxolane [10]. The graphite was pre-lithiated before cell assembly and the cathode material, niobium selenide (NbSe_3) did not contain lithium ions at the initial state.

Goodenough *et al.* discovered lithium ions could be reversibly inserted and extracted from a layered lithium cobalt oxide (LiCoO_2) in 1980 [6] at a higher working potential of 4.2 V versus metallic lithium. Capitalizing on earlier findings on the reversible lithium ion intercalation and de-intercalation process in carbonaceous material and on reversible lithiation and de-lithiation of lithium cobalt oxide, Tazawa and Nagaura published their work describing the creation of the C/ LiCoO_2 rocking chair cell, its construction and performance which was shortly followed by commercialization of the first Li-ion battery by Sony Corporation in June 1991 [12].

Researches on electrolyte have led to the concept of solid polymer electrolyte which involves the use of a polymer matrix swollen with liquid solvent and lithium based salt [13], [14]. Combining the technology of liquid Li-ion batteries and the manufacturing advantages presented by the polymer technology, Bellcore researchers introduced polymeric electrolytes in a liquid Li-ion battery system [15], which is known as polymer Li-ion battery. This technology involves the usage of a copolymer of vinylidene difluoride with hexafluoropropylene (PVdF-HFP) binder bonded to the electrodes. These types of batteries which has been commercialize in 1999, offer

shape versatility, flexibility, lightness and present many advantages in the electronic miniaturization technology trend.

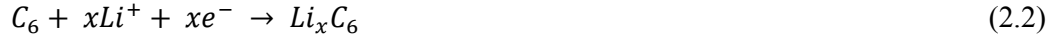
2.2 Reaction Mechanism of Rechargeable Lithium-Ion Battery

The working principle of rechargeable lithium ion (Li-ion) batteries is based on an electrochemical reaction referred to as electro-insertion reaction. This electro-insertion reaction is basically a host/guest solid state redox reaction involving electrochemical charge transfer coupled with insertion of mobile guest ions into the host material without major structural changes. A common convention in the literature of Li-ion battery is that *intercalation* is regarded as a special case of insertion. The term *intercalation* implies the restricting condition that a layered host takes up guests within its interlayer gaps which may result in a volume change perpendicular to the layers, but which causes no other structural changes [6]. Any other lithium storage process in materials without significant layered structure is considered as insertion process.

A basic Li-ion cell consists of a positive electrode (cathode) composed of a lithium ion source material, lithium cobalt oxide (LiCoO_2) and a negative electrode (anode) from graphite. The two electrodes are separated by a porous film soaked in lithium hexafluorophosphate (LiPF_6) dissolved in dimethyl carbonate (DMC) and ethylene carbonate (EC). The guest ions are lithium ions (Li^+) and the host solid is graphite (usually denoted as C_6). As illustrated in Figure 2.1, during charging under applied voltage, Li^+ are extracted from LiCoO_2 cathode into the electrolyte and simultaneously an equivalent amount of Li^+ from the electrolyte are intercalated between the carbon layers in the graphite anode. Electrons are driven out through the external circuit to the anode. The cathode compensates the removal of lithium by the oxidation of the transition metal present in the lattice ($\text{Co}^{+3} \rightarrow \text{Co}^{+4}$). The chemical reaction at this electrode is given below:



The intercalated Li^+ will recombine with the electrons resulting in reduction of the graphite, which is represented by the chemical equation below;



Upon discharging as shown in Figure 2.2, the reverse process takes place where Li^+ are moved out of the graphite, through the electrolyte and back to the cathode where cobalt is subsequently reduced and LiCoO_2 is reformed, while electrons flow from anode to cathode powering the external circuit. The Li^+ are transferred back and forth between anode and cathode through the electrolyte during the charging (reduction) and discharging (oxidation) processes. One electrode intercalates Li^+ while the other de-intercalates Li^+ at the same time. Accordingly, the cells have been termed as rocking-chair batteries.

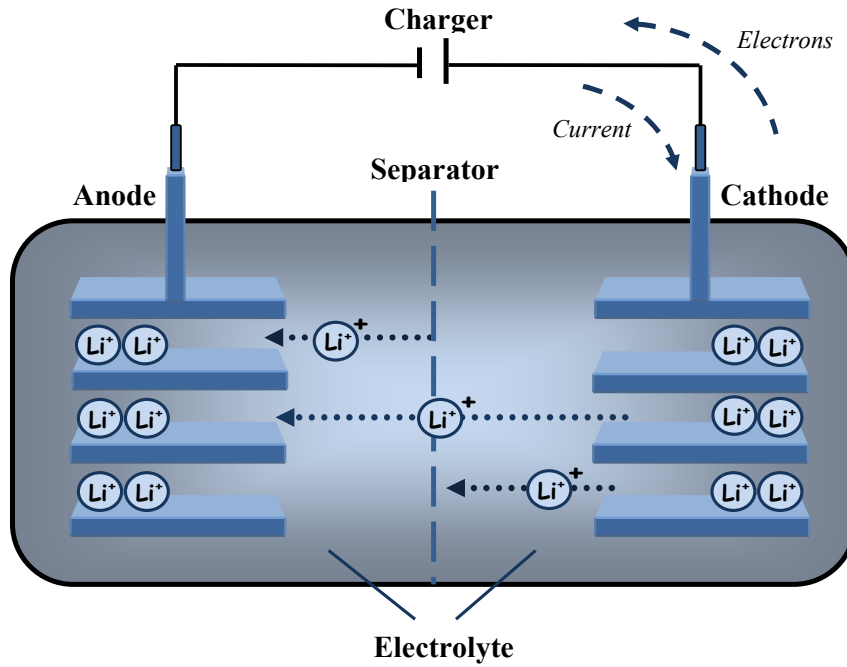


Figure 2.1: Schematic representation of a lithium-ion cell in charging mode.

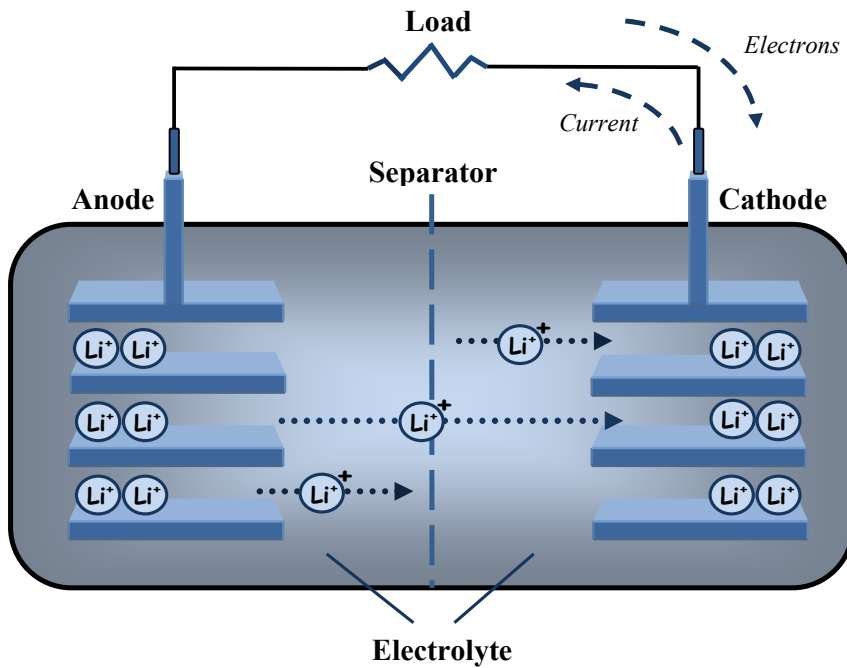


Figure 2.2: Schematic representation of a lithium-ion cell in discharging mode.

2.3 Characteristics of Electrode Materials

The strategy of using lithium insertion compounds as electrode materials in Li-ion battery should satisfy several important criteria in order for them to deliver high performance. A lithium insertion compound should be able to allow a large amount of lithium ion insertion/extraction to take place in order to maximise the cell capacity, have good electronic and ionic conductivity, and stable chemical and structural stabilities [6]. Good electronic and ionic conductivity properties could minimize polarization losses during the charging and discharging process and thereby support a high current and power density. The reversible Li^+ insertion and extraction reaction should have no or minimal changes to the host structure in order to provide a longer cycle life for the cell. From a commercial point of view, the insertion compounds should be inexpensive, environmentally safe and lightweight.

The main difference between the anode and cathode insertion hosts is that the anode should have a low lithium chemical potential in order to maximise the cell voltage. Careful selection of cathode and anode pairs is required to maintain an acceptable cell voltage of at least 3 V [6]. The anode and cathode insertion hosts should have the lowest and highest voltages versus metallic lithium, respectively in order to maximise the cell voltage. Lithium insertion compound such as lithium cobalt oxide (LiCoO_2), lithium manganese oxide (LiMn_2O_4) and lithium nickel oxide (LiNiO_2) make attractive cathode materials as they have high electrode potential of 4 V [6]. Lightweight carbonaceous materials such as graphite and coke have lower electrode potential of less than 1 V versus lithium which made them attractive anode material [6].

2.4 Anode Materials for Lithium Ion Cells

2.4.1 Graphite

Lithium can be intercalated into carbonaceous materials. Graphite with a high degree of crystallinity appears to be the most desirable candidate due to the high host capacity (LiC_6), low and flat electrode potential profile similar to that of lithium metal (0.01-0.02 V) [6]. Graphitic carbons basically comprise of sp^2 -hybridized carbon atoms which are arranged in a hexagonal network known as the graphene layer. Van der Waals forces provide a weak bonding between the graphene layers leading to the layered graphite structure [6]. Graphite has its graphene layers stacked in an ABAB order. The B layer is shifted by $1/3$ of a unit cell along the 110 crystal direction with respect to the A layer (Figure 4) [16].

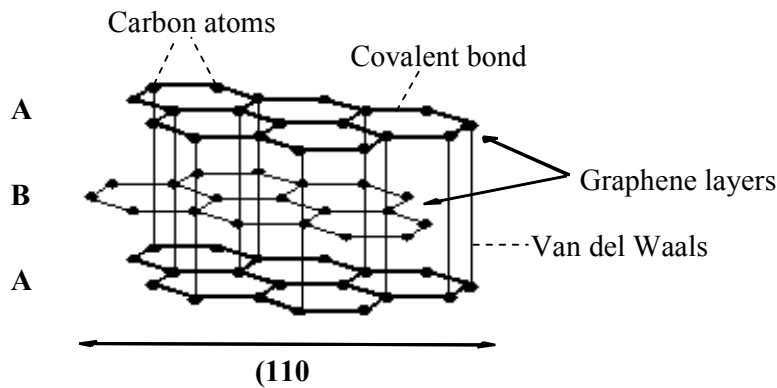


Figure 2.3: Structure of graphite (adapted from [16]).

Upon lithium intercalation into the graphite host, the graphene layers shift from ABAB to AAAA stacking arrangement. Under ambient condition, perfectly ordered graphite intercalates one lithium ion into every three carbon hexagons, resulting in LiC_6 . The in-plane structure of LiC_6 is shown in Figure 2.4 [16].

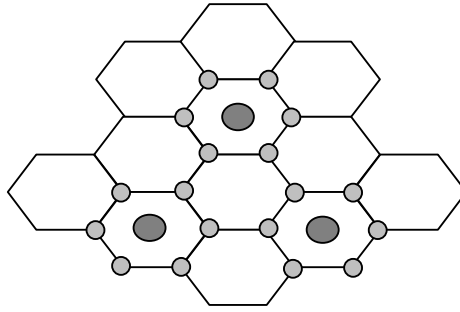


Figure 2.4: The in-plane structure of LiC_6 (adapted from [16]).

The capacity of a cell is expressed as the total quantity of electricity involved in the electrochemical reaction and is defined in terms of Coulombs or *ampere-hours*. The *ampere-hour capacity* of a battery is directly associated with the quantity of electricity obtained from active materials. The quantity of electricity can be expressed as the number of moles of electrons passing through a cell. Faraday's first law of electrolysis states that the mass of a substance deposited, evolved or dissolved at an electrode is proportional to the quantity of electrical charge passed during electrolysis. The amount of electricity passing through the circuit in a given time is the number of moles of electrons passing through the circuit in that time and the charge, Q is related to the current by,

$$Q = It \quad (2.3)$$

One Coulomb corresponds to a current of 1 Ampere during one second. One mole of electrons has a charge of 96,487 Coulombs of electricity that produces one gram equivalent of a substance by electrolysis. In transferring one mole of electrons in an hour basis, the current required is,

$$96487 \text{ Coulomb} = I(3600 \text{ seconds})$$

$$I = 26.8 \text{ Ampere hour}$$

Theoretical specific capacity of an electrode material expressed in mAh/g is given by,

$$\text{specific capacity} = \frac{26.8}{nm} \times 1000 \quad (2.4)$$

Where n is the number of moles of the anode material required to transfer 1 mole of charge and m is the molar mass (g/mol) of the anode material. During the charging process, the electrochemical reaction at graphite is expressed as follows:



The above reaction showed that transferring one mole of Li^+ from cathode to anode results in the simultaneous transfer of one mole of charge through the external circuit. Graphite can intercalate one lithium atom for every six carbon atoms. Therefore, the theoretical specific capacity of graphite can be calculated based on Equation (2.4) as follows:

$$\begin{aligned} \text{specific capacity of graphite} &= \frac{26.8 \text{ Ah}}{6(\text{mol}) \times 12.011 \left(\frac{\text{g}}{\text{mol}}\right)} \times 1000 \\ &= 372 \text{ mAh/g} \end{aligned}$$

Theoretically, the intercalation of Li^+ into graphite is fully reversible with a specific capacity of 372 mAh/g. This, however only applies to the case of a perfect crystal. In practical cases, graphite produced industrially does not have a perfect crystal structure. The capacity is also affected by irreversible reactions experienced by graphite during the cell's charging and discharging process, which leads to some losses in capacity. The initial interaction between graphite and electrolyte during the first charging process causes the electrolyte to be reduced by forming a passivating film on the surface of the carbon particles. This film, known as the solid electrolyte interface (SEI) is composed of mainly lithium carbonate and lithium alkyl carbonate as the electrolyte solvents generally contains alkyl carbonates and highly soluble lithium salts [17]. The SEI film is electronically insulating and permeable to Li^+ [17]. The formation of this film consumes lithium which is provided from the cathode and

electrolyte during the charging process. This reaction is irreversible and results in some charge loss, which is referred to as *irreversible capacity* [18]. Since the cathode is the only lithium source in the Li-ion cell, these losses are detrimental to the capacity of the whole cell. Another major problem of graphite anodes is that the intercalation of Li^+ from organic solvent electrolytes proceeds together with the organic solvent and yields large interlayer expansion and the subsequent degradation of graphite structure and additional irreversible capacity [18].

2.4.2 Lithium Alloys

Other possible alternative anode material that has been considered to replace the lithium metal in rechargeable lithium cells are lithium alloys as they are expected to be safer. Lithium (Li) is able to form intermetallic phases with some elements from the Group III, Group IV and Group V of the periodic table such as aluminium (Al), silicon (Si), germanium (Ge), tin (Sn), Plumbum (Pb), antimony (Sb) and bismuth (Bi), at room temperature if the metal is polarized to a negative potential in a Li^+ containing liquid organic electrolyte [6][19]. These elements show different reaction with Li ranging from 1.0 to 0.1 V [6]. Early work on lithium alloys were connected with their use in high temperature cells ($\sim 400^\circ\text{C}$), which operate in molten salt electrolytes. Lithium alloys were used because metallic lithium (Li) melts around 180°C [19]. Lithium alloys were used as negative electrode in thermal battery under high temperature condition. Matsushita commercialised the first cell using lithium alloy operating at ambient temperature based on Wood's metal (an alloy of Bi, Pb, Cd, Sn) in 1980s, however, the commercial success was short lived as this cell was found to deteriorate with increased depth of discharge [2]. The reversible reaction of Li with storage metal M (M= Al, Sn, Si, Pb, Sb, etc) to form lithium alloy (Li_xM) follows according to [19],



Table 2.1 shows the theoretical specific capacity for selected lithium storage metals and graphite, calculated using Equation (2.4). The theoretical specific capacities of lithium alloys are higher than that of lithiated graphite as these metals can store and release large amount of lithium. Lithium alloys also assure high voltages when combined with metal oxide cathodes and do not suffer from solvent co-intercalation issues [19].

Despite these advantages, lithium alloys are still not utilized in commercial Li-ion cells because they suffer from cyclability issues. The storage metals undergo major changes in structure and in volume while alloying with lithium. These alloys are not intercalation compounds. The lithium stored in the metal host is in the ionic form and not in atomic form. During the charging and discharging process, the insertion and removal of Li^+ is accompanied by large volume changes in the host material. The lithium alloys, Li_xM are of highly ionic character and therefore they are usually brittle [19], [20]. Mechanical stresses induced from the volume changes, lead to the deterioration in mechanical stability of the anode [19], [20]. This will then cause the anode to crack and pulverize thus reducing the anode lifetime [19], [20].

Table 2.1: Theoretical capacities for selected lithium alloy and graphite

Unlithiated metal	Fully lithiated metal	Capacity (mAh/g)
Al	LiAl	994
Pb	$\text{Li}_{4.4}\text{Pb}$	569
Sb	Li_3Sb	660
Si	$\text{Li}_{4.4}\text{Si}$	4199
Sn	$\text{Li}_{4.4}\text{Sn}$	993
C, graphite	LiC_6	372

Host metal properties such as particle size, shape, texture and porosity strongly affect the macroscopic dimensional stability during lithium alloying and de-alloying process [19]. Although volume changes of metal hosts upon alloying with lithium are in the order of several 100%, large absolute volume changes can be avoided when the

size of metallic host particles is kept small [19]. The practicality of this concept was checked by Besenhard, Yang and Winter by employing tin anodes of different particle sizes which have been prepared by electroplating on copper substrates from aqueous solutions containing tin cations (Sn^{2+}) [20], [21]. In the case of coarse tin particles, the formation of large cracks and the delamination of active material from substrate are much stronger and appear earlier during cycling than in the case of finer tin particles. The cracks allow the electrolyte to penetrate into fissures between copper current collector and tin deposit, where it is decomposed to electronically insulating products [20], [21]. Due to loss of electronic contact between particles as well as between particles and the current collector, lithium cannot be extracted effectively [21]. Consequently, the amount of active material which is accessible for lithium storage decreases which leads to the eventual failure of the anode material. The magnitude of cracks and pulverization is lesser in finer tin particle size. Although the smaller particle size tin outperforms the coarse one, the cycling stability is still not sufficient [20], [21].

Another approach to lessen the effects of pulverization resulting from large volume changes of lithium alloys during cycling was proposed by Huggins *et al.* [22]. They proposed the ‘mixed-conductor matrix’ concept where particles of the electrochemically active storage metal (reactant) are finely dispersed within a solid, electronically conducting metallic matrix. The matrix should allow rapid transport of electroactive species (Li^+), act as a current collector and maintain the morphology microstructure of the dispersed reactants. The application of tin based composite oxide as anode material was based on this concept where the active tin is dispersed in the formed oxide phases which act as the inactive matrix component [23]-[26]. This concept was also exploited extensively on the study of tin based intermetallics anode material by Dahn *et al.* [28], [29], Tackeray *et al.* [30], [31], and Besenhard *et al.* [21], [32], [33].

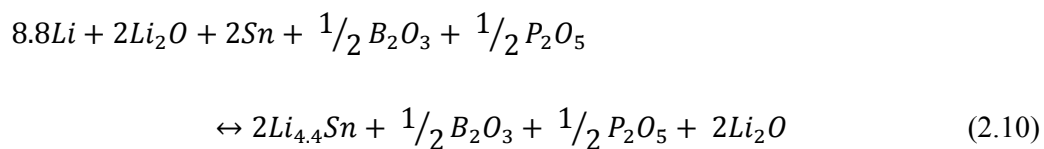
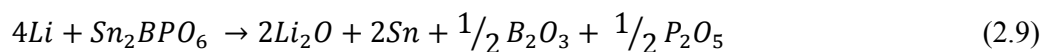
2.4.3 Tin Composite Oxide

When Sony Corporation introduced its carbon based anode in its commercial Li-ion batteries in 1991, research on lithium alloys was dampened. Most researchers concentrate their efforts into development various carbonaceous materials as anode material. Limitations in gravimetric and volumetric capacity of graphite based anode however, have resulted in search for new materials that could supplant it in the next generation of mobile devices that requires higher energy density. In 1997, Fuji Photo Film Celltec Co. announced its new patent on Li-ion technology known as the Stalion[®] Li-ion battery, which claimed to have higher energy density than conventional carbon anode based Li-ion battery [23]. This Stalion[®] Li-ion battery uses an amorphous tin-based composite oxide as its anode material instead of carbon. The tin based composite oxide active material has a basic formula represented by SnM_xO_y , where M is a group of glass-forming metallic elements whose stoichiometric number is equal to or more than that of tin ($x \geq 1$) and is typically comprised of a mixture of Boron (B), Phosphorus (P) and Aluminium (Al) [24]. One typical composition is $\text{Sn}_{1.0}\text{B}_{0.56}\text{P}_{0.40}\text{Al}_{0.42}\text{O}_{3.6}$, was prepared by mixing SnO , B_2O_3 , SnP_2O_7 and Al_2O_3 and heated at 1100°C , followed by quenching to yield a yellowish transparent glass [23]. Following the release of the patent, Y. Idota *et al.* reported the electrochemical behaviour of this composite by assuming Sn (II) behaves as the electrochemically active element for Li insertion whereas the other elements provide an electrochemically inactive network of $-(\text{M}-\text{O})-$ that expands anisotropically, allowing the dispersion of the Sn particles as well as Li^+ diffusion [24]. This anode was reported to be able to deliver a reversible capacity of more than 600 mAh/g, which is much higher than the theoretical capacity of graphite anode which is limited to only 372 mAh/g [24]. This has aroused new interest in the research on alloy based compounds as alternative anode material for Li-ion batteries based on the concept that electrochemical lithium insertion into an active metal centre which is embedded in a composite matrix or into transition metal intermetallics.

Few details were provided to explain the electrochemical mechanism of tin based oxide anode by Courtney and Dahn [25], [26]. They proposed a mechanism on the lithium reaction with tin oxide (SnO and SnO₂) anode based on their studies using *in-situ* X-ray diffraction [25], [26]. This mechanism comprise of two electrochemical reaction. In the first step, tin oxide reacts with Li to form an amorphous lithium oxide (Li₂O) phase and the reduced form of metallic Sn. The newly formed Sn particles further react with Li to form Li-Sn alloy up to the composition of SnLi_{4.4} [25]. The simplified electrochemical reactions are represented as follows [25];



The reversible reaction in the Sn oxide-based anodes as shown in Equation (2.8), involves the alloying and de-alloying of Li with very small grains of Sn, while Li₂O phase formed during the first discharge and the other components in the glass remains inert during the subsequent cycles. The reaction in the first step to form the Li₂O phase (Equation (2.7)) is irreversible and result in large irreversible loss. Despite this, the irreversible, amorphous Li₂O phase serves as a binding medium that resists the cracking of the electrode induced by the large volumetric change occurring in the Sn-Li alloys during cycling [25], [26]. Courtney and Dahn further studied the reaction of lithium with tin oxide composite glass [26]. The electrochemical reactions are represented as follows;



The active component in this type of anode is the tin oxide whereas the other components act as spectators. The spectator ions here are the glass network formers such as Boron (B) and Phosphorus (P), have been presumed to be inert to

electrochemical reaction, serving to prevent aggregation of Sn atoms during repeated cycles of charging and discharging [26]. This leads to improved cyclability in comparison to the use of pure Sn metal as the anode.

The Stalion[®] battery however was never commercialized despite of its earlier announcement. This was most likely due to poor prolonged cycling performance and the large, irreversible capacity loss during the first cycle. In February 2005, Sony Corporation announced its first hybrid Li-ion battery dubbed as the Nexelion[™] batteries in its press release [27]. This new battery utilizes a tin-based amorphous material and is reported to deliver 30% increase in capacity per volume ratio compared to conventional Li-ion battery which uses graphite-based materials for the anode. The newly developed tin-based amorphous anode consists of multiple elements such as tin, cobalt and carbon which are mixed in nanometer level. The presence of several elements in the tin-based anode was claimed to be able to minimize the change in particle shape during charge and discharge [27].

2.4.4 Tin-Based Intermetallics

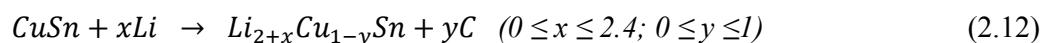
The concept suggested by Huggins *et al.* [6], [22] was applied by Dahn's group in their study on iron-tin (Sn_2Fe) compound as anode material [28], [29]. This concept involves using an intermetallic compound, MM' where M is the active element that alloys with Li while M' is the inactive element that serves as a matrix that surrounds the active element. The role of the inactive matrix also serves to absorb massive volume changes that occur within the anode upon lithiation (expansion) and delithiation (contraction) processes. Sn_2Fe decomposed to nano-sized iron and form lithium-tin alloy upon reaction with lithium. The Li_xSn ($x \leq 4.4$) alloy is surrounded by elemental Fe. The fine Fe atoms do not alloy with lithium but acts as inactive matrix and supports the intergrain electronic contact in the material. During the delithiation process, Fe atoms aid Li removal by reacting with Sn to reform small grains of Sn_2Fe . However, due to large volume expansion during reaction with Li, some Sn regions gradually lose connection, leading to an incomplete reformation of the starting

material. This compound exhibited high specific capacities of 800 mAh/g and 650 mAh/g during the first discharge and charge cycle, respectively. However, upon long term cycling, significant loss of capacity was observed.

Tackeray *et al.* studied the copper-tin (Cu_6Sn_5) intermetallic insertion compound [30], [31]. Their approach which is similar to the one taken by Dahn's group [28], [29], which is also based on the concept as proposed by Huggins *et al.* [6], [22] in utilizing an intermetallic compound, MM' . The Cu_6Sn_5 hexagonal structure comprises of layers of tin atoms sandwiched between sheets of copper atoms [30]. Initial reaction of Cu_6Sn_5 with lithium follows according to this reaction [6];



During the reaction with lithium, half of the tin atoms are displaced to form columns of tin, while copper and the other half of tin atoms remain spatially intact, creating small hexagonal channels in which lithium can be inserted to form Li_2CuSn [6], [30]-[31]. They discovered that this intermetallic compound is capable of topotactic lithium intercalation. This topotactic reaction is accompanied by a volume expansion of 61% [6], [30], [31]. Further lithiation of Li_2CuSn results in the extrusion of the remaining copper atoms from the structure before $\text{Li}_{4.4}\text{Sn}$ is formed at around 0.4V [6]. This reaction can be represented as;



In principle, the Cu_6Sn_5 insertion intermetallic compound can exhibit high specific capacity without the drawback of massive volume expansion problems associated with alloy formation.

Besenhard's team also studied the 'mixed conductor matrix' concept as suggested by Huggins *et al.* [6], [22] by taking on a different approach in studying an all active multiphase compound, SnSb as anode material [21], [32], [33]. The multiphase compound, SnSb has two active phases which have different potentials for the onset of lithium alloying reaction [27]. In the initial reaction, Li is inserted into the Sb host

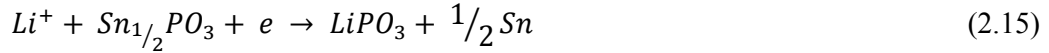
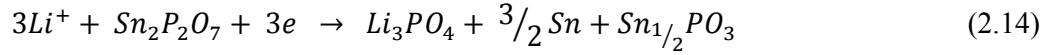
structure to form Li_3Sb whereas tin is displaced from the structure [21], [32], [33]. This can be represented by the reaction below;



When a certain potential is reached, the more reactive phase will react first whereas the other remains ductile and can buffer the expansion of the first phase. Once the Li_3Sb domain is completely formed, the remaining Sn particles react further with Li to form Li_xSn alloy [32]. During the Li removal (charging) process, the SnSb phase is restored. The good cyclability of this compound can be attributed to the fact that both component react sequentially where Li_3Sb formation takes place at ~ 0.8 - 0.85 V vs Li^+/Li which is then followed by Li_xSn alloy formation at ~ 0.65 - 0.7 V [32]. Therefore, at each step of the reaction, the lithiated phase is embedded in an inactive matrix. It is believed that the continuous phase separation and restoration during cycling could to some extent counteract the aggregation of finely dispersed Sn to large Sn regions, which leads to an increase in volume changes [21], [32]. However, low voltage reaction involving formation of tin alloys result in further electrode expansion and loss of interparticle contact between Li_3Sb and Sn causing irreversibility and capacity fading [33].

2.4.5 Tin Phosphate

Work on crystalline and amorphous forms of tin pyrophosphate ($\text{Sn}_2\text{P}_2\text{O}_7$) by Xiao *et al.* [7] shown that the amorphous version showed better performance. Amorphous $\text{Sn}_2\text{P}_2\text{O}_7$ was prepared by melt quenching the crystalline $\text{Sn}_2\text{P}_2\text{O}_7$. The first discharge curve is similar to the reaction mechanism of the tin based oxide with lithium as discussed in the earlier section (2.4.3) by reduction of the tin phosphate to tin and followed by reversible Li-Sn alloying and de-alloying reactions. The reduction reaction in the first cycle was proposed to proceed as follows [7];



It was found that $\text{P}_2\text{O}_7^{2-}$ dissociates in PO_4^{3-} and PO_3^- after repeated cycling based on investigation using Infra-red spectroscopy [7]. The tin atoms dispersed in Li_3PO_4 and LiPO_3 networks are hosts for further reversible Li-Sn alloying and de-alloying reaction. The proposed reversible alloying and dealloying reaction of Li-Sn is similar to the reversible reaction for tin oxide based anode material as represented in Equation (2.8). Xiao *et al.* found that the amorphous and crystalline $\text{Sn}_2\text{P}_2\text{O}_7$ delivered reversible capacities of 520 mAh/g and 400 mAh/g, respectively [7]. A higher potential was required for complete extraction of Li^+ in crystalline $\text{Sn}_2\text{P}_2\text{O}_7$ which explains the lower capacity obtained from this polymorph.

Wan *et al.* [34] reported the charge-discharge performance of amorphous tin phosphate ($\text{Sn}_2\text{P}_2\text{O}_7$) prepared from different heat treatment temperatures of 500, 550, 600 and 700°C and tin phosphate incorporated with manganese. It was found that tin phosphate synthesized from thermal decomposition of tin (II) hydrogen phosphate at 700°C recovered a reversible capacity of around 500 mAh/g from its initial discharge capacity of around 1020 mAh/g. This anode suffered a 50% loss in irreversible capacity. The $\text{SnMn}_{0.5}\text{PO}_4$ prepared at 700°C exhibited initial discharge capacity of

635 mAh/g followed by a reversible capacity of around 470 mAh/g. This manganese doped tin phosphate only experienced 26% loss in irreversible capacity.

Tirado and Vicente's research group [35] studied the performance of an orthorhombic tin (II) phosphate chloride ($\text{Sn}_2\text{PO}_4\text{Cl}$) electrochemical behaviour as anode material. The structure of $\text{Sn}_2\text{PO}_4\text{Cl}$ resembles that of SnO , difference being the chlorine atoms are located in the interlayer space. The product after the first discharge was considered a matrix of LiCl and Li_3PO_4 that finely disperses Sn-Li alloys. The presence of chlorine does not affect the reduction of tin. The phosphate group suffers limited volume changes on cycling. Capacity retention stabilizes after a decrease during the first ten cycles which is attributed to the increase in the size of tin domains. The reversible capacities remain close to 300 mAh/g for up to 40 cycles.

Behm and Irvine investigated the influence of the structure and composition of different tin phosphates on their electrochemical performance as anode material [36]. The materials studied were crystalline cubic and layered SnP_2O_7 , $\text{LiSn}_2(\text{PO}_4)_3$, $\text{Sn}_2\text{P}_2\text{O}_7$ and $\text{Sn}_3(\text{PO}_4)_2$ and amorphous Sn_2BPO_6 . The best result was obtained with a cubic SnP_2O_7 anode which showed an initial reversible capacity of more than 360 mAh/g and the ability to retain 96% of the initial reversible capacity when cycled up to 50 cycles between 0.02 and 1.2 V vs. Li^+/Li but when further cycled to more than 100 cycles, capacity retention sank to 75% [36]. Capacity retention in these phosphate systems was found to be better for the Sn (IV) starting materials than for Sn (II) starting materials. This was partly explained by higher proportion of inert matrix. If the active tin particles are dispersed well in the inactive matrix, the aggregation of tin will be slowed down. The higher spectator atoms to tin ratio leads the tin atoms to be farther apart thus decreasing formation of tin clusters thereby improving capacity retention. The cubic SnP_2O_7 cycled better than its layered polymorph, which showed that the structure of the initially inserted matrix of the starting material influences the capacity retention [36]. Another important conclusion drawn from this study is that it is not necessary for the starting material to be amorphous, or if crystalline, to have small grain size in order to have good cyclability [36].

2.5 Potential of Mesoporous Tin Phosphate as Anode Material in Lithium-Ion Battery

Large losses in irreversible capacity of tin oxide based anode have often been associated with the formation of irreversible phases such as Li_2O and volume changes resulting from repeated reversible alloying and de-alloying of Li-Sn reactions. Despite these disadvantages, tin based anodes are still widely investigated because of its high gravimetric and volumetric capacity. Different approaches have been taken to retain its high capacity and relieve mechanical strain during cycling by resorting to modifying structure and morphology and using multi-component tin based composite materials [20]-[36].

Porous materials may be regarded as crystalline or amorphous solids which permit the reversible passage of molecules (gas, liquid, solid) through their structures via holes in their surface. Pore dimensions cover a very wide range and according to the International Union of Pure and Applied Chemistry (IUPAC), pores are classified into three main groups depending on the pore size: where pore size between 0.7 to 2 nm are termed micropore, those between 2 and 50 nm are termed mesopores, and those greater than 50 nm are termed macropores [37]. Since the discovery of M41S silicates by Mobil's scientists in 1992, mesoporous material, possessing large internal surface area and narrow pore size distribution, have attracted considerable attention for their potential application as molecular sieves, catalysts, absorbents and host materials [38]. The mesoporous materials are mostly derived with supramolecular assemblies of surfactant which acted as templates of the inorganic components during synthesis. In the broadest sense, a template may be defined as a central structure within which a network forms in such a way that removal of the template creates a filled cavity with morphological related to those of the template [39]. Surfactants have been shown to organize silica into a variety of mesoporous forms, through the mediation of electrostatic, hydrogen-bonding, covalent and van der Waals interactions [40]. Surfactants are usually organic compounds that are amphiphilic in nature. Amphiphilic means they contain both hydrophobic group (tails) and hydrophilic groups (heads). Therefore they are both soluble in both organic solvents and water.

Generally a clear homogeneous solution for surfactants in water is required to obtain ordered mesostructures. Surfactants can be classified as cationic, anionic and non-ionic surfactants [39], [40].

The surfactant templating technique in synthesizing mesostructured materials has been extended to metal oxides, sulfides and phosphates. Over the past decades, the phosphates of tetravalent metals have been extensively studied because of their potential application in ion exchange, proton conductors, sensors and catalysis [41]. Layered tin phosphates are particularly interesting because of their structural flexibility and they have been widely applied in ion exchange, catalysis, encapsulation of semiconductor particles and electrical conductivity [41]. Recently, Kim *et al.* published an exciting report on the performance of mesoporous tin phosphate as anode component for Li-ion battery [42]. They prepared mesoporous/crystalline tin phosphate composite using cetyltrimethylammonium (CTAB) surfactant and found that it exhibited higher reversible capacity of around 580 mAh/g [42]. They suggested that tin phosphate was first decomposed to an active $\text{Li}_{4.4}\text{Sn}$ alloy and an inactive amorphous lithium phosphate phase which serves as a supporting matrix [42]. The highlight of this report was the claim that the synthesized mesoporous/crystalline tin phosphate exhibited reversible pore expansion and contraction during the Li insertion and extraction reaction. This reversible pore change was said to be able to minimize volume changes effects often associated with tin based anodes [42].

The requirement for the starting anode material to be amorphous is hard to understand since different studies as cited earlier [7], [23]-[26], [28]-[36], have showed that even crystalline materials lose their long-range order and become amorphous when they are electrochemically lithiated. The most important factor should be that the starting material when lithiated attains a structure and composition that it manages to stop tin from aggregating while it still allows transport of lithium ions and electrons. It is important to continue efforts to understand why certain structures and compositions of tin phosphate anode could impart higher capacity and better cycling performance.

Phosphates of tetravalent metals were claimed to possess promising physical and chemical properties such as outstanding superionic interlayer conductivity, improved capacity as intercalation compound and noteworthy electrical conductivity of the solid matrix [43]. These criteria motivate efforts to research the potential of mesoporous tin phosphate as anode host material for Li-ion battery. The approach taken to improve the structural stability in order to achieve satisfactory cycling performance was to incorporate a mesoporous framework in the tin phosphate anode to relieve mechanical strain during charging and discharging cycles. The lamellar structured mesoporous tin phosphate has not been widely studied of its electrochemical behavior with lithium. The lamellar, mesoporous tin phosphate in this work has been synthesized via an anionic surfactant (sodium dodecyl sulfate) templating method. This thesis deliberates on the electrochemical behavior of mesoporous tin (IV) phosphate upon reaction with lithium.

CHAPTER 3

METHOD OF INVESTIGATION

3.1 Overview

The methodology of this study systematically covers four research phases as described by the flowchart shown in Figure 3.1.

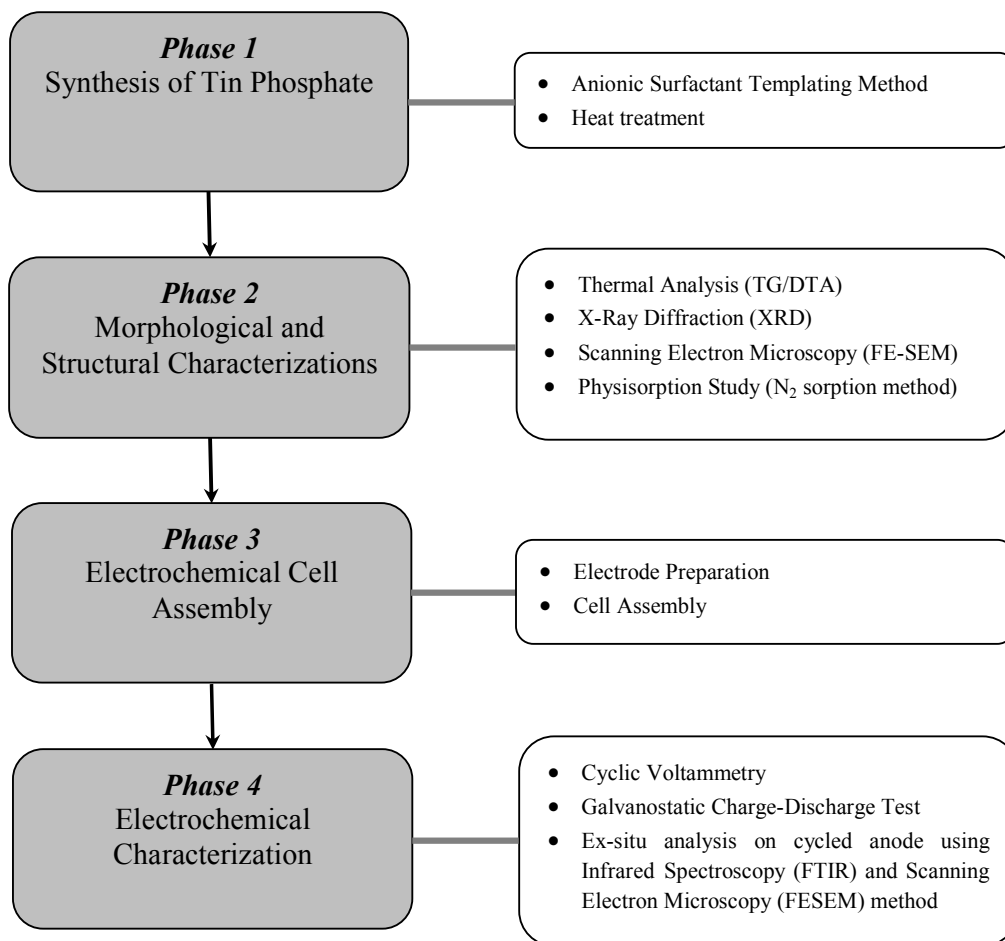


Figure 3.1: Flowchart on research phase and experimental techniques applied.

Phase 1 covers the synthesis of the tin phosphate material, Phase 2 covers morphological and structural characterization of tin phosphate, Phase 3 covers electrochemical cell assembly of tin phosphate anodes and subsequently followed by Phase 4 which covers electrochemical characterization of tin phosphate anodes.

3.2 Materials and Chemicals

Details of materials and chemicals used in this experiment are stated in Table 3.1. Chemicals supplied for this experiment were reagent grade. All chemicals were used as received, without further purification.

Table 3.1: Materials and chemicals used

Materials/Chemicals	Formula	Purity	Supplier
Tin tetra-chloride	SnCl_4	99%	Sigma-Aldrich
Sodium dodecyl sulfate	$\text{NaCl}_2\text{H}_{25}\text{SO}_4$	99%	Sigma-Aldrich
Orto-Phosphoric acid	H_3PO_4	86%	J.T. Baker
Ethanol	$\text{C}_2\text{H}_5\text{OH}$	99.7%	R&M Chemicals
Lithium foil (thickness = $\pm 0.75\text{mm}$)	Li	99.9%	Sigma-Aldrich
Lithium hexa-florophosphate in ethylene carbonate: di-methyl carbonate (1:1, v/v)	LiPF_6 in EC:DMC	-	Mitsubishi Chemical Corporation
Teflonized acetylene black	C	-	Timcal Co. Ltd
Glass microfiber filters (ϕ 20 mm)	-	-	Whatman

3.3 Synthesis of Mesoporous Tin Phosphate by Sodium Dodecyl Sulfate Templating Method

Mesoporous tin phosphates were synthesized via a surfactant templating method in aqueous solution. This research focused on the usage of an anionic surfactant, sodium dodecyl sulfate, as the templating surfactant. Mesoporous tin (IV) phosphate was synthesized by reacting aqueous solution of tin tetrachloride (SnCl_4), sodium dodecyl sulfate (SDS, $\text{NaCl}_2\text{H}_{25}\text{SO}_4$) and ortho-phosphoric acid (H_3PO_4) based on molar ratio of 1:1:4. As SnCl_4 is an extremely reactive and corrosive chemical, the synthesis procedure was carried in an Argon-filled glove box (MBraun), under room temperature at 25°C, for safety purpose.

Aqueous solution of SDS was prepared by adding 5.625 g of SDS into distilled-deionized water (DDW) to make 20 ml solution. A cloudy white solution was formed. The solution was continuously stirred until it turned into a transparent solution. Phosphoric acid was diluted by adding 4 ml H_3PO_4 to make a 20 ml dilution. The SDS solution was poured into the diluted H_3PO_4 solution while maintaining stirring. The aqueous SnCl_4 solution was prepared by adding 2.35 ml of SnCl_4 into DDW to make 20 ml solution. White fumes were emitted during this process. This solution was mixed shortly before being transferred into a pipette. The SnCl_4 aqueous was added drop-wise from a pipette into the SDS- H_3PO_4 solution with vigorous stirring. An exothermic reaction took place during this process as the beaker was found to be warm to touch. After the addition of around 10 ml of SnCl_4 aqueous solution, the mixed solution starts to turn cloudy. This may indicate initial formation of precipitate. Further addition of SnCl_4 solution resulted in a more cloudy and viscous solution. Upon completion of SnCl_4 solution addition into the SDS- H_3PO_4 solution, a thick, whitish gel was formed. This mixture was left with vigorous stirring overnight. The resulting mixture was then taken out of the glove box and placed into a Teflon lined stainless steel vial and then loaded into an autoclave and kept at 100°C for 5 days. After cooling to room temperature, precipitates formed during the aging process was recovered by filtration, followed by repeated washing with distilled water, and then dried in a vacuum oven at 100°C for 2 days. The as-prepared powder were grounded

and calcined at 200, 300, 400 and 500°C for 2 hours, yielding mesoporous tin phosphate. The synthesis procedure is simplified in a flow chart shown in Figure 3.2.

For reference purpose, a non-mesoporous tin phosphate was prepared without the presence of the SDS surfactant in the glove box. Aqueous solution of SnCl_4 was slowly added into the stirring H_3PO_4 solution, based on molar ratio of 1:3. This mixture turned cloudy and became more viscous. This mixture was left for continuous stirring overnight before taken out from the glove box. The resulting thick solution was transferred into a Teflon lined stainless steel vial and then loaded into an autoclave and kept at 100°C for 5 days. Upon cooling to room temperature, precipitates were washed and filtered and then in a vacuum oven at 100°C for 2 days. The as-prepared powder were then grounded and calcined at 200, 300, 400 and 500°C for 2 hours.

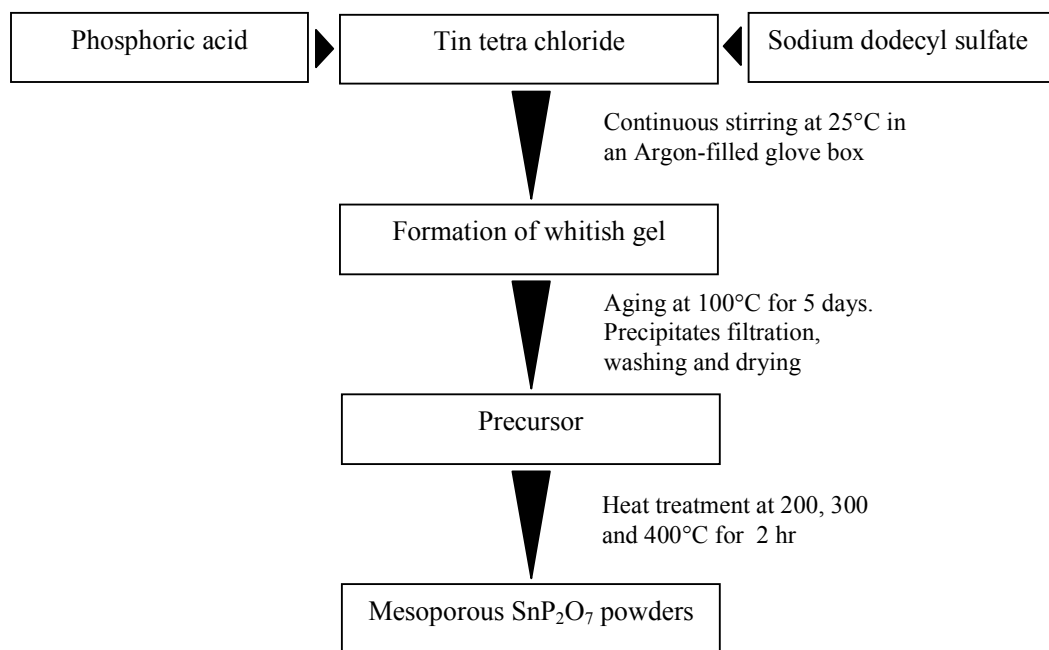


Figure 3.2: Flowchart on the synthesis of mesoporous SnP_2O_7 by surfactant templating method.

3.4 Methods of Characterization

The produced mesostructured and non-mesostructured tin phosphate batches were subjected to structural and morphological characterizations by means of thermal analysis, powder x-ray diffraction and scanning electron microscopy coupled with energy dispersive x-ray methods. Mesoporous structure of tin phosphate was further investigated using physisorption methods based on Brunauer-Emmett-Teller theory. Ex-situ characterizations on the tin phosphate anodes after electrochemical tests were carried out by means of Fourier transform infrared spectroscopy and scanning electron microscope. The following sections cover brief explanations on the techniques used in this experiment.

3.4.1 Thermal Analysis

Thermal analysis is a branch of materials science where the properties of materials are studied as they change with temperature. In this study, thermal behavior of tin phosphate was investigated using thermogravimetric-differential thermal analysis (TG-DTA) method. Thermal analyses of the as-synthesized oven dried tin phosphate powder were carried out with an EXSTAR TG/DTA 6300 thermal analyzer (SII NanoTechnology Inc, Japan). All measurements were carried out under static air condition with sample mass of less than 10 mg placed in a platinum pan. The heating profile consisted of a 5°C/min linear ramp from 30°C to 800°C. The TG-DTA data was analyzed using the EXSTAR 6000 software.

3.4.2 Powder X-Ray Diffraction

Powder X-ray diffraction is a technique used to characterize crystallographic structure, crystallite size and preferred orientation in polycrystalline or powdered solid samples. The wavelength of X-rays is comparable to the size of atoms; therefore they are ideally suited for probing the structural arrangement of atoms and molecules in a wide range of materials [44]. This technique provides information on types and

nature of crystalline phases, degree of crystallinity, amorphous phase, micro-strain and size of crystallites.

Diffraction is one of the most basic phenomena occurring when a wave interacts with an obstacle. When applied to the study of solid matter, Bragg's diffraction is generally considered. In this type of diffraction, the crystal structure of solid acts as a three dimensional grating. The waves scattered at various angles interact between them and the resulting diffracted waves have a maximum intensity when they satisfy the famous Bragg's law [44] :

$$2d \sin \theta = n\lambda \quad (3.1)$$

(where d is the distance between two inter-atomic planes, θ is the angle at which the radiation hits the crystal and λ is the wavelength of the radiation).

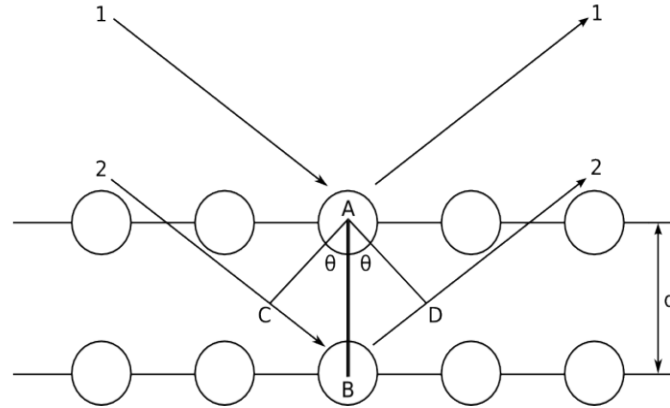


Figure 3.3: Schematic representation of Bragg's law (adapted from [44]).

Bragg's law can be easily derived graphically, as shown in Figure 3.3 [44]. Considering two rows of atoms, the distance between them (AB) is equal to the interplanary distance, d . In order to have constructive interference between waves 1 and 2, scattered by the two planes, it is needed that the additional path travelled by wave 2 is an integer number of wavelengths. It is possible to write $BC + BD = n\lambda$ and BC and BD can be estimated from trigonometry as $BC = BD = d \sin \theta$. Therefore,

Bragg's law is obtained as $2d \sin \theta = n\lambda$ [44]. The characteristic set of d-spacings generated in a X-ray diffraction pattern provides a unique 'fingerprint' of the materials present in the sample. When compared with standard reference patterns, this 'fingerprint' allows for identification of the material.

All materials prepared in this work have been characterized by powder X-ray diffraction (XRD) using a Bruker D8 Advance Diffractometer (40kV, 40 mA) with monochromatized Cu K α radiation source. The wavelength of the incident X-rays was 1.54060 Å and data were collected with a step size of 0.02° and a time per step of 1second. Low angle diffraction with a 2 θ range of 1-10° was employed to investigate the long range order of the synthesized mesoporous tin phosphate. A higher angle XRD pattern with 2 θ range of 10-80° was applied to further investigate and identify the crystallographic structure of the prepared powders. All XRD patterns were analyzed using the Diffrac Plus EVA version 9 software and further matched with the existing structural data from Powder Diffraction File database of the International Centre for Diffraction Data (ICDD).

3.4.3 Field-Emission Scanning Electron Microscope

The scanning electron microscope (SEM) is a type of electron microscope that images sample surface by scanning it with a high-energy beam of electrons in a raster scan pattern [45]. The electrons interact with the atoms that make up the sample and produce signals that contain information about the sample's surface morphology. The types of signals produced by SEM include secondary electrons, back-scattered electrons, characteristic X-rays, light, specimen current and transmitted electrons [45]. Secondary electron detectors are common in all SEMs but it is rare that one equipment would have detectors for all possible signals. In most common detection mode, secondary electron imaging can produce very high resolution images of a sample surface, revealing details about less than 5 nm in size. Due to very narrow electron beam, SEM micrographs have a large depth of field yielding a characteristic

three-dimensional appearance useful for understanding the surface structure of a sample.

Field-emission scanning electron microscope (FE-SEM) is a high-resolution imaging technique which provides topographical and structural information [45]. The FESEM can be classified as a high vacuum instrument (less than 1×10^{-7} Pa). The vacuum allows electron movement along the column without scattering and helps prevent discharges inside the instrument [45]. The vacuum design is a function of the electron source due to its influence on the cathode emitter lifetime [45]. Emitter type is the main difference between the SEM and the FESEM. There are two classes of emission source: thermionic emitter and field emitter. Thermionic emitters use electrical current to heat up a filament; the two most common materials used for filaments are Tungsten (W) and Lanthanum Hexaboride (LaB_6) [45]. When the heat is enough to overcome the work function of the filament material, the electrons can escape from the material [45]. Thermionic sources have relative low brightness, experiences cathode material evaporation and thermal drift during operation [45]. Field emission is one way of generating electrons that avoids these problems. A Field Emission Source (FES), also called a cold cathode field emitter, does not heat the filament. The emission is reached by placing the filament in a huge electrical potential gradient. The FES is usually a wire of Tungsten (W) fashioned into a sharp point. The significance of the small tip radius (~ 100 nm) is that an electric field can be concentrated to an extreme level, becoming so big that the work function of the material is lowered and electrons can leave the cathode [45]. FESEM that uses FES produces cleaner images, less electrostatic distortions and spatial resolution of less than 2 nm (which is three to six times better than SEM) [45].

In this study, a FE-SEM (LEO Gemini 1530) was used for inspecting morphology of the prepared tin phosphate samples. Prior to imaging analysis, samples were prepared by depositing a thin layer of gold (Au) on the surface using a POLARON Sputter Coater SC7640, mini sputtering system.

3.4.4 Physisorption Study

The characterization of amorphous networked materials is problematic because the structure of the materials is enormously complex. Most porous materials have amorphous structure. Pore shape is mainly unknown but it could be approximated by an appropriate model. Three basic pore models exist are; cylindrical pores, ink-bottle pores and slit-shaped pores [46]. Gas adsorption method plays an important role in the characterization of a wide range of porous materials. Gas adsorption methods allow probing of entire surface area of solid including irregularities and pore interiors [46]. Physical gas adsorption (physisorption) is a preferred technique to study porous characteristics of solid materials therefore this technique is chosen to investigate the mesoporous structure of the prepared tin phosphate. The isotherm obtained from these adsorption measurements provides information on the surface area, pore volume and pore size distribution. Nitrogen (N_2) adsorption at 77K and at sub-atmospheric pressures is the most popular technique, providing information on size distributions in the micro-, meso- and macroporosity range [46].

Before performing gas sorption experiments, solid surfaces of the powders must be freed from contaminants such as water and oils by means of a surface cleaning method known as out-gassing. Out-gassing is often carried out by placing the sample in a glass cell and heating it under vacuum. Once clean, the sample is brought to a constant temperature by means of an external bath. Small amounts of a gas (*adsorbate*) are introduced in steps into the evacuated sample chamber. Adsorbate molecules quickly find their way to the surface of every pore in the solid (*adsorbent*). As more molecules are introduced into the system, the adsorbate molecules tend to form a thin layer that covers the entire adsorbent surface. Based on the well-known Brunauer, Emmett and Teller (B.E.T.) theory, one can estimate the number of molecules required to cover the adsorbent surface with a monolayer of adsorbed molecules, N_m [46], [47]. Multiplying N_m by the cross-sectional area of an adsorbate molecule yields the sample's surface area [46], [47]. Continued addition of gas molecules beyond monolayer formation leads to the gradual stacking of multiple layers (or multi-layers) on top of each other. As the equilibrium adsorbate pressure

approach saturation, the pores become completely filled with adsorbate. Knowing the density of the adsorbate, one can calculate the volume it occupies and, consequently, the total pore volume of the sample [46], [47]. If at this stage one reverses the adsorption process by withdrawing known amount of gas from the system in steps, one can also generate desorption isotherms. Adsorption and desorption isotherms rarely overlay each other. The resulting hysteresis leads to isotherm shapes that can be mechanistically related to those expected from particular pore shapes. Computational methods such as Barrett, Joyner and Halenda (BJH) allow the determination of pore sizes from equilibrium gas pressures, as simply given by the equation below [46], [47];

$$\text{Average Pore Diameter} = \frac{4V_p}{S_{BJH}} \quad (3.2)$$

where V_p is the mesopore volume and S_{BJH} is the BJH specific surface area.

Surface area measurements and pore size distribution of the synthesized mesoporous tin phosphates in this study were evaluated using the physisorption technique. Physisorption of nitrogen (N_2) at the temperature of liquid nitrogen, 77K on the samples were conducted using an automatic Quantachrome Autosorb-1C gas sorption apparatus. Powders were weighed, placed in a PyrexTM glass tube and fitted into the chamber of the equipment and out-gassed at 150°C under N_2 gas flow overnight (± 18 h) prior to measurement. The N_2 adsorption-desorption isotherms were measure within a relative pressure of P/P_o ranging between 0.05 to 0.975, where P is the absolute pressure and P_o is the vapor saturation pressure of pure N_2 at temperature of the measurement. Surface areas (BET area) were obtained using the multipoint BET method. Pore size distributions were analyzed by the BJH method.

3.4.5. Fourier Transform Infrared Spectroscopy

Spectroscopy is the measurement of a quantity as a function of either wavelength or frequency. Infrared spectroscopy utilizes the fact that molecules have specific frequencies at which they rotate or vibrate corresponding to discrete energy levels [48]. In infrared spectroscopy, infrared radiation is passed through a sample where some are absorbed by the sample and some of it is passed through (transmitted). The resulting spectrum represents the molecular absorption and transmission, creating a molecular fingerprint of the sample [48]. The peaks in the spectrum correspond to the frequencies of vibrations between the bonds of the atoms making up the compound [48]. Because each different compound is a unique combination of atoms, no two compounds produce the exact same infrared spectrum [48]. Fourier Transform Infrared Spectroscopy (FTIR), like other forms of spectrometry, can be used to identify compounds or investigate sample composition.

When a material is irradiated with infrared radiation, absorbed IR radiation usually excites molecules into a higher vibrational state. The wavelength of light absorbed by a particular molecule is a function of the energy difference between the at-rest and excited vibrational states [48]. The wavelengths that are absorbed by the sample are characteristic of its molecular structure. The FTIR spectrometer uses an interferometer to modulate the wavelength from a broadband infrared source [48]. A detector measures the intensity of transmitted or reflected light as a function of its wavelength [48]. The signal obtained from the detector is an interferogram, which must be analyzed with a computer using Fourier transforms to obtain a single-beam infrared spectrum [48]. The FTIR spectra are usually presented as plots of intensity versus wavenumber (cm^{-1}). Wavenumber is the reciprocal of the wavelength. The intensity can be plotted as the percentage of light transmittance or absorbance at each wavenumber. The plotted IR spectrum is compared with standard spectra in computer databases or with a spectrum obtained from a known material, in order to identify the material of the specimen. Absorption bands in the range of $4000\text{-}1500\text{ cm}^{-1}$ are typically due to functional groups (e.g., -OH , C=O , N-H , CH_3 , etc.) [48]. The region from $1500\text{ - }400\text{ cm}^{-1}$ is referred to as the fingerprint region [48]. Absorption bands in

this region are generally due to intramolecular phenomena and are highly specific to each material [48].

In this experiment, solid sample (~2 mg) is mixed with potassium bromide (KBr) to form a fine powder using an agate mortar. This powder is then compressed into a thin pellet. KBr is transparent in the IR region. FTIR spectra were measured using a Nicolet Magna 560 IR spectrometer with a resolution of 4 cm^{-1} .

3.5 Electrode Fabrication and Cell Assembly

The electrode was fabricated by mixing the synthesized tin phosphate powders with a conductive binder known as teflonized acetylene black (TAB) at a ratio of 80:20, in an agate mortar. Few micro-liter of ethanol was dropped into this mixture to aid the mixing process. The mixture was then spread uniformly onto stainless steel mesh, which serves as a current collector and pressed under a pressure of about 1500 psi in an uniaxial hydraulic press (Enerpac). For cyclic voltammetry measurement, samples were prepared with less than 10 mg of anode material, which was then spread and pressed onto a 50 mm^2 (5mm x 10mm) stainless steel mesh spot welded to a stainless steel wire of around 4 cm long. For galvanostatic charge-discharge performance tests, 20 mg of anode material was spread and pressed onto a 15 mm diameter stainless steel mesh. All pressed electrodes were dried in an oven at 120°C overnight before they were transported into an argon-filled glove box (Mbraun, Germany). Assembly of all electrochemical test cells was carried in a circulating argon (Ag) glove box where both moisture and oxygen contents were below 1 ppm each.

A three electrode custom designed electrochemical cell casing was fabricated for cyclic voltammetry characterization. Li foils were used as both counter and reference electrodes. The prepared anode acts as the working electrode. All three electrodes were immersed in a 1 M LiPF_6 in EC:DMC (1:1) electrolyte contained in a glass bottle, sealed with a NeopreneTM stopper. The schematic diagram of the three electrode cell assembly for cyclic voltammetry measurement is shown in Figure 3.4.

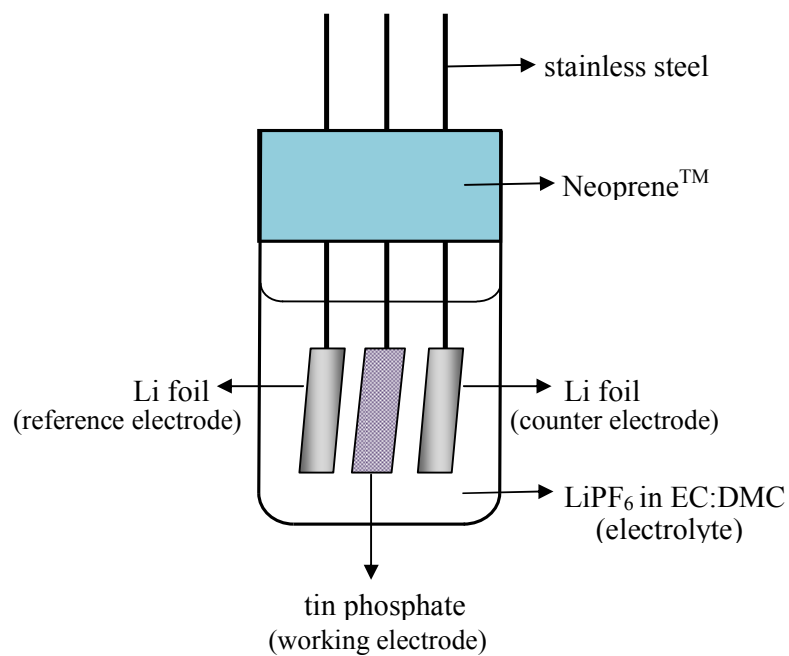


Figure 3.4: Schematic diagram of a three-electrode configuration electrochemical test cell.

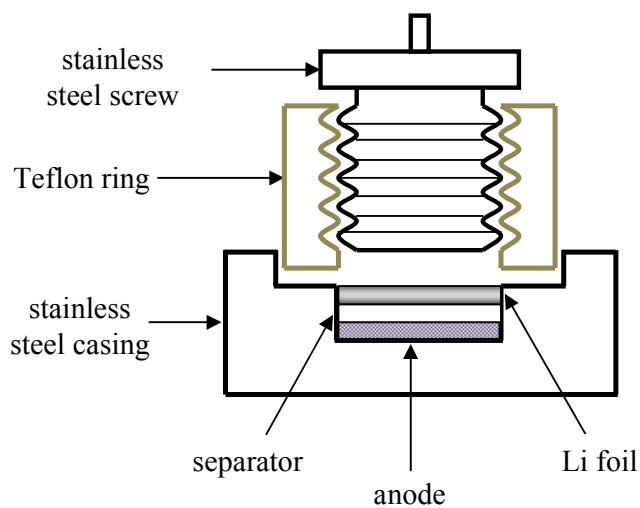


Figure 3.5: Schematic diagram of a two-electrode configuration electrochemical test cell.

Another custom designed electrochemical test cell was also fabricated to evaluate the charge-discharge cycle performance of the tin phosphate anode. The tin phosphate anode was assembled versus a Li foil as the counter electrode. A glass micro-fibre (ϕ 20 mm) which has been pre-soaked in 1 M LiPF_6 in EC:DMC (1:1, v/v) electrolyte, was used as a separator. This two electrode configuration (anode / LiPF_6 in EC:DMC / Li) is schematically represented in Figure 3.5. This cell is screwed in place before transferred out from the glove box.

3.6 Electrochemical Performance Assessment

3.6.1 Cyclic Voltammetry

Cyclic voltammetry (CV) is a simple electrochemical technique widely applied in the study of redox reactions of electrode in electrochemical cells. CV is a type of potentiodynamic electrochemical measurement, in which a voltage is applied to a working electrode and current flowing at the working electrode is plotted versus the applied voltage to give a cyclic voltammogram. This technique is performed by scanning the voltage between two chosen voltage limits and measuring the current response arising from any electron transfer process within the two voltage limits. This process is repeated for a desired number of cycles. The voltage limits will define the electrode reaction that takes place, therefore the starting voltage is preferentially chosen at a value where no electrode reaction will occur (open circuit voltage) and swept towards positive or negative potentials to investigate oxidation or reduction processes, respectively. The resulting potential measured between the reference electrode and working electrode and the current measured between the working electrode and counter electrode is the plotted as current (I) vs. potential (V) [49]. The forward scan produces a current peak for any analytes that can be reduced through the range of the potential scan. The current will increase as the potential reaches the reduction potential of the analyte, but then falls off as the concentration of the analyte is depleted close to the electrode surface. As the applied potential is reversed, it will

reach a potential that will re-oxidize the product formed in the first reduction reaction and produce a current of reverse polarity from the forward scan. This oxidation peak will usually have a similar shape to the reduction peak. The I-V response curves for a simple reversible electrode reaction are characterized by asymmetrical peaks.

In this work, CV measurements on the electrode samples were carried out with a Solartron 1287A Electrochemical Interface equipment. The configuration of the CV electrochemical cell is shown earlier in Figure 3.4. The three-electrode cell consists of the tin phosphate electrode as the working electrode and Li foils which were used as both counter and reference electrodes. This cell is connected to the equipment with alligator clips prior to cyclic voltammetry measurements. The potential was scanned between 0 and 2.0 V versus Li/Li⁺ at a rate of 0.100 mV/s for three cycles. The first scan always commenced cathodically from the rest potential or open circuit voltage (OCV). The voltametric responses of the samples were analyzed using a CorrWare version 2.3 (Scribner, Inc) software.

3.6.2 Galvanostatic Charge-Discharge Tests

Galvanostatic charge-discharge cycling tests were conducted on the electrochemical cells using the WonATech WBCS 3000 Battery Cycler System as shown in Figure 3.6. The custom-designed electrochemical cell with a two-electrode configuration (anode / LiPF₆ in EC:DMC / Li) as shown in Figure 3.5, is also known as a half-cell. Li foil is applied here as both counter and reference electrode. This half-cell is connected with alligator clips to a WonATech Battery Cycler System prior to galvanostatic charge-discharge tests, as shown in Figure 3.6 (b).

In order to use the full capacity of the active tin phosphate anode material, the test cell was initially discharged (lithium insertion) from OCV to 0 V (vs. Li/Li⁺) before being charged (lithium extraction) to the selected upper voltage limit. In this experiment, the battery cycler system was programmed using the equipment's software, WBCS English version 1.11. to perform galvanostatic discharge and charge

cycling to the pre-set potential limits of 0-1.2 V, 0-1.6 V and 0-2.0 V (vs. Li/Li^+) at a constant current of 0.5 mA. This current value was selected depending on the theoretical capacity and the active weight of the tin phosphate anode under investigation, as cited from literatures [7], [25], [26], [42]. Differential capacity analysis was carried out using the IVMAN DA software developed by WonATech. Differential capacity plots were constructed based on the charge-discharge data obtained earlier from the WBCS software.

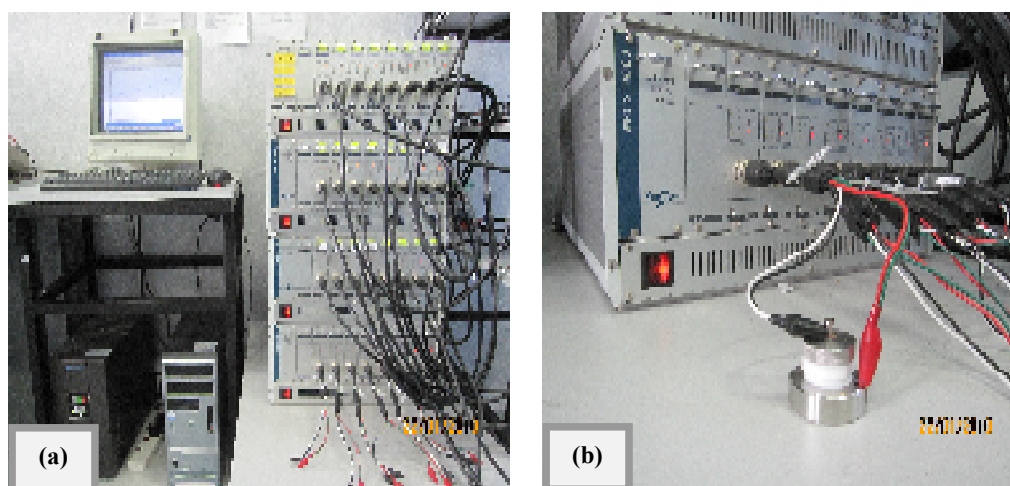


Figure 3.6: (a) WonATech WBCS Battery Cycler equipment, (b) A two-electrode electrochemical cell connected to the battery cycler equipment for galvanostatic cycling test.

CHAPTER 4

STRUCTURAL AND MORPHOLOGICAL CHARACTERIZATION OF TIN PHOSPHATE

4.1 Overview

This research work highlights the possible application of a lamellar, mesoporous structured tin phosphate as anode material in Li-ion batteries. In the first phase on this research, the lamellar, mesoporous tin phosphate was synthesized via a surfactant templating method where an anionic surfactant, sodium dodecyl sulfate (SDS) was used. For reference purpose, another batch of tin phosphate was synthesized in absence of the SDS surfactant. The next crucial phase of this research was to determine the physical characteristics of the tin phosphate batches produced. This chapter elaborates on the structural and morphological properties of both tin phosphate batches produced based on characterizations by means of Thermogravimetric-Differential Thermal Analysis (TG-DTA), powder X-Ray Diffraction (XRD), nitrogen physisorption and Field-Emission Scanning Electron Microscope (FESEM).

4.2 Synthesis of Mesoporous Tin Phosphate

Lamellar materials feature a number of important and interesting properties due to qualities induced by them by the addition of guest components placed within the interlayer spacing. Among interesting properties shown by these materials is the ability of these solids to host a variety of molecules in-between their interlayer spacing and that the lamellar structure can undergo reversible swelling [43].

Porous solids have high scientific and technological interest as well. They are able to interact with atoms, ions and molecules at surfaces and throughout the bulk material. Distribution of sizes, shapes and volumes of the void spaces in porous materials are directly related to their ability to perform desired function in a particular application.

Supramolecular arrays of amphiphiles led to mesostructures which can often be created by a variety of amphiphilic species; the resultant mesostructured products are periodically ordered by amorphous with respect to their short range atomic structure [50]. The main role of surfactants in the synthesis of mesostructured materials is to act out as templates or directing agents for the effective control of mesophase structures. In principle, the morphology of the solid is imposed by the tri-dimensional (3D) mesostructure of a surfactant, which acts as a nucleating agent and which is finally removed after the growth of the inorganic material [50].

In the synthesis of mesostructured materials, lamellar structures are often obtained from utilizing anionic surfactants [51]. Therefore, the anionic surfactant, sodium dodecyl sulfate was used as structure directing species in the synthesis of the mesoporous tin (IV) phosphate (SnP_2O_7) discussed in this study. The synthesis of lamellar or cubic tin phosphate phase strongly depends on the phosphoric acid to tin chloride (P:Sn) molar ratio. Phosphoric acid content of 4 molar leads to the formation of layered tin phosphate structure whereas phosphoric acid content of 16 molar leads to the formation of cubic tin phosphate [52].

Charge density matching between surfactant and the inorganic species is important for the formation of the organic-inorganic mesophases. Stucky and co-workers [53], [54] proposed a generalized mechanism of formation based on the specific type of electrostatic interaction between a given inorganic precursor, I and surfactant head group, S and by extension where a counterion, X was involved. Four general synthetic routes were suggested, which are S^+I^- , SI^+ , $\text{S}^+\text{X}\text{I}^+$ and $\text{S}^-\text{X}^+\text{I}^-$ (S^+ is the cationic surfactant, S^- is the anionic surfactant, I^+ is the inorganic precursors cation, I^- is the inorganic precursors anion, X^+ is the cationic counterion and X^- is the

anionic counterion) [53], [54]. To yield mesoporous materials it is important to adjust the chemistry of the surfactants headgroups which can fit the requirement of the inorganic components.

In this study, the mesoporous tin phosphate was synthesized using anionic surfactant (sodium dodecyl sulfate) and tin chloride (SnCl_4) as inorganic precursor under acidic condition from phosphoric acid source. Under low concentration, surfactant molecules usually exist in micellar forms, and no long-range organized surfactant structures exist [50]. Sodium dodecyl sulfate (SDS) is an anionic surfactant with a structural formula of $\text{CH}_3-(\text{CH}_2)_{11}-\text{O}-\text{SO}_3^{(-)} \text{Na}^{(+)}$. SDS contains the negatively charged ionic headgroup, OSO_3^- . This negatively charged headgroup interacts with the positively charged inorganic metal precursor (Sn^{4+}) following the S^-T^+ pathway. In this synthesis, phosphoric acid enhances electrostatic interactions between Sn^{4+} and surfactant assemblies. The aging process in this experiment was carried out at 100°C for 5 days to promote further assemblies of the inorganic-organic network and the formation of the rigid inorganic framework based on the Sn-O-P bonds. After this, the recovered resulting precipitates were removed of the SDS surfactant by means of heat-treatment in order to produce the mesoporous structure. It is often in such surfactant-assisted pathway, part of the surfactant headgroup is incorporated into the final material after heat treatment [50].

4.3 Thermal Analysis on Tin Phosphate

Thermal analysis study has been carried out to gain more information on the transformation that occurred during the heating of both batches of as-synthesized tin phosphate powders; one synthesized without the SDS surfactant, and the other with the SDS surfactant. The SDS synthesized tin phosphate was expected to produce mesoporous tin phosphate whereas that synthesized in the absence of the SDS serves as reference purpose. Thermal behavior of both samples in the temperature range of $30-800^\circ\text{C}$ was analyzed based thermogravimetric and differential thermal analysis (TG-DTA) method. The thermal analysis in this study was limited to 800°C because

phosphorus loss and decomposition of tin phosphate to tin oxide (SnO_2) occur above this temperature, as reported by C. Velásquez *et al.* [43].

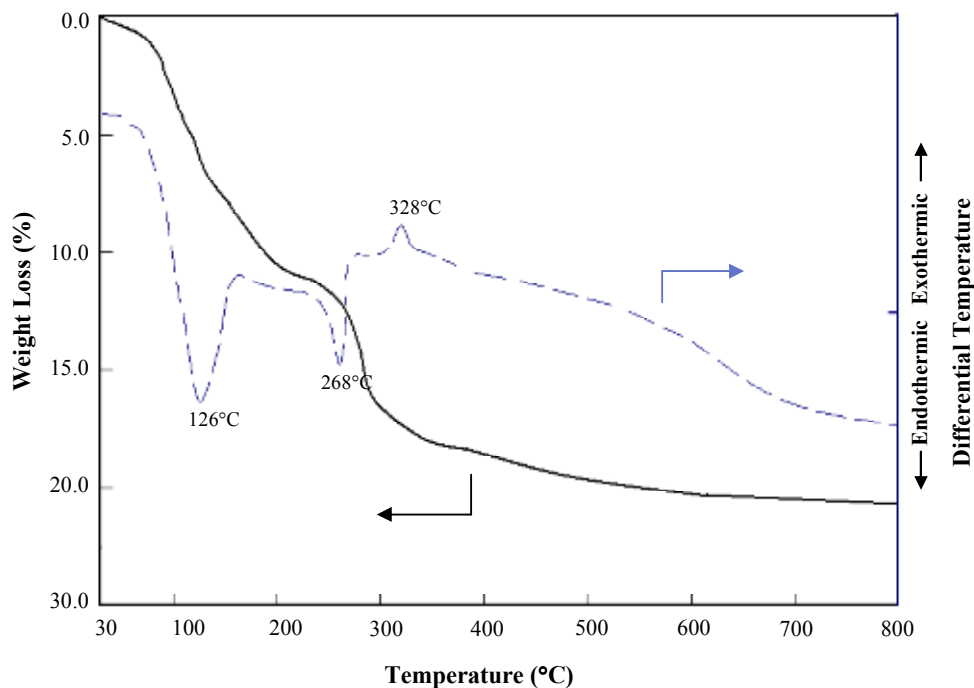


Figure 4.1: TG-DTA curves for tin phosphate.

The thermal behavior of tin phosphate synthesized without SDS surfactant is shown in Figure 4.1. There are three peaks observed in the DTA curve. The first peak centered at 126°C, is endothermic and was accompanied by a weight loss of about 11% within the temperature range of 70-200°C in the TG curve. This effect can be ascribed to the evaporation of moisture from the tin phosphate precursor. Subsequent weight loss of around 8% was recorded within 210-390°C on the TG curve. This loss was complemented with an endothermic peak at 268°C on the DTA curve. This weight loss may be attributed to structural water release due to dehydration of hydrogen phosphate (HPO_4) group [55]. Elimination of water molecules in crystallization water can occur at temperature higher than 100°C [56]. Traces of tin phosphate is initially present in the form of tin hydrogen phosphate ($\text{Sn}(\text{HPO}_4)_2$). The

condensation of phosphate group may occur at 328°C that causes $\text{Sn}(\text{HPO}_4)_2$ to be transformed into SnP_2O_7 , as represented in the reaction below;



The third peak observed on the DTA curve at 328°C is exothermic and this peak was not accompanied by appreciable weight loss in the TG curve. This incidence may be assigned to phase transition of tin phosphate from amorphous to crystalline [56]. Total mass loss of the as-synthesized tin phosphate recorded from 30-800°C was about 21%.

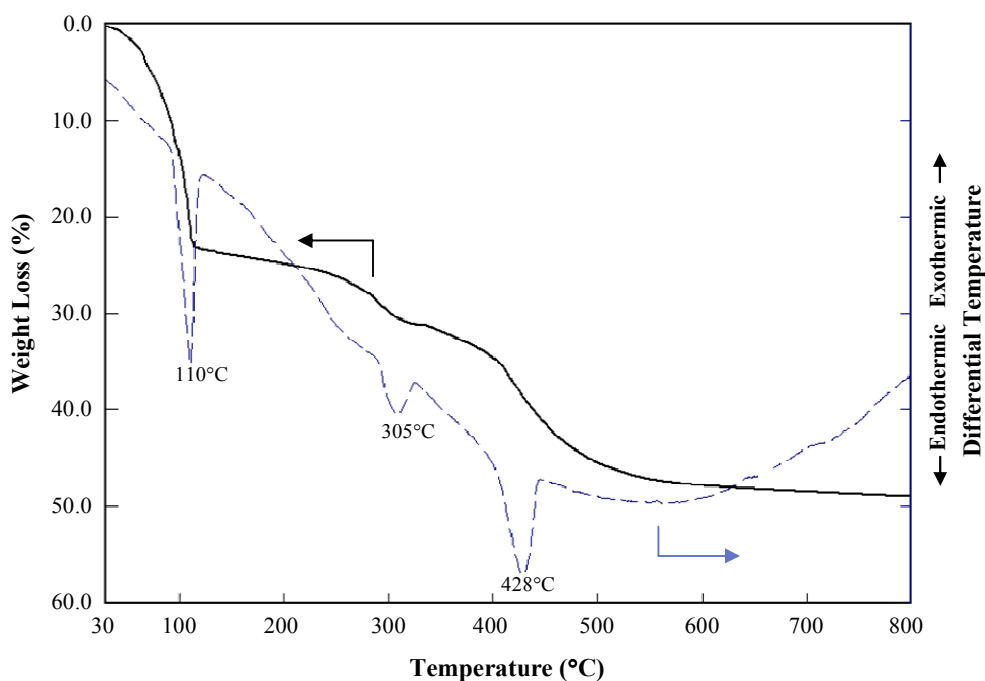


Figure 4.2: TG-DTA curves for surfactant synthesized tin phosphate.

Thermal analysis on tin phosphate synthesized with SDS surfactant is shown in Figure 4.2. This thermogram differs from the one observed for tin phosphate synthesized without SDS. There are three endothermic peaks observed in this DTA curve. The first endothermic peak around 110°C is accompanied by a weight loss of around 23%. This could be assigned to dehydration of absorbed moisture in the tin

phosphate precursor. A continuous and slow weight loss is observed around 115-400°C on the TG curve and a small endothermic peak was recorded at 305°C on the DTA curve. Possible causes for this weight loss may be due to release of coordinated water during the dehydration of HPO_4 group in $\text{Sn}(\text{HPO}_4)_2$ to form SnP_2O_7 . The temperature of this endothermic peak is slightly higher than the one observed for the reference tin phosphate in Figure 4.1 for the same effects, occurring at 268°C. Another explanation for this phenomenon is the possibility of another effect co-occurring around 305°C. This effect may be referred to the onset of the decomposition of the SDS surfactant which would lead to the dissociation and rearrangement of bonds between SDS surfactant and metal ions [50], [51] and [57]. A subsequent decline was observed further along the TG curve around the temperature of 420-500°C, resulting in a weight loss of 8%. The third endothermic peak was observed at 428°C. This peak may be contributed by the decomposition of SDS surfactant. It is postulated that SDS surfactant started to decompose around 300°C and was completely decomposed around 500°C as no significant weight loss is observed at a temperature above 500°C. A total mass loss of about 48% was recorded for the synthesized mesoporous tin phosphate. This is two times higher than the one recorded for non-mesoporous tin phosphate due to additional weight loss from decomposition of the SDS surfactant.

Based on TG-DTA analysis, it was observed that well defined weight loss accompanied by structural transformation occurs between 200° and 500°C for both mesoporous tin phosphate and non-mesoporous tin phosphate. In order to gain further insights on the structural changes, a series of physical characterization techniques were carried on both tin phosphate batches calcined at 200,300, 400 and 500°C. The following sections elaborate on the structural transformation of the synthesized tin phosphate upon calcination.

4.4 X-Ray Powder Diffraction Analysis on Tin Phosphate

The structure of both tin phosphates batches; one was synthesized using the SDS surfactant and the other without the surfactant, was studied by means of X-ray powder diffraction using a BRUKER D-8 Advance X-Ray powder diffractometer. X-ray diffraction (XRD) studies were performed on both batches of synthesized tin phosphates, which were each heat-treated at 200, 300, 400 and 500°C for 2 hours. The powder diffraction pattern of the samples were analyzed in two separate spectrums; one on the lower 2θ angle (1-10°) and the other on the higher 2θ angle (10-80°). Materials such as mesoporous and nano-materials feature very large d-spacing. Therefore, XRD measurements need to start at very low 2θ angles to unambiguously determine the crystalline structure and execute qualitative or quantitative phase identification. The lower 2θ angle powder diffraction pattern was employed here to detect the presence of mesostructure phase whereas the higher angle XRD pattern was used to further investigate and identify the crystallographic structure.

The powder diffraction patterns of tin phosphate synthesized without SDS surfactant calcined at different temperature for 2 hours are shown in Figure 4.3. No peaks were observed in the lower 2θ angle diffraction pattern for tin phosphate calcined from 200-500°C, as shown in Figure 4.3 (a). This indicates that no mesostructure characteristics were observed for this tin phosphate. The XRD pattern of $2\theta = 10-80^\circ$ which contained diffraction patterns of all the calcined tin phosphate powders, is shown in Figure 4.3 (b). Tin phosphate calcined at 200°C exhibited some weak peaks in the XRD pattern which suggests the phase present here is largely amorphous. A broad band exists between 20° and 23° and some tiny peaks around 28°, 31° and 44°. The occurrence of these weak peaks was indicative of the presence of $\text{Sn}(\text{HPO}_4)_2$. When the sample was further calcined at 300°C, it exhibited crystalline peaks which was matched to the standard $\text{Sn}(\text{HPO}_4)_2$ (no. 00-028-1390) from the Powder Diffraction File (PDF) database. The asterisks observed in this diffraction pattern denote the main reflections of the $\text{Sn}(\text{HPO}_4)_2$. Other diffraction peaks

observed at $2\theta = 19.5^\circ$, 22° , 29° and 34° agrees well with those reported for SnP_2O_7 by Behm and Irvine [36], Velásquez *et al.*[43] and L. Kőrösi *et al.* [58].

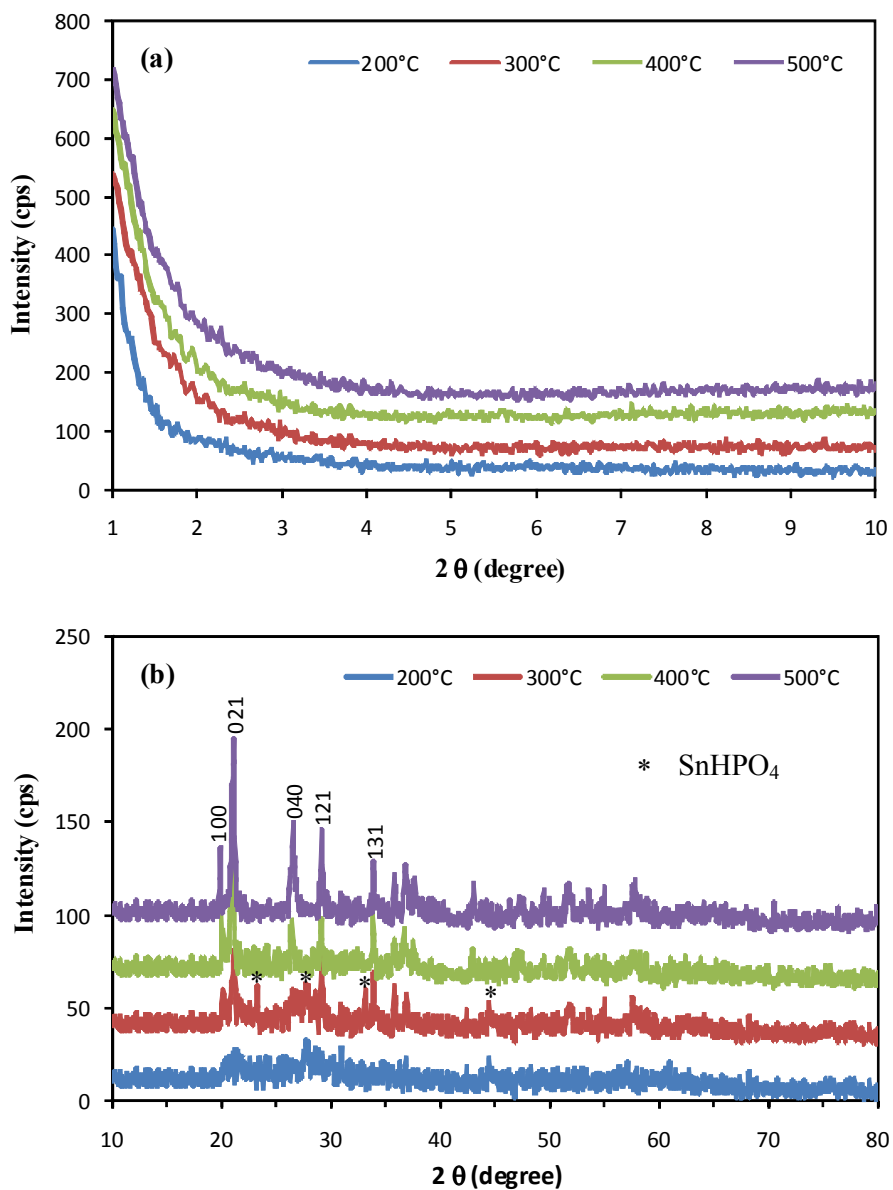


Figure 4.3: XRD pattern for tin phosphate synthesized without SDS surfactant (a) $2\theta = 1-10^\circ$ and (b) $2\theta = 10-80^\circ$.

It has been assumed earlier based on TG-DTA analysis in section 4.3 (Figure 4.1) that the mass loss of 8% within 210-390°C was attributed to the effects of dehydration of HPO_4 group. The XRD patterns of tin phosphate calcined at 300° and 400°C support that this weight loss corresponds to the structural transition of $\text{Sn}(\text{HPO}_4)_2$ to SnP_2O_7 , as expressed by Equation 4.1. Peaks previously assigned to traces of $\text{Sn}(\text{HPO}_4)_2$ for tin phosphate calcined at 300°C have disappeared in the XRD pattern for tin phosphate calcined at 400°C and appearance of new crystalline peaks were observed in XRD pattern. The position of the diffraction peaks of tin phosphate fired at 400°C is similar to that fired at 500°C. Higher peak intensities were observed for tin phosphate calcined at 500°C. The indexation of Bragg reflections in the XRD pattern for the sample at (100), (021), (040), (121) and (131) provided evidence on the presence of cubic SnP_2O_7 [36], [43], [58]. As intensity of peak increases, crystallinity of SnP_2O_7 increases as well. Calcination at higher temperature causes the tin phosphate phase to undergo further structural ordering to form cubic SnP_2O_7 crystal structure. The appearance of this SnP_2O_7 crystal structure has been anticipated based on earlier findings on the TG-DTA curve in Figure 4.1 which showed an exothermic peak indicative of phase transition from amorphous to crystalline at 328°C.

Low-angle XRD pattern ($2\theta = 1-10^\circ$) for the tin phosphate synthesized using SDS template technique as shown in Figure 4.4 (a) confirmed that the materials calcined at 200-400°C possess mesoporous characteristics. The mesostructured characteristic is evidenced by the presence of low angle reflections of (100) around $2\theta = 1.6^\circ$. The findings from the low angle XRD pattern provide initial evidence that the SDS synthesized tin phosphate exhibit mesoporous structure. Mesoporous tin phosphate calcined at 200°C showed a broad peak between 1.3° and 2° indicating that poorly ordered mesophase has begun to form at this temperature. A d-spacing value of 24 nm was determined for this sample. When this mesostructured tin phosphate was further calcined to 300°C, a narrower peak with increased intensity was observed in the XRD pattern as shown in Figure 4.4 (a). This shows the ordering of the mesostructure has taken place. Stronger intensity indicates higher ordering.

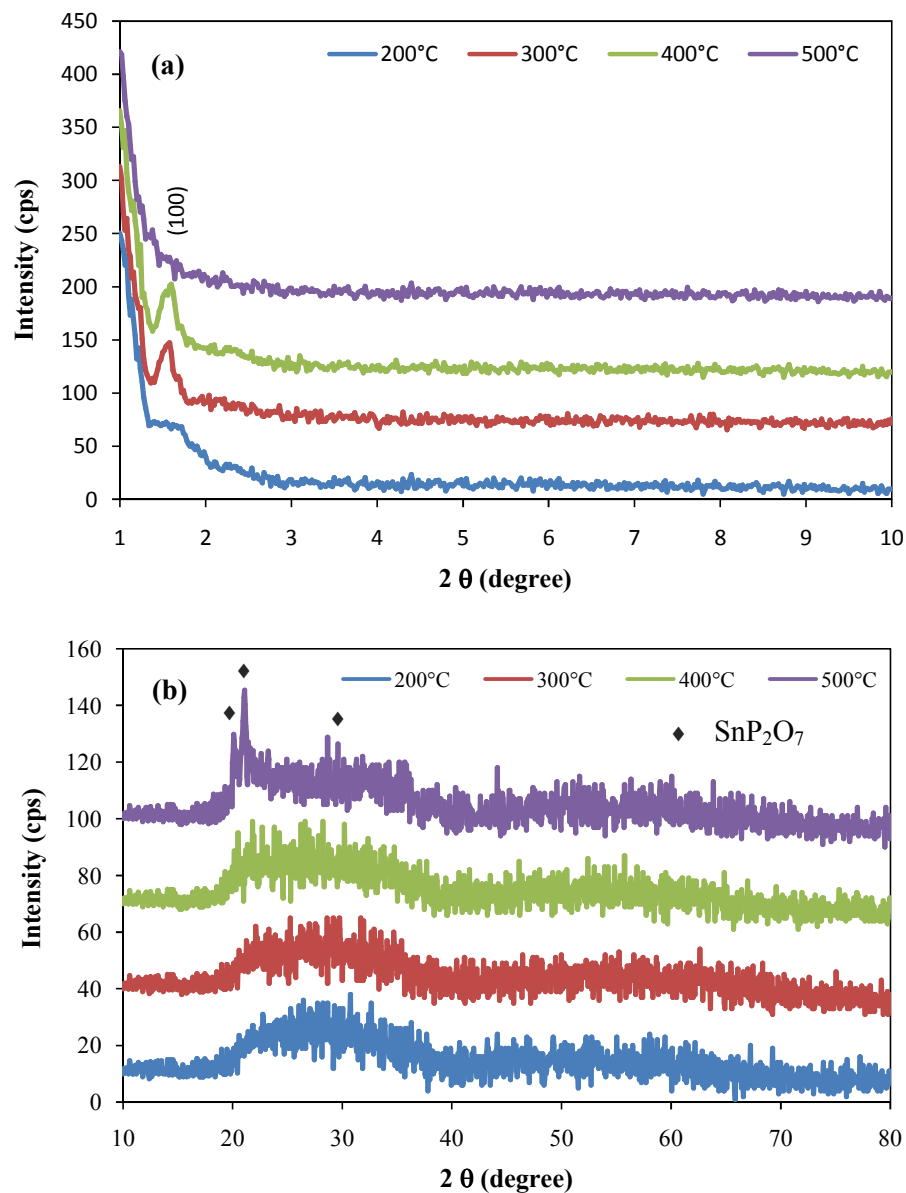


Figure 4.4: XRD pattern for tin phosphate synthesized with SDS surfactant (a) $2\theta = 1-10^\circ$ and (b) $2\theta = 10-80^\circ$.

The low angle peak characteristic for the sample heated at 300°C did not change much when heated to 400°C. This showed that the mesostructure is still preserved during the removal of SDS surfactant at this range of temperature. Both tin

phosphates calcined at 300 and 400°C showed strong reflection at (100) with d-spacing value of around 22 nm. The position of the low angle peaks and the d-spacing value for both of these calcined powders did not show obvious differences which indicate that the gradual losses of the SDS surfactant at 300 and 400°C did not cause significant mesostructural changes. However, when calcination temperature was further increased, the mesostructure phase collapsed. This is indicated by the disappearance of the low angle reflection from the XRD pattern for the SDS synthesized tin phosphate calcined at 500°C. The mesophase structure of the SDS tin phosphate was completely destroyed at this temperature.

This finding supports the assumption made earlier in the thermal analysis that decomposition of SDS surfactant occurs between 110-500°C, as depicted by the weight loss in the TG-DTA curve shown in Figure 4.2 and complete removal of the SDS surfactant takes place above 428°C. Complete removal of surfactant in non-thermally stable mesoporous materials is often associated with the collapse of mesoporous structure at high temperature [50]. The wide angle XRD pattern at $2\theta = 10-80^\circ$ for the calcined mesostructured tin phosphate is shown in Figure 4.4 (b). The diffraction pattern indicated that mesoporous tin phosphate is largely amorphous at calcination temperature of 200, 300 and 400°C and a similar broad band between $2\theta = 19^\circ$ and 38° exists for all of them. This band when indexed according to their corresponding crystalline SnP_2O_7 synthesized without the SDS surfactant as discussed earlier, could be attributed to the presence of $\text{Sn}(\text{HPO}_4)_2$ and SnP_2O_7 phases. It is observed that not only did the SDS synthesized tin phosphate calcined at 500°C, showed broad diffraction, it also displayed reflection peaks of SnP_2O_7 at $2\theta = 19.5^\circ$ and 22° . The XRD diffraction pattern for SDS synthesized tin phosphate fired at 500°C indicates that this material contains crystalline phase and presence of residual amorphous phase but is non-mesostructured. XRD patterns of amorphous and crystalline structures shows different diffraction peak signals and crystallinity properties. The diffraction peaks of amorphous sample are broader than those of the crystalline material, thus indicating that the mean crystallite size in the amorphous phase is smaller than that of the crystalline phase. Broad diffraction peaks observed in

Figure 4.4 (b) for mesoporous SnP_2O_7 fired at 200, 300 and 400°C may indicate the possibilities that the amorphous phase consists of crystallite size that are much smaller than that of the crystalline cubic SnP_2O_7 or that the calcined mesoporous tin phosphate consists of nanocrystalline domains within amorphous walls of SnP_2O_7 .

For comparison purpose, one of the SDS synthesized SnP_2O_7 batch was calcined at 400°C for 4 hours. Figure 4.5 showed the low-angle XRD pattern for mesoporous SnP_2O_7 calcined at 400°C for 2 hours and 4 hours. The SnP_2O_7 calcined at 400°C for 4 hours displayed a small shift of the low angle reflection to higher 2θ angle along with a slight increase in the width of reflection indicating that the pore structure experienced changes during surfactant removal at prolonged calcination. This slightly broader peak suggests that the degree of mesostructure ordering was reduced whereas the peak shift indicates contraction to the structure. The d-spacing of this sample is 20 nm whereas that of the SnP_2O_7 calcined at 400°C for 2 hours is 22 nm. This suggests that prolonged calcination at 400°C influences the mesostructure features.

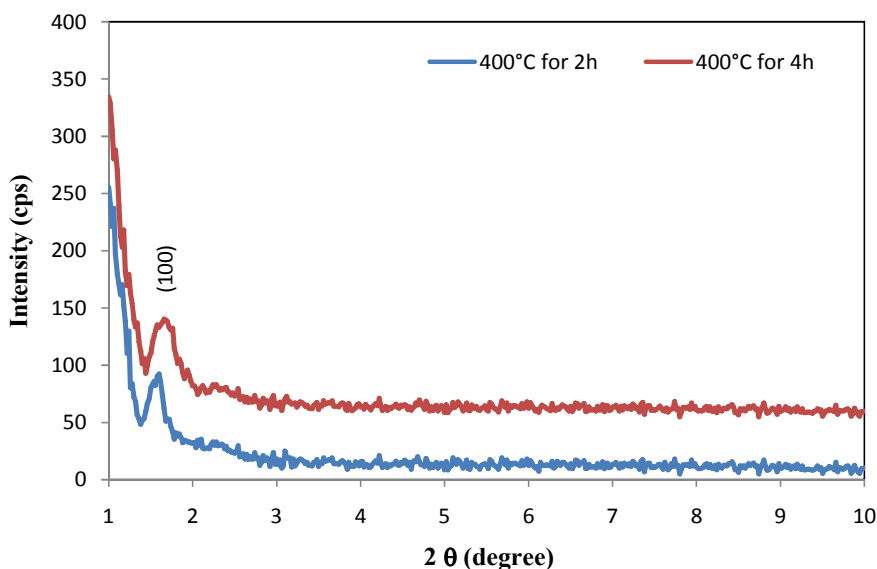


Figure 4.5: XRD pattern of mesostructured tin phosphate calcined at 400°C for 2h and 4h.

4.5 Physisorption Studies Based on Nitrogen Sorption Isotherm

The mesoporous characteristics of the SDS synthesized SnP_2O_7 was further analyzed by means of nitrogen adsorption. The nitrogen (N_2) adsorption/desorption isotherms at 77 K for the calcined SDS-synthesized SnP_2O_7 are shown in Figure 4.6. Each isotherm consists of 10 points of adsorption and 10 points of desorption. The shape of the isotherms obtained for SnP_2O_7 fired at 200, 300 and 400°C corresponds to the Langmuir Type IV isotherm which is characteristic of mesoporous materials [37], as shown in Figures 4.6 (a)-(d). As mentioned earlier in Chapter Two (section 2.5) based on IUPAC definition, mesoporous materials are porous solids with pore size pore size between 2 to 50 nm [37]. The isotherm of the SDS synthesized SnP_2O_7 calcined at 500°C (Figure 4.6 (e)) however, showed no obvious desorption characteristics and can be classified as Type II isotherm which is associated with non-porous or macroporous adsorbent materials [46]. The hysteresis profile observed for SDS synthesized SnP_2O_7 calcined at 200, 300 and 400°C are similar. A slight slope observed at low relative pressure, P/P_0 of less than 0.10 is associated with behavior of nitrogen adsorption in the inner layer of the mesopore to form a molecular monolayer [37]. After this, more nitrogen molecules are gradually adsorbed to form multilayer. This mechanism is known as mesopore filling. This gradual multilayer built up behavior does not show dramatic slope changes in P/P_0 region between 0.15 to 0.75. The third behavior depicted by the steep increase in adsorbed volume at P/P_0 ranging from 0.80 to 0.99, is caused by complete filling of nitrogen molecules in the confined mesopores [37]. The fourth adsorption behavior was observed when P/P_0 reached nitrogen saturation pressure at the peak of 0.99, where capillary condensation of nitrogen occurs in the mesopores and at this point when the adsorption process is reversed by withdrawing the nitrogen molecules from P/P_0 at 0.99 down to 0.05, a desorption isotherm is generated [37]. A hysteresis loop was observed between P/P_0 from 0.95 to 0.75. Hysteresis suggests presence of obstruction of pore channels in the synthesized mesoporous SnP_2O_7 . The shapes of hysteresis loops have often been identified with specific pore structures. Mesoporous SnP_2O_7 calcined at 200, 300 and

400°C exhibited similar hysteresis contour of a H4 type which is often associated with narrow slit-shaped pores [37].

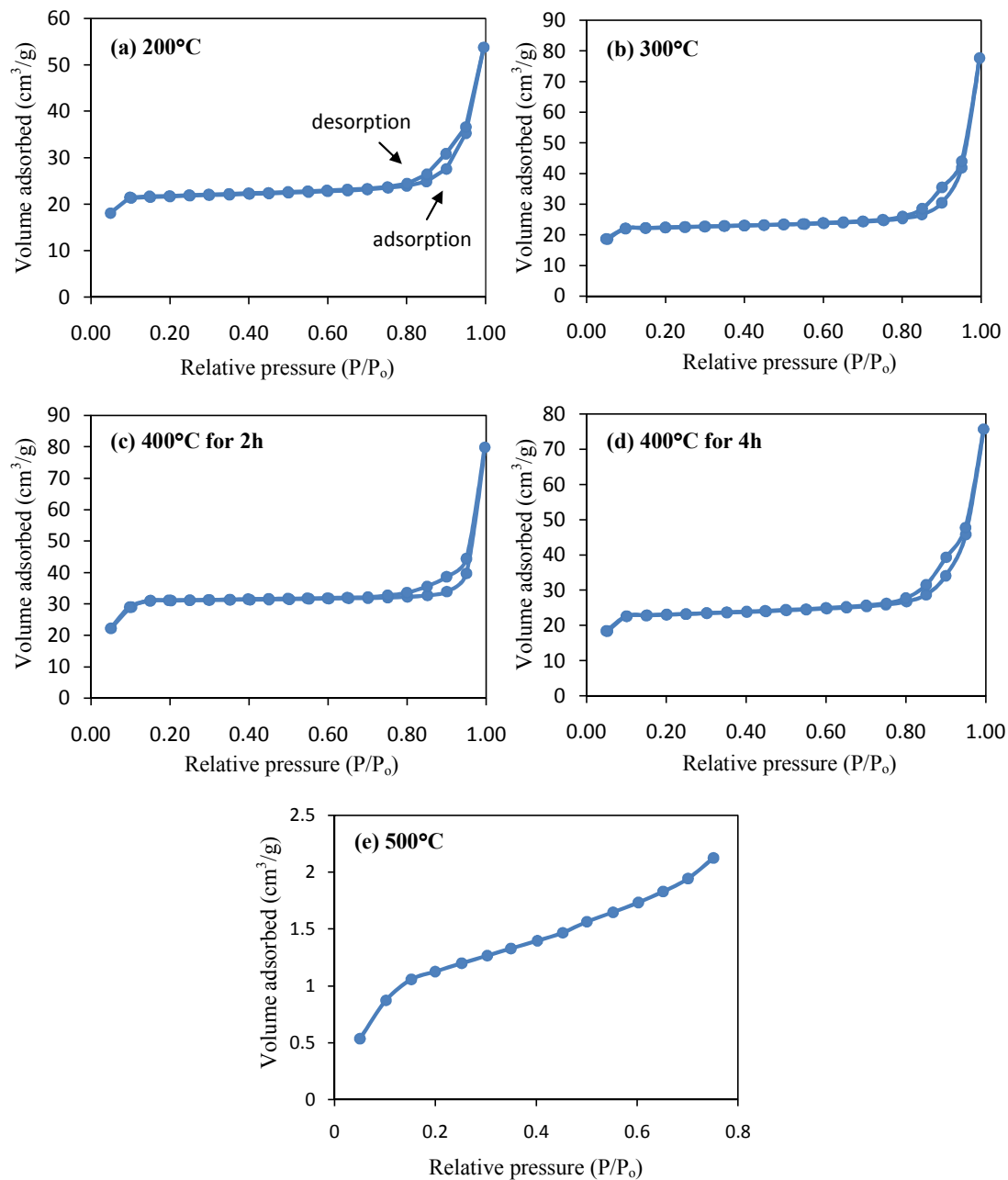


Figure 4.6: Nitrogen adsorption/desorption isotherms for SDS-synthesized SnP_2O_7 calcined for 2 hr at (a) 200°C, (b) 300°C, (c) 400°C, (d) 400°C for 4h and (e) 500°C.

The presence of the Type IV isotherm with the hysteresis loop suggests that the SDS synthesized SnP_2O_7 is mesoporous when calcined between 200 and 400°C. Based on the analysis of these sorption isotherms, it is assumed that the SDS surfactant filled the wall linings of the mesopores in the initial state. When the precursors were heat treated, gradual removal of the SDS surfactant occurs. The residual SDS remaining in the inner walls of the mesopores was believed to provide some support to the mesostructure. When the precursor was calcined to 500°C, SDS surfactant is completely removed from the mesoporous framework. This in turn has initiated the crystallization of the inorganic pore wall structure of SnP_2O_7 which led to the total collapse of the mesoporous structure. This analysis is complemented by findings from thermal analysis (section 4.3) where complete decomposition of SDS surfactant was found to occur around 428°C in the TG-DTA curve and also by findings from the XRD pattern for the SDS synthesized SnP_2O_7 calcined at 500°C (Figure 4.4, section 4.4) where no low angle reflections characteristic of mesoporous material were present and tiny peaks appeared in the wide angle spectrum indicating formation of crystalline phases. This N_2 sorption isotherm results strongly helps to conclude that the SDS synthesized SnP_2O_7 displayed mesoporous characteristics when calcined between 200 to 400°C but when fired to 500°C, the mesoporous structure collapses.

For reference purpose, N_2 adsorption studies were also conducted on the non-SDS synthesized SnP_2O_7 powders and the isotherms obtained for samples calcined at 200, 300, 400 and 500°C are shown in Figure 4.7 (a)-(d). All the isotherms revealed a Langmuir Type II isotherm which is characteristic isotherm for finely divided non-porous materials [37]. At relatively low P/P_0 pressures of less than 0.1, a monolayer of adsorbed N_2 gas molecules is formed on the surface of the material. At relatively high P/P_0 pressures, multi-layer adsorption takes place where only a very small amount of gas was adsorbed. No capillary condensation takes place at higher P/P_0 pressure which explained the absence of hysteresis loops. The only useful information that can be extracted from this sorption analysis is the surface area.

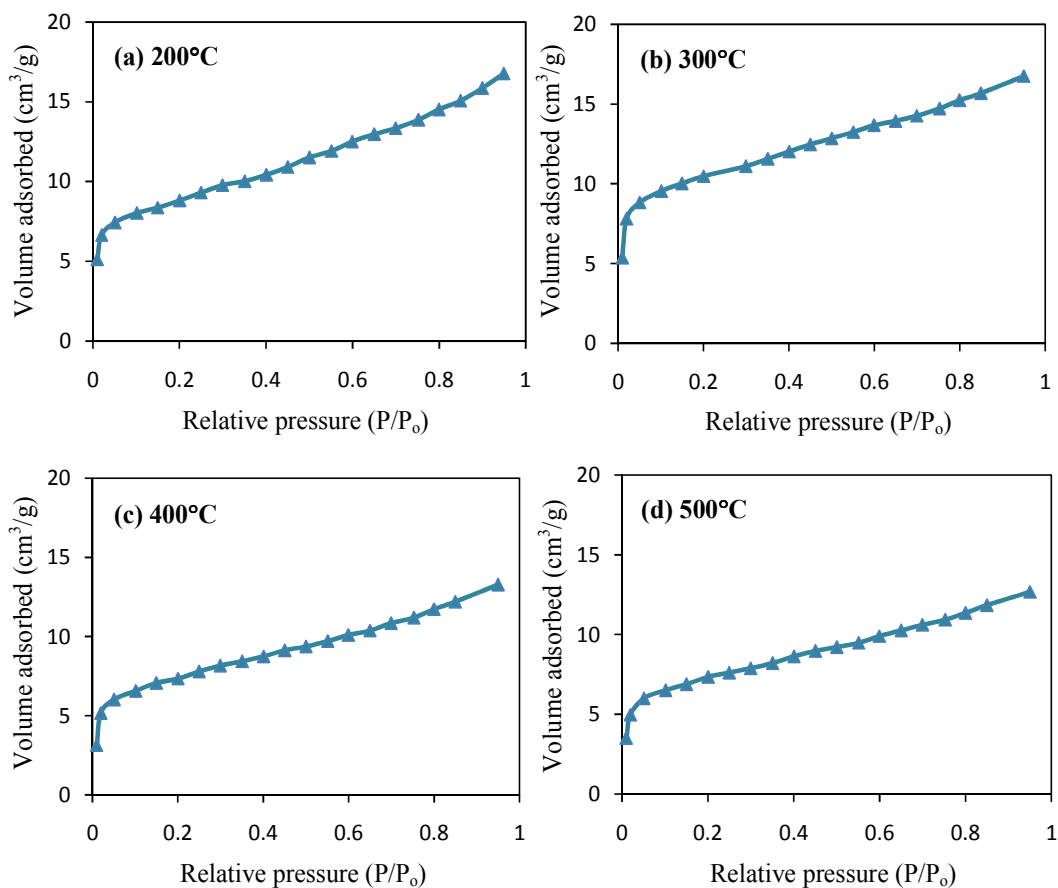


Figure 4.7: Nitrogen adsorption/desorption isotherms for non-SDS synthesized tin phosphate calcined at (a) 200°C; (b) 300°C; (c) 400°C and (d) 500°C.

Table 4.1 lists the measured Brunauer-Emmett-Teller (BET) surface area of the synthesized SnP_2O_7 powders. The BET surface area of the powders were calculated from the linear part of the BET plot ($P/P_0 = 0.05$ to 0.10). The surface area of the mesoporous SnP_2O_7 samples was estimated from the surface area of mesoporous porewall. As observed for mesoporous SnP_2O_7 samples, with increasing calcination temperature, the BET surface area began to decrease. The mesostructure SnP_2O_7 produced after calcination at 200°C and 300°C has a BET surface area of 138 m^2/g and 125 m^2/g , respectively. Mesoporous SnP_2O_7 calcined at 400°C for 2 hours has a BET surface area of 115 m^2/g whereas that calcined at the same temperature for 4 hours showed a BET surface area of 106 m^2/g . The SDS synthesized SnP_2O_7 calcined

at 500°C has a low surface area of 13 m²/g. Low surface areas of around 4-9 m²/g were also obtained for non-SDS synthesized SnP₂O₇ powders which is typical for non-porous materials. In characterization of very low specific surfaces such as the non-porous materials, it is necessary to generate a very high vacuum degree and to measure very low equilibrium pressures. The measuring gas commonly used for this case is krypton. However, there are some limitations in characterizing non-porous using the physisorption method with the present gas sorption apparatus (Quantachrome Autosorb-1C) as it is not designed to collect equilibrium pressures in a very low and restricted pressure range and it is better suited for characterization of porous solids.

Table 4.1: BET surface areas of synthesized SnP₂O₇ powders

SnP ₂ O ₇ samples	Surface Area * (m ² /g)
SDS synthesized SnP₂O₇	
200°C for 2h	138
300°C for 2h	125
400°C for 2h	115
400°C for 4h	106
500°C for 2h	13
Non-SDS synthesized SnP₂O₇	
200°C for 2h	9
300°C for 2h	7
400°C for 2h	4
500°C for 2h	4

* Surface area determined using the BET method.

Based on XRD and physisorption results, it has now been established that the SDS synthesized SnP_2O_7 powder calcined at 500°C and the non-SDS synthesized SnP_2O_7 batch are not mesostructured and non-porous. Further analysis on porous characteristics shall now be focused on SDS synthesized SnP_2O_7 powders calcined at 200, 300 and 400°C as they displayed the mesoporous characteristics.

The pore size distribution of the mesoporous SnP_2O_7 powders were determined using the Barrett-Joyner-Halenda (BJH) model and the desorption branch isotherm. Figure 4.8 shows the pore size distributions for the mesostructured SnP_2O_7 as determined using the Barrett-Joyner-Halenda (BJH) model and the desorption branch isotherm. BJH analyses showed that the mesoporous SnP_2O_7 exhibits a mean pore size of 10.6, 13.5 and 15.8 nm when calcined to 200, 300 and 400°C for 2 hours, respectively. Mesoporous SnP_2O_7 calcined at 400°C for a longer duration of 4 hours has an average pore size of 17.9 nm. All the calcined mesoporous SnP_2O_7 powders possess a relatively narrow pore size distribution. It was observed from Figure 4.8 that with increasing calcine temperature, peak pore diameters shifted to a higher value and pore size distribution becomes wider. The same effects hold true when mesoporous SnP_2O_7 was calcined for prolonged duration of 4 hours at 400°C . The SDS surfactant partially occupies the mesopores and when calcination temperature increases, the SDS surfactant slowly decomposes resulting in the smaller pore which then collapse into larger pores. The number of pore decreases as a result of sintering while at the same time the pore size increases.

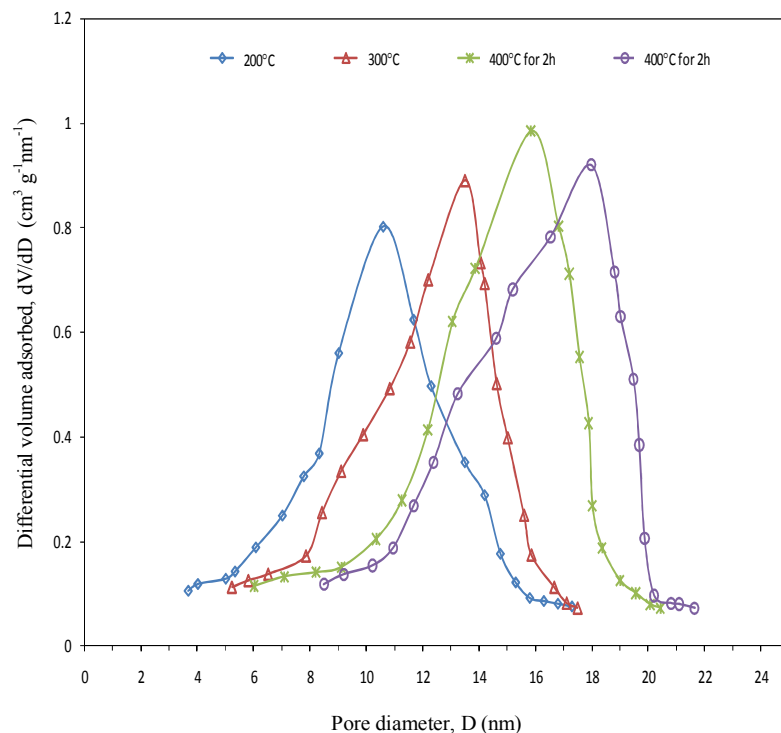


Figure 4.8: Pore size distribution of mesoporous SnP_2O_7 calcined for 2h at 200, 300 and 400°C and for 4 h at 400°C.

Pore volume values shown in Table 4.2 was taken from volume of nitrogen adsorbed at $P/P_0 = 0.99$. Pore volume increases when calcined from 200 to 400°C for 2 hours. However, a slight drop of $2.64 \text{ m}^3/\text{g}$ in adsorbed volume was recorded for the mesoporous SnP_2O_7 calcined at 400°C for 4 hours. There is no known determined relationship on how surface area and pore diameter are correlated with pore volume. The correlation strongly depends on the pore type and shape. It was mentioned earlier that the Type IV isotherm for the mesoporous SnP_2O_7 has a hysteresis loop of Type H4 which is associated with narrow slit-shaped pores. The initial increase in pore volume may be due to the increase in gas accessible areas where smaller pores collapse to form larger pores when calcined from 200 to 400°C for 2 hours. However, when calcined at 400°C for a prolonged duration, the complex slit-shaped pore network began to experience sintering of pore walls and this initiated crystallization of the SnP_2O_7 particles. This causes the pore structure to be further disordered thus

imparting some constrictions for gas to be accessible in some areas which led to a slight decrease in adsorbed volume.

Table 4.2: Structural properties of SDS synthesized SnP_2O_7 calcined at different temperature

Mesoporous SnP_2O_7	Pore diameter ^a (nm)	Pore volume ^b (m^3/g)	d_{100} ^c (nm)	Pore wall ^d (nm)
200°C for 2h	10.6	53.78	24	13.4
300°C for 2h	13.5	75.68	22	8.5
400°C for 2h	15.8	79.86	22	6.2
400°C for 4h	17.9	77.22	20	2.1

^a Pore diameter is determined using the desorption branch isotherm and BJH model.

^b Volume of N_2 adsorbed at $P/P_0 = 0.99$.

^c d_{100} is the d spacing for reflections at (100).

^d The pore wall thickness is determined by subtracting the pore diameter from the d spacing.

The low angle diffraction peak for the calcined mesoporous SnP_2O_7 provides an estimate of the average distance between framework pores based on the d-spacing values. Therefore, pore wall size can be estimated from the difference between d-spacing and pore size value. D-spacing values shown in Table 4.2 for the calcined mesoporous SnP_2O_7 was determined from reflection at (100) in the XRD pattern (Figure 4.4, section 4.3). The thicker pore wall size at lower calcination temperature may be due to the occupation of the organic SDS surfactant which lined the pore walls. For higher calcination temperature, the SDS gradually decomposes causing the SDS lining in the inner mesopore to become thinner resulting in decreased pore wall thickness. Various studies showed that the choice of surfactant is critical to the size and shape of the particles and SDS surfactant is known to produce mesoporous materials with larger mesopore sizes of ~ 10 nm [50], [59], [60].

4.6 FESEM Analysis on Tin Phosphate

Morphology of the synthesized mesoporous and non-mesoporous SnP_2O_7 powders are examined using the Field Emission Scanning Electron Microscopy (FE-SEM, LEO Gemini 1530). The microscope images of the calcined mesoporous SnP_2O_7 and non-mesoporous SnP_2O_7 magnified at 20, 000 times are shown in Figures 4.9 and 4.10, respectively.

The SDS synthesized mesoporous SnP_2O_7 powders showed spherical morphology with foam-like structure, as observed from Figure 4.9 (a)-(d). These four micrographs of the calcined mesoporous SnP_2O_7 powder showed uniform spherical particles with a narrow size distribution. The mesoporous SnP_2O_7 calcined at 200°C consists of very fine spherical particles with an average size of around 20 nm as shown in Figure 4.9 (a). These nanoparticles are loosely clustered together forming uniform pores of several nanometers between them. Observations made on the FESEM images in Figure 4.9 revealed larger aggregates of fine particles were formed when the calcination temperature was increased. The interconnected aggregates that form the mesoporous SnP_2O_7 network and the voids between them were noticeably larger when calcined to a higher temperature of 400°C , as shown in Figure 4.9 (c) and (d). When the firing temperature increases, the SDS surfactant decomposes and this in turn causes the particles to aggregate and form agglomerates thus leaving larger voids in the mesoporous SnP_2O_7 structure. The average particle size when calcined to 400°C is around 30 nm. The mesoporous SnP_2O_7 calcined at 400°C for 4 hours showed a more compact agglomerate morphology compared to that of the mesoporous SnP_2O_7 calcined at 400°C for 2 hours, as observed from Figure 4.9 (c) and (d). Prolonged calcination may induce sintering effects on the SnP_2O_7 particles causing them to grow and form larger crystallites.

The morphology of the SDS synthesized SnP_2O_7 powders calcined at 500°C as shown in Figure 4.9 (e) did not exhibit morphology similar with that observed for the mesoporous SnP_2O_7 samples. Particles observed here displayed irregular morphologies. It is harder to determine the average particle size since irregularly shaped particles tends to have a very broad particle size distribution. Obvious sintering effects on the particles were observed as the powder displayed compact arrangement of layered SnP_2O_7 clusters. The TG-DTA results obtained earlier in section 4.3 indicated that the decomposition of SDS surfactant occurred around 428°C . It is believed when the sample was fired to 500°C , the rate of particle growth was more rapid and this eventually led to the collapse of the mesostructure and formation of SnP_2O_7 aggregates which were held closely together.

Figure 4.10 shows the FESEM images of the non-SDS synthesized SnP_2O_7 powders. The FESEM image of the non mesoporous SnP_2O_7 samples calcined at 200°C displayed stacked layers of irregularly shaped particle aggregates, as shown in Figure 4.10 (a). As the non-mesoporous samples are calcined at higher temperature, they revealed a cauliflower like morphology as observed from Figure 4.10 (b)-(d). At higher calcination temperature, uniform distribution of spherical shape SnP_2O_7 aggregates form larger agglomerates that are compactly arranged. FESEM images of the non-SDS synthesized SnP_2O_7 showed uniform arrangement of particle morphology with increasing firing temperature. This complements the XRD analysis on non-mesoporous SnP_2O_7 samples in Section 4.3 that indicated the SnP_2O_7 experiences structural ordering with increasing calcination temperature to form the crystalline phase. Based on Figure 4.10 (c) and (d), the uniform spherical particles of non-mesoporous SnP_2O_7 calcined at 400 and 500°C have a narrow particle size distribution of around $0.2\text{ }\mu\text{m}$, which is very much larger than that obtained for the mesoporous SnP_2O_7 .

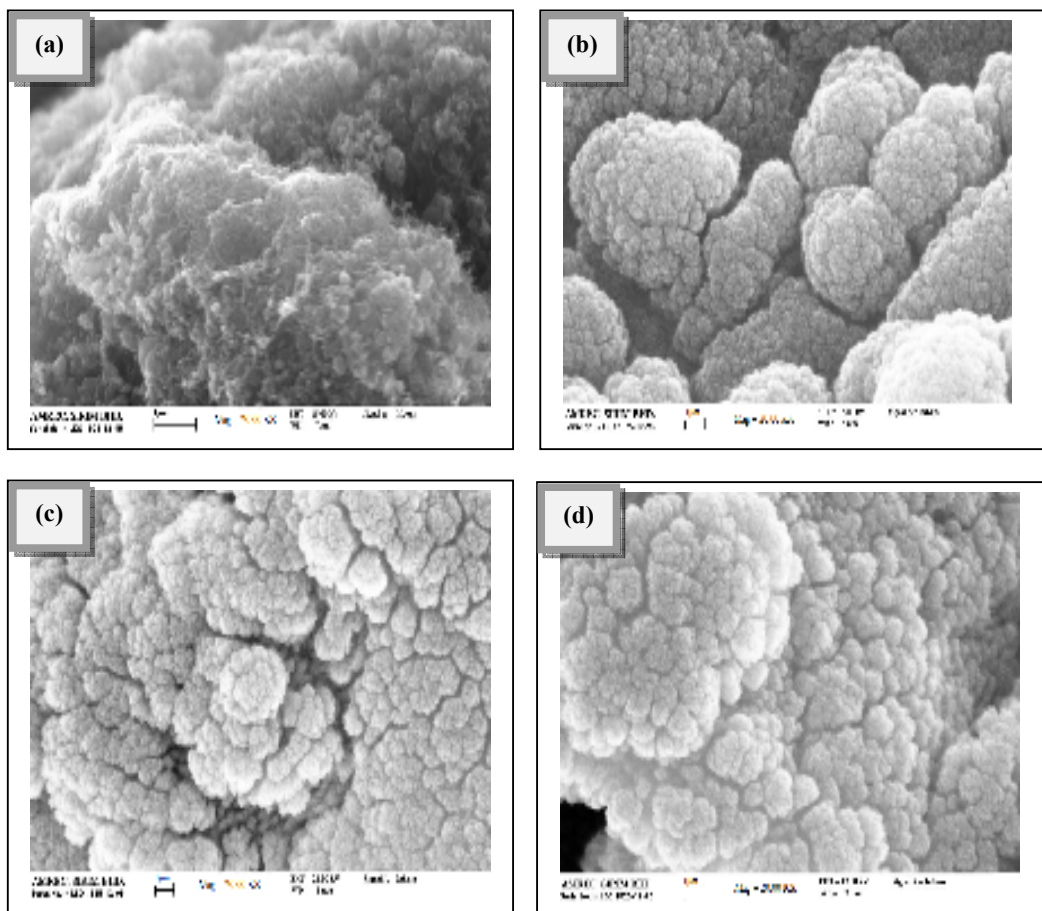


Figure 4.10: FESEM images of non-SDS synthesized SnP_2O_7 calcined at (a) 200°C for 2 hr, (b) 300°C for 2 hr, (c) 400°C for 2 hr and (d) 500°C for 2 hr.

4.7 Summary

For SnP_2O_7 powders synthesized in absence of the SDS, no mesoporous characteristics were detected by means of XRD or N_2 physisorption analysis. Crystalline phase of $\text{Sn}(\text{HPO}_4)_2$ begun to form when the powder was calcined at 300°C . When further calcined to 400°C , this compound transformed to crystalline SnP_2O_7 . The degree of crystallinity increases with increasing calcination temperature. Low surface areas of around $6\text{--}11\text{ m}^2/\text{g}$ were obtained for the non-mesoporous SnP_2O_7 samples that were calcined between 200 to 500°C . FESEM observations revealed average particle size distribution of around $0.2\text{ }\mu\text{m}$ non-mesoporous SnP_2O_7 powders calcined at 400°C .

Mesostructured, amorphous tin (IV) phosphate (SnP_2O_7) synthesized via the SDS surfactant was successfully obtained when calcined at 200 , 300 and 400°C as indicated by the presence of the low angle reflection in the XRD pattern. The mesoporous characteristics were further confirmed by N_2 physisorption analysis which showed a Type IV isotherm. Average pore size as determined for mesoporous SnP_2O_7 calcined at 200 , 300 and 400°C for 2 hours and at 400°C for 4 hours are 10.6 , 13.5 , 15.8 and 17.9 nm , respectively. Increasing calcination temperature causes gradual decomposition of SDS surfactant which led to the collapse of smaller pores to form larger pore. Average particle size of around 30 nm was observed from FESEM images for mesoporous SnP_2O_7 powders calcined at 400°C . Heating up to 500°C resulted in the destruction of the mesoporous structure. A semi-crystalline, non-mesoporous phase was obtained for the SDS synthesized SnP_2O_7 calcined at 500°C .

CHAPTER 5

ELECTROCHEMICAL PERFORMANCE OF MESOPOROUS TIN PHOSPHATE AS ANODE MATERIAL

5.1 Overview

The electrochemical performance of the mesoporous tin phosphate as anode material is the resounding theme of this research work. The performance here refers to the measured capacity (mAh/g) over a number of charge and discharge cycles. This research phase covers investigation on the electrochemical properties of the synthesized SnP_2O_7 anode using electroanalytical techniques such as the Cyclic Voltammetry (CV) and galvanostatic charge-discharge cycling performance tests. This chapter begins with the analysis on the redox behavior of the synthesized SnP_2O_7 anodes upon reaction with Li, subsequently followed by extensive investigation analysis on the voltage profile and cycling performance of the anodes. In the previous research phase, the synthesized non-mesostructured tin phosphate powders which were calcined at different temperatures have been characterized along side with the mesoporous SnP_2O_7 for reference purpose. It has been established in Chapter 4 that the SDS synthesized SnP_2O_7 calcined at 200, 300 and 400°C are mesoporous whereas that calcined at 500°C along with the non-SDS synthesized SnP_2O_7 calcined between 200 to 500°C are non-porous materials. All the mesoporous SnP_2O_7 samples produced are amorphous whereas the SDS synthesized SnP_2O_7 powder calcined at 500°C is semi-crystalline phase and the non-SDS synthesized SnP_2O_7 powders calcined between 300 to 500°C are crystalline. It would be interesting to analyze the electrochemical performance of synthesized SnP_2O_7 anodes with different structures.

In this chapter, the electrochemical behavior of all the mesoporous SnP_2O_7 anodes were compared with that of the SDS synthesized SnP_2O_7 calcined at 500°C and the non-SDS synthesized SnP_2O_7 anode calcined at 500°C . This selection was made to provide a more focus comparison analysis on the electrochemical performance of amorphous, mesoporous SnP_2O_7 anodes with the non-porous SnP_2O_7 anodes with a semi-crystalline and crystalline structure. The non-SDS synthesized SnP_2O_7 calcined at 500°C was chosen because it has the highest degree of crystallinity in its batch. A control half-cell consisting of a commercial graphite anode was constructed and tested in the same manner as the mesoporous and non-mesoporous SnP_2O_7 samples for performance comparison purpose as well. In the later part of this study, the best performing mesoporous SnP_2O_7 anode was singled out for performance evaluation within different voltage limits and for prolonged cycling tests. For ease of sample reference in this chapter, the synthesized SnP_2O_7 investigated in this study shall be denoted as follows;

Mesoporous SnP_2O_7 calcined at 200°C for 2 hr	→ MP200
Mesoporous SnP_2O_7 calcined at 300°C for 2 hr	→ MP300
Mesoporous SnP_2O_7 calcined at 400°C for 2 hr	→ MP400
Mesoporous SnP_2O_7 calcined at 400°C for 4 hr	→ MP4004
SDS synthesized, semi-crystalline SnP_2O_7 calcined at 500°C for 2 hr	→ MP500
Non-SDS synthesized, crystalline SnP_2O_7 calcined at 500°C for 2 hr	→ TP500

Some ex-situ analysis on the cycled anode samples were carried out using Fourier Transform Infrared and Field-Emission Scanning Electron Microscope methods to further complement electrochemical analysis on the SnP_2O_7 anodes.

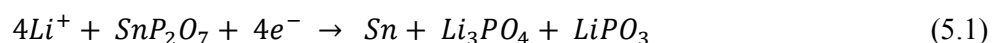
5.2 Cyclic Voltammetry Analysis on Mesoporous and Non-Mesoporous Tin Phosphate Electrodes

The cyclic voltammetry (CV) technique was used to elucidate electrochemical behavior of the synthesized amorphous, mesoporous tin phosphate (SnP_2O_7) electrodes during reduction and oxidation. The preparation of the mesoporous SnP_2O_7 electrode for CV tests has been described earlier in Chapter 3 (section 3.5). The fabricated electrode was assembled in a three-electrode custom designed electrochemical cell casing with Li foils as both counter and reference electrode and 1 M LiPF_6 in EC:DMC (1:1) as the electrolyte. Li metal is believed to be minimally polarized due to low current densities, thus giving a reliable reference potential. All potentials will be referred to the Li/Li^+ electrode throughout this thesis. The assembly configuration of the CV cell is schematically represented in Figure 3.4 (Chapter 3, section 3.5). Once assembled the test cells were immediately subjected to CV tests [49]. The cells were scanned within a potential of 0 to 2.0 V with a slow scan rate of 0.100 mV/s for three cycles. The first scan always begins cathodically from the rest potential or open circuit voltage (OCV) which is around 3.0 V for the tin phosphate anodes investigated here. During this potential scan, changes in current resulting from redox (reduction and oxidation) reactions in the cell were recorded as shown in the cyclic voltammograms in Figures 5.1 and 5.2.

Cyclic voltammograms of mesoporous SnP_2O_7 calcined from 200 to 400°C are shown in Figure 5.1. The voltammetric responses as observed from the figure for all four calcined samples looked fairly similar. The potential sites of redox peaks for the calcined mesoporous SnP_2O_7 anodes are only different by a magnitude of ± 0.02 V when compared to each other. It can also be observed from all the voltammograms shown in Figure 5.1 that the appearance of the first sweep from OCV (~ 3.0) to 0.0V is very different from subsequent cycles. During the first sweep, essentially all the irreversible reactions occur. All four cyclic voltammograms of the calcined mesoporous SnP_2O_7 electrodes exhibited four cathodic peaks in the initial first cycle scan. Regardless of which mesoporous SnP_2O_7 sample is being referred to, the first three peaks which were detected around 1.67, 1.10 and 0.69 V only appears once

during the first cathodic scan. The underlying reactions are irreversible because no similar features were observed from the second scan onward. Reaction occurring around 1.65 to 1.67 V may be attributed to the electrolyte decomposition on the active anode surface to form a passivating film known as the solid electrolyte interface (SEI) [61]. Initial contact of the electrolyte and Li metal causes the organic solvent of the electrolyte to be reduced resulting in the formation of the SEI film on the surface of SnP_2O_7 electrode [61]. This passive film is only a few nanometers thick and its composition consists mainly of lithium alkylcarbonates [61]. This passive film is fragile and easily oxidized when exposed to air. It is difficult to conduct ex-situ XRD analysis to determine the stability of mesoporous SnP_2O_7 anode upon interaction with the electrolyte as these SEI films are largely amorphous. The formation of this SEI film is irreversible. The following reaction proceeds whereby Li^+ pass through the passive film and react with the SnP_2O_7 .

Courtney and Dahn had reported the electrochemical properties of two different tin oxide systems (SnO and Sn_2BPO_6) [25], [26]. In both systems, the irreversible reactions during the first discharge process involve the reduction of the starting tin oxide based materials to form tin and lithium oxide (Li_2O) phase. For SnO , the decomposition begins at 1.2 V and involves 2 mol of lithium per mole of SnO [25], [62]. For Sn_2BPO_6 , the decomposition begins at 1.5 V and consumes 4 mole of lithium per mole of Sn_2BPO_6 [26], [61]. The reduction products would be microscopic tin particles dispersed in an inactive matrix consisting of lithium phosphate phases [7], [26], [36]. The irreversible reaction of SnP_2O_7 with Li in the first cycle can be expressed in equation (5.1) as proposed by Xiao *et al.* [7];



The reduction reaction expressed in Equation 5.1 should be indicated by the presence of an irreversible peak in the cyclic voltammogram. In line with this, the presence of next irreversible cathodic peak after the irreversible formation of the passive film around 1.65 - 1.67 V can be associated with the reduction of SnP_2O_7 .

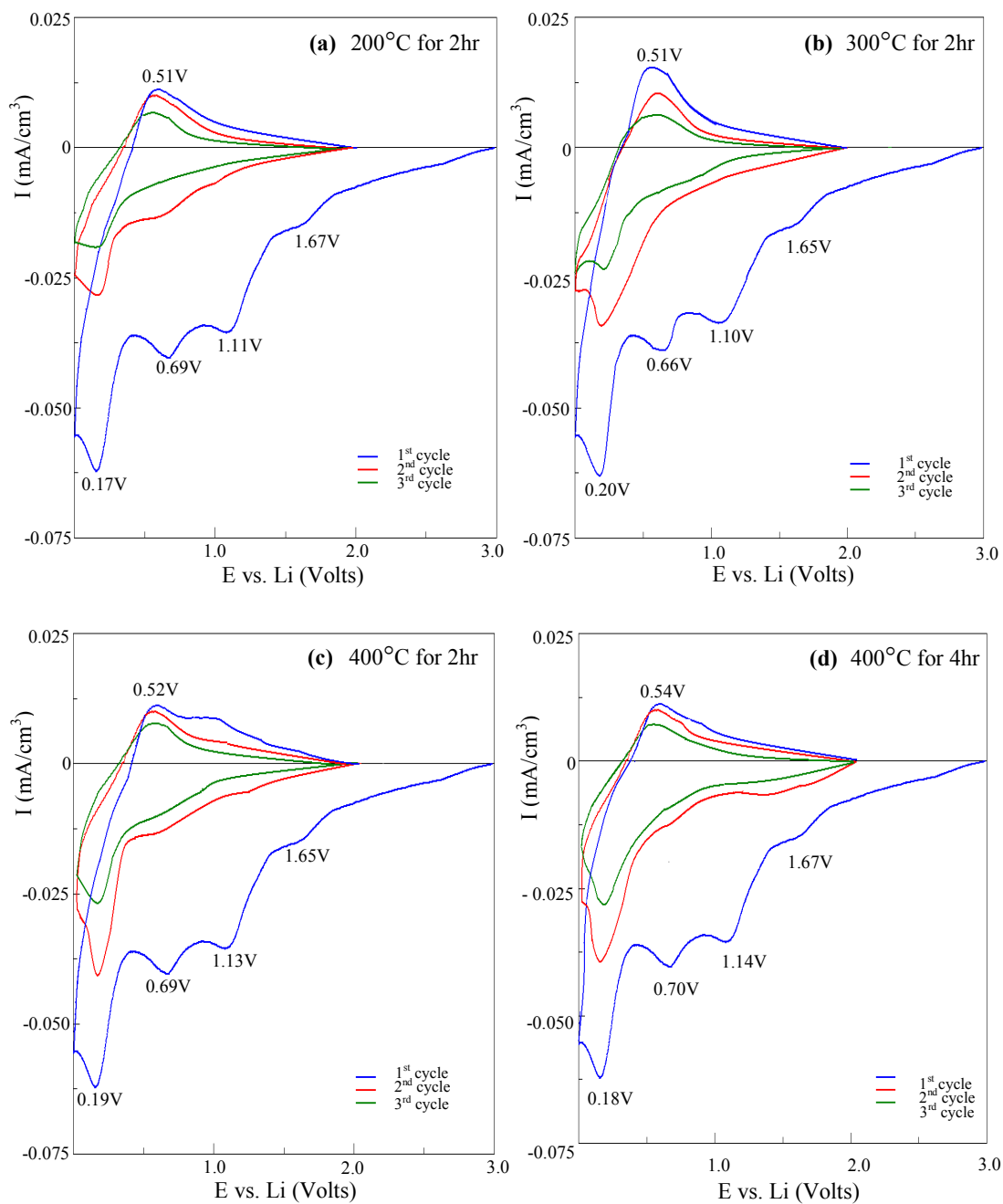
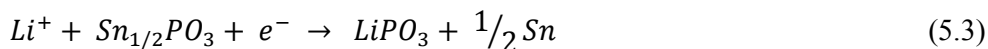
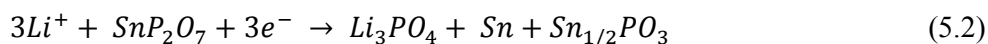


Figure 5.1: Cyclic voltammograms of mesoporous SnP_2O_7 calcined at; (a) 200°C for 2 hr (MP200), (b) 300°C for 2 hr (MP300), (c) 400°C for 2 hr (MP400) and (d) 400°C for 4 hr (MP4004).

However, in the case of the mesoporous SnP_2O_7 electrode, there are two irreversible cathodic peaks observed around 1.10 and 0.69 V. This could mean that there are two energetically different environments for the reduction of SnP_2O_7 to occur in the mesoporous structure. It is hypothesized that during the initial reduction reaction of the amorphous, mesoporous SnP_2O_7 , some partially reduced tin phosphate may first be formed at 1.10 V. This was the case reported by Xiao *et al.* [7] in their study on amorphous tin phosphate anode. The unstable tin phosphate ($\text{Sn}_{0.5}\text{PO}_3$) phase when further reacted with the remaining Li was reduced to tin (Sn) particles and lithium phosphate phase at a different potential site. Therefore, the reduction reaction in the first cycle for mesoporous SnP_2O_7 was assumed to proceed in the following stepwise order [7];



The electrochemical reactions (Equations (5.2) and (5.3)) that gave rise to these two peaks result in large irreversible losses as there is a wide gap observed between this curve in the first cycle and the following curve in the second cycle. The fourth cathodic peak located around 0.18 V was subsequently followed by an oxidation peak around 0.52 V on the reverse anodic scan. This pair of redox peaks appeared in all three cycles in the voltammograms which indicate reversible reaction. This reaction is associated with the reversible Li insertion and extraction reaction. This pair of reversible redox peaks was found to decrease in size with increasing cycle number indicating gradual loss in recyclability.

Based on other studies carried out on tin phosphate based anodes [7], [26], [36], [42], the reversible reaction is said to be identical with that of the tin oxide based anodes as discussed earlier in Chapter Two (section 2.4.3). The microscopic Sn particles dispersed in the Li_3PO_4 and LiPO_3 matrix behave as hosts for further Li^+ insertion possibly through the formation of various Li-Sn alloy composition. The de-alloying process is expected to occur during the charging process to release Li^+ and to restore the metallic Sn.

This reversible reaction is represented as below;



Based on structural and morphological analysis discussed in Chapter 4, different calcination temperature and duration produced mesoporous SnP_2O_7 with different pore size distribution and morphology. However, the cyclic voltammetric response observed for all the mesoporous SnP_2O_7 samples showed that neither the calcination temperature nor duration has a pronounced influence on the electrochemical behaviour. This is because all the amorphous, mesoporous SnP_2O_7 anodes have the same energetic sites for reaction with Li, therefore they all displayed similar redox reactions despite the difference in mesostructure characteristics,.

For references purpose, CV measurements were also carried out on different non-mesostructured SnP_2O_7 electrodes such as the SDS synthesized semi-crystalline SnP_2O_7 calcined at 500°C (MP500) and the non-SDS synthesized crystalline SnP_2O_7 calcined at 500°C (TP500). It is essential to determine if the crystallographic feature has any influence on the redox behaviour of SnP_2O_7 anodes. TP500 was chosen because it has the highest degree of crystallinity. The cyclic voltammograms of these two samples are shown in Figure 5.2.

For MP500 anode, the presence of the three irreversible peaks during the initial scan was associated with the same reactions occurring in mesoporous SnP_2O_7 electrodes during the CV measurements. The first peak at 2.02 V was assigned to the initial decomposition of electrolyte species to form the passive layer on the electrode surface. The irreversible peaks at 1.43 and 0.80 V were referred to the initial reduction of SnP_2O_7 to form Sn particles and the irreversible lithium phosphate phases (Li_3PO_4 and $LiPO_3$), as expressed by Equations (5.2) and (5.3). The only difference detected in this cyclic voltammogram when compared to the ones for mesoporous SnP_2O_7 is the potential at where these reactions take place. This difference is believed to be influenced by their crystallographic features. The presence of some crystalline phase may cause the irreversible reaction to take place at different potential sites. The next cathodic peak was found at around 0.20 V and upon the reverse anodic scan, a

small peak was detected around 0.52 V. These peaks are visible in the second and third cycles indicating the reactions occurring here are reversible. This pair of reversible redox peaks was found to be similar with that observed for mesoporous SnP_2O_7 electrodes which are associated with the reversible Li^+ insertion and extraction reactions as represented by Equation (5.4).

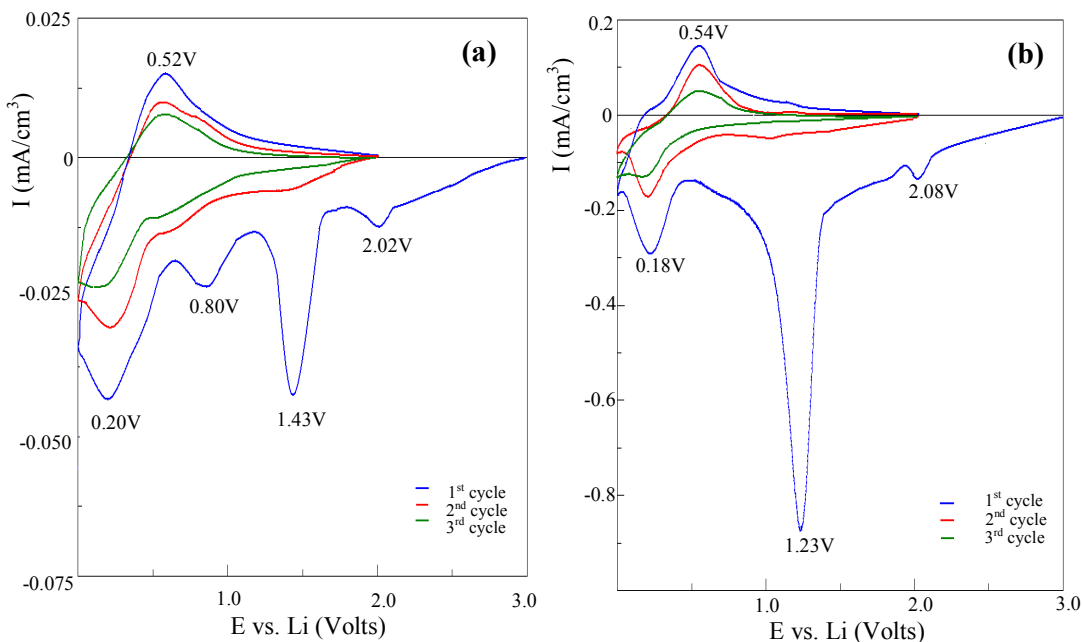


Figure 5.2: Cyclic voltammograms of (a) SDS synthesized SnP_2O_7 calcined at 500°C for 2 hr (MP500) and (b) non-SDS synthesized SnP_2O_7 calcined at 500°C (TP500).

The cyclic voltammogram for TP500 is shown in Figure 5.2 (b). This voltammogram has a very different profile when compared to that of MP500 and the rest of the mesoporous SnP_2O_7 electrodes. The small peak at 2.08 V is ascribed to the initial passive film formation. Further on, a large irreversible cathodic peak at 1.23 V was observed. This cathodic peak is referred to the initial irreversible reduction of SnP_2O_7 to form Sn particles and the irreversible lithium phosphate phases (Li_3PO_4 and LiPO_3). This single peak conforms to the reaction expressed in Equation (5.1). The pair of reversible redox peaks located at 0.18 V and 0.54 V for TP500 anode was found to be similar with that obtained for MP500 and mesoporous SnP_2O_7 electrodes. These peaks were attributed accordingly to the reversible reaction of Li insertion and

extraction reaction. This cyclic voltammogram profile for TP500 was found to be similar with that obtained by Behm and Irvine [36] in their work on crystalline SnP_2O_7 synthesized via a solid state reaction.

5.3 Voltage Profile on Initial Charge and Discharge Cycle of Mesoporous and Non-Mesoporous Tin Phosphate Anodes

All the mesoporous SnP_2O_7 anodes (MP200, MP300, MP400 and MP4004) and non-mesoporous anodes SnP_2O_7 (MP500 and TP500) fabricated in this study, were assembled in a custom designed two-electrode electrochemical cell (Figure 3.4) with 1 M LiPF_6 in EC:DMC (1:1) as the electrolyte and Li foil as the counter electrode. The assembled cells were allowed to rest overnight before galvanostatic tests. This is done in order to obtain a more thorough wetting of particle's surface areas by allowing the anode to soak in the liquid electrolyte for some time in the sealed electrochemical test cell. In this initial study on the charge discharge profile, the assembled cell was discharged (Li^+ insertion) and charged (Li^+ extraction) at a constant current of 0.5 mA between 0.0 to 2.0 V. The voltage cutoff was specified at 0.0 V and 2.0 V in order to obtain a deep discharge and charge state profile to study the Li^+ storage and extraction capacity of the synthesized SnP_2O_7 anode. This current value of 0.5 mA was selected depending on the theoretical capacity and the active weight of the tin phosphate anode under investigation, as cited from literatures [7], [25], [26], [42]. The capacity expressed here is the specific capacity per gram of the active SnP_2O_7 anode. Differential capacity plot was constructed based on the first charge and discharge data of the corresponding SnP_2O_7 anode under investigation using the IVMAN DA software. Although similar electro-analytical information can be obtained from differential capacity plots and the CV technique, the derivation of data are based on different methodology. In the CV technique, a voltage is applied and the electrode's electrochemical reaction is detected by measuring the current changes during the potential scan and it is common practice for the CV cells to be tested immediately after assembly to detect immediate redox reactions [49]. The galvanostatic charge-discharge test on the other hand was conducted by applying

current to a cell within a voltage range to evaluate capacity of the cell. The differential capacity plot is derived from the galvanostatic cycling data to gauge subtle changes arising from electrochemical reactions, not discernible in the voltage profile during charging and discharging. These analyses from differential capacity plots for MP200, MP300, MP400, MP4004, MP500 and TP500 could complement the electroanalysis obtained from the corresponding cyclic voltammograms from section 5.2. The differential capacity plots are placed next to the first discharging and charging curves of the fabricated mesoporous and non-mesoporous SnP_2O_7 anodes as shown in Figures 5.3 and 5.4, respectively.

The mesoporous SnP_2O_7 anodes; MP200, MP300, MP400 and MP4004 exhibited similar charge-discharge curve profile as observed from Figures 5.3 (a)-(d). The initial discharge profile for all the mesoporous SnP_2O_7 anodes displayed a plateau around 1.1 V before the voltage drops down to 0.0 V. This plateau is related to the Li^+ insertion into the anode and the reduction of Sn^{4+} to Sn as reported by several authors [36], [62]. Subsequent charging up to 2.0 V gives the charge capacity that reflects on how much Li^+ could be extracted out. The charge curve has a shorter profile compared to the discharge curve and this indicates during the charging process, not all the inserted Li^+ were extracted out resulting in some irreversible capacity loss.

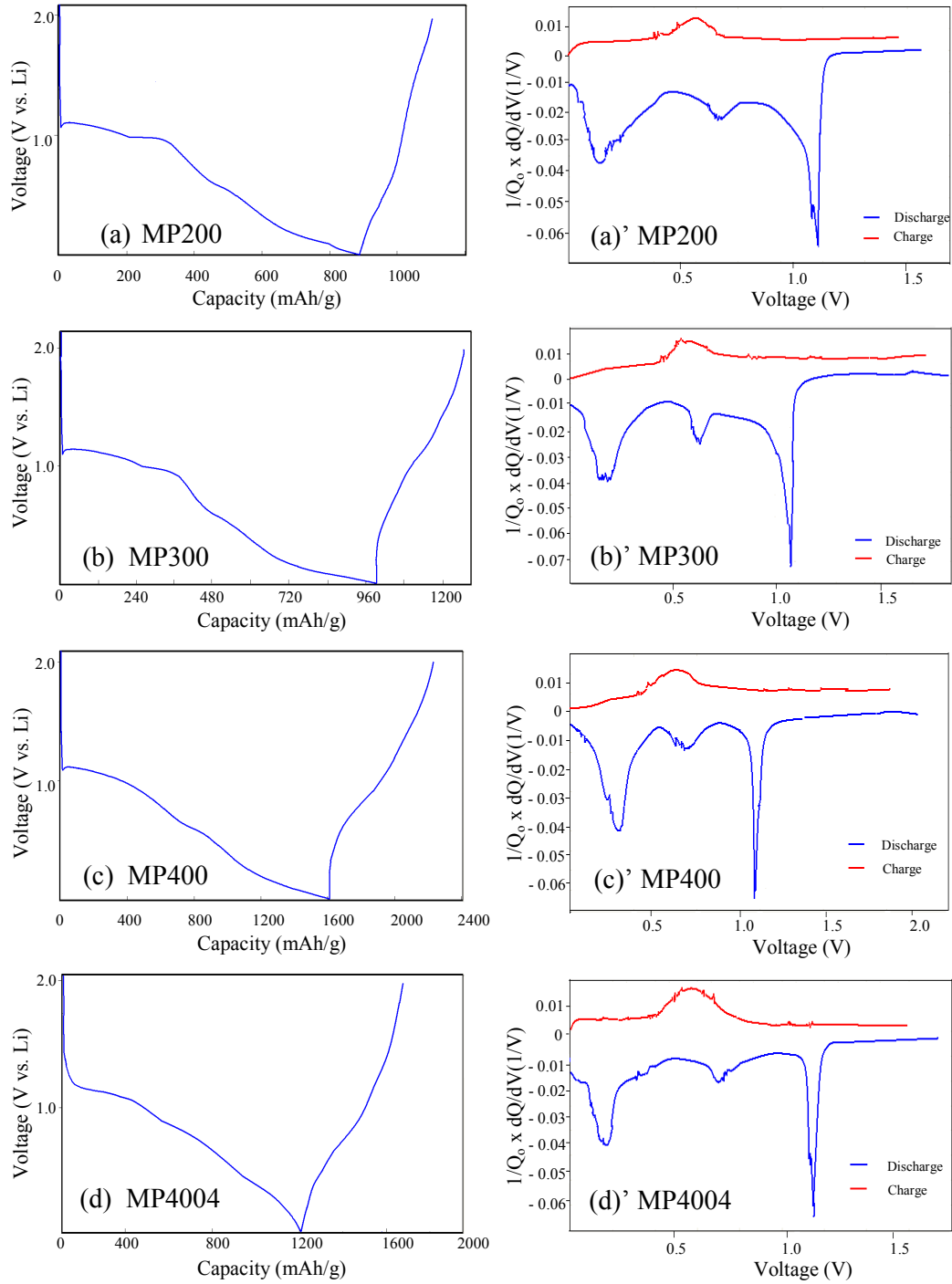


Figure 5.3: First cycle data on charge/discharge curve and differential capacity plot for mesoporous SnP_2O_7 anodes, MP200, MP300, MP400 and MP4004.

The differential capacity plot provides a mean to analyze the electrochemical reactions that cause the losses that occurred during the discharging and charging process within a voltage limit. On an average estimation based on the differential capacity plots for MP200, MP300, MP400 and MP4004, there are two cathodic peaks detected around 1.1 V and 0.7 V as shown in Figures 5.3 (a)-(d)'. These peaks match those found in the first cycle scan in the cyclic voltammogram shown in Figures 5.1 (a)-(d), which indicate the reduction of SnP_2O_7 . The first reduction reaction resulted in formation of lithium phosphate (Li_3PO_4), unstable tin phosphate ($\text{Sn}_{0.5}\text{PO}_3$) phase and Sn particles [7]. This unstable $\text{Sn}_{0.5}\text{PO}_3$ when further reacted with Li was believed to be reduced at a different potential to form LiPO_3 and Sn particles [7]. These irreversible reactions were expressed in Equations (5.2) and (5.3). There is no distinctive peak present in all the differential capacity plots in Figures 5.3 (a)-(d) that indicates the electrolyte decomposition reaction to form passive SEI films on the active anode surface as was observed in the corresponding cyclic voltammograms in Figures 5.1 (a)-(d). This is because this test cell has been left to rest overnight prior to charge-discharge test and the SEI film formation had already taken place during this rest period. This explains why the electrolyte decomposition reaction was not detected in the differential capacity plot. It was assumed based on the cyclic voltammogram analyses that the alloying and dealloying reactions of Li_xSn are the reversible reactions that occur during the discharging and charging process. Correspondingly, the peaks located around 0.17 V and 0.54 V in Figures 5.3 (a)-(d) represents the reversible Li^+ insertion and extraction reactions, respectively. The potential sites of these peaks in the differential capacity plots agree well with those obtained in the cyclic voltammograms in Figures 5.1 (a)-(d). Alloying and de-alloying reactions of Li-Sn which covers a number of alloy phases with different compositions are expected to take place within this potential range.

For non-mesoporous anode, MP500, there are three cathodic peaks observed at 1.2, 0.80 and 0.20 V in the differential capacity plot shown in Figure 5.4 (a)'. The reactions occurring at 1.2 and 0.8 V were attributed the irreversible reactions of SnP_2O_7 reduction as expressed in Equations (5.2) and (5.3), which is similar with the

reactions occurring for mesoporous SnP_2O_7 anodes. This differential capacity plot corresponds with the findings obtained from the MP500 cyclic voltammogram in Figure 5.2 (a). The reversible Li^+ insertion and extraction reaction peaks which were located at 0.20V and 0.52V, respectively in this plot are also similar with that obtained from the corresponding cyclic voltammogram.

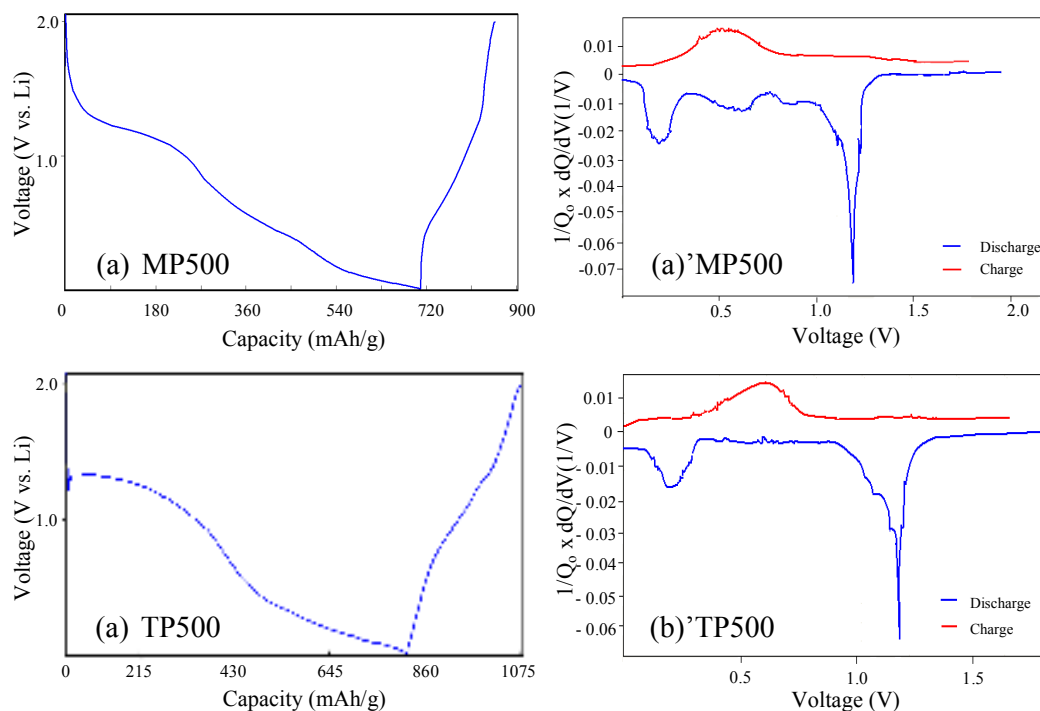


Figure 5.4: First cycle data on charge/discharge curve and differential capacity plot for non-mesoporous SnP_2O_7 anodes, MP500 and TP500.

For non-mesoporous TP500 anode, there is only one cathodic peak observed at 1.22V in the differential capacity plot shown in Figure 5.4 (b)'. This is similar with that obtained from the corresponding cyclic voltammogram at 1.23 V as shown earlier in Figure 5.2 (b). This peak is attributed to the reduction of SnP_2O_7 to form lithium phosphate phases (Li_3PO_4 and LiPO_3) and Sn particles, as expressed earlier in Equation (5.1). The reversible Li-Sn alloying and de-alloying reaction of TP500 anode are represented by the pair of peak at 0.18 V and 0.58 V, which was also similar with that found in the corresponding cyclic voltammogram.

The voltage profiles of the first cycle and the differential capacity plots observed for all the mesoporous SnP_2O_7 samples basically showed similar electrochemical behavior profile, as displayed in Figure 5.3. The main difference lies in the measured capacity value. Based on Figures 5.3 (a)-(d), when the anode was discharge to 0.0 V, the discharge capacity value was obtained and accordingly when the anode was charged to 2.0 V, the charge capacity was obtained. Table 5.1 summarizes the first cycle charge discharge capacity data of the SnP_2O_7 anodes cycled between 0.0-2.0V. Among the six different SnP_2O_7 anodes tested, MP400 delivers the highest initial discharge capacity (1650 mAh/g) whereas the lowest discharge capacity was obtained from MP500 (705 mAh/g).

Table 5.1: Initial charge discharge capacity of SnP_2O_7 anodes cycled between 0.0-2.0V

Anode	1 st cycle discharge capacity (mAh/g)	x , (Li_xSn)	1 st cycle charge capacity (mAh/g)	Irreversible losses (%)
MP200	897	4	182	79.7
MP300	1010	4.5	350	65.3
MP400	1650	7.3	590	64.2
MP4004	1240	5.5	508	59
MP500	705	3.1	150	78.7
TP500	821	3.6	275	66.5

Idota *et al.* considered the reaction between lithium and the tin composite oxide anode as a reversible intercalation reaction and that it does not involved the formation of tin [24]. Their explanation could not easily resolve the large amount of lithium that is taken up by tin (4.4 moles of Li per mole of Sn) as most intercalation systems typically involve $\frac{1}{2}$ to 1 mole of Li per mole of Sn. Courtney and Dahn have preferred to consider the presence of Li_xSn alloys and their inter-conversions to be responsible for charge storage and withdrawal [25], [26]. They proposed that the reversible Li-Sn alloying and de-alloying reaction, as represented by Equation (5.4) gives the anode material its reversible charge storage capacity [25], [26]. In theory, 4.4 Li atoms can

be electrochemically inserted reversibly per atom of Sn to form the $\text{Li}_{4.4}\text{Sn}$ alloy, which would give the tin anode a maximum theoretical capacity of 993 mAh/g [25], [26]. The calculation of the theoretical capacity has been explained earlier in Chapter Two (section 2.4.1).

For this investigation, it is assumed that the charge consumed during the discharging process (Li insertion process) is for the reduction of Sn^{4+} to Sn and Li^+ to Li to form Li_xSn alloy. The equivalent moles of Li^+ , x to form the alloy, Li_xSn for all the SnP_2O_7 anodes tested as shown in Table 5.1 was calculated using the discharge capacity obtained in the first cycle based on the alloying theory outlined by Courtney and Dahn [25], [26]. The other mesoporous SnP_2O_7 samples such as MP300, MP400 and MP4004 performed better in terms of accommodating higher amount of Li^+ as reflected by the higher initial discharge capacities and x number of Li^+ moles to form the Li_xSn alloy as observed from Table 5.1.

5.4 Ex-Situ Analysis on Mesoporous Tin Phosphate Anode Using Infrared Techniques

The rechargeability of tin phosphate is based on the reversibility in electrochemical reactions involving structurally related phases of Li-Sn alloy. The alloy phase is believed to be dispersed in a phosphate matrix consisting primarily of the decomposition products formed during the first Li insertion reaction. It was proposed by Xiao *et al.* that tin phosphate decomposes to lithium phosphate phases (Li_3PO_4 and LiPO_3) and Sn particles upon reaction with Li, as expressed in Equation (5.1) [7]. It is essential to investigate the presence of irreversible phosphate matrix that was formed during the reduction of SnP_2O_7 upon reaction with Li in order to determine its influence on the reversibility of the synthesized SnP_2O_7 anodes as analyzed based on results from cyclic voltammograms, initial charge-discharge curves and differential capacity plots which was covered in sections 5.2 and 5.3, above. In order to explain the processes of Li insertion into the SnP_2O_7 , changes in the structure of the anode during the discharge process is investigated by means of infrared techniques. Ex-situ analysis was not carried out with XRD technique mainly because the mesoporous anode structure is largely amorphous and based on literatures [7], [25], [26], [36], the lithium phosphate phases are also amorphous.

Infrared spectroscopy is often used to characterize solid phosphates based on vibrations of the P-O bonds. In this study, ex-situ analysis on the discharged and charged mesoporous SnP_2O_7 was carried out by means of Fourier Transformed Infrared (FTIR) technique. Based on analysis on cyclic voltammograms and differential capacity plots for the SnP_2O_7 anodes, it was found that the peak and plateau observed around 1.1 - 1.2 V is related to the Li^+ insertion into the anode causing reduction of the SnP_2O_7 to form lithium phosphate phases and Sn particles. Therefore, it is interesting to analyze the structure of the SnP_2O_7 anode at the state of discharge around 1.1 V. The mesoporous SnP_2O_7 anode, MP400 was chosen for this analysis as it delivers the best initial charge-discharge performance. The term lithiation shall be used in this context to refer to the state where the anode structure is inserted with Li and accordingly the term delithiation refers to the state of the anode

when Li^+ are extracted out. FTIR analysis was carried out on pristine MP400 anode, MP400 anode discharged to 1.1 V, MP400 anode discharged to 0.0 V and MP400 anode charge to 2.0 V. Attempts to extract information from FTIR spectra of freshly discharged and charged anode samples are tough due to reactions of the electrolyte with the atmosphere and to the presence of solvent used to support the electrolyte in the cells (EC and DMC) as they could mask the possible signals of the phosphate phase. The charged and discharged cells were disassembled in a glove-box, where the anode was removed and soaked in methanol to remove traces of the electrolyte solvent and then left to dry. Once dried, the anode was taken out of the glove box where part of the anode material was scraped out and prepared in KBr pellets under ambient conditions.

Figure 5.5 shows the FTIR spectra of the lithiated and delithiated MP400 anode. Initial FTIR spectra analysis showed relatively weak absorption bands owing to the presence of the acetylene black and polytetrafluoroethylene from the teflonized acetylene black binder around spectral region of 600 cm^{-1} and these were of less significant importance therefore the further FTIR spectra analysis were normalized from above 600 cm^{-1} to eliminate these signals. The features in the frequency range from 1300 to 700 cm^{-1} are of greater diagnostic value as they encompass the stretching of PO_3 terminal group and the 'P-O-P' bridge in the pyrophosphate, $\text{P}_2\text{O}_7^{4-}$ anion [63]-[65]. This FTIR analysis could only deduce the existence of phosphate phases whereas the appearance of Sn and Li-Sn alloys are not easily identifiable.

In Figure 5.5 (a), three main bands dominate the spectrum for pristine MP400 anode. Using characteristics frequencies of phosphorous compounds found in literature [63]-[65] the strong band at 742 cm^{-1} can be assigned to the symmetric stretching of bridging P-O-P, $\nu_s(\text{P-O-P})$. The next band at 1007 cm^{-1} is assigned to the symmetric stretching vibration of PO_3 units, $\nu_s(\text{PO}_3)$ [63]-[65]. The narrow band at 1142 cm^{-1} is related to the asymmetric stretching of PO_3 units, $\nu_{as}(\text{PO}_3)$ [63]-[65]. All of these bands are characteristics of the $\text{P}_2\text{O}_7^{4-}$ anion.

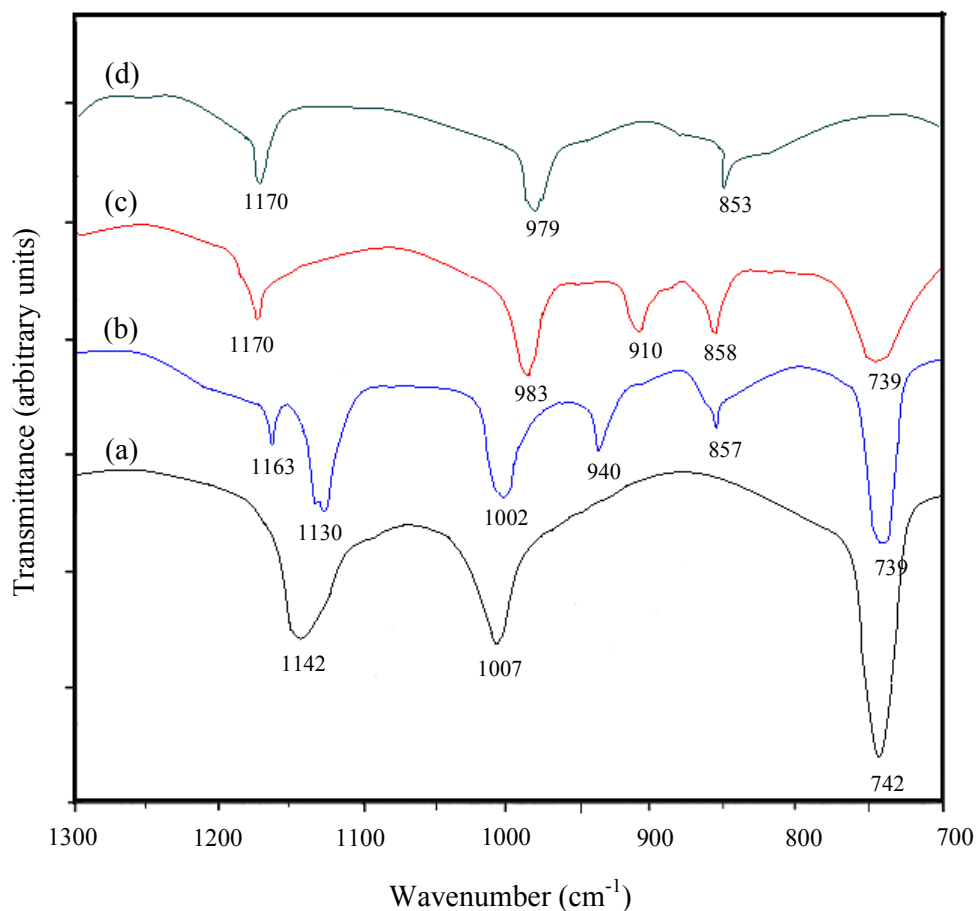


Figure 5.5: FTIR spectra of (a) pristine MP400 anode, (b) MP400 discharged to 1.1 V, (c) MP400 discharge to 0 V and (d) MP400 charged to 2.0 V.

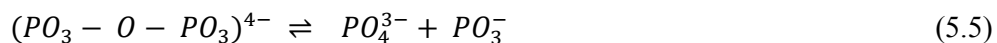
The spectrum for the MP400 anode discharged at 1.1 V can be seen in Figure 5.5 (b). The small, narrow bands at 1163 and 857 cm^{-1} are attributed to traces of lithium alkylcarbonate from the electrolyte residuals that remains in this lithiated MP400 anode [61]. The band around 1130 cm^{-1} exhibited a doublet appearance resulting from the PO_3 vibration split. This doublet appearance may be due to the unequal environments of the PO_3 groups in the anode structure [63] and is assigned to the asymmetric stretching, $\nu_{\text{as}}(\text{PO}_3)$. The bands at 1130 and 1002 cm^{-1} are ascribed to the asymmetric and symmetric stretching of PO_3 units, respectively. They are similar with the bands observed in the spectrum for pristine MP400 at 1142 and 1007 cm^{-1} as

shown in Figure 5.5 (a), except that in this spectrum displayed in Figure 5.5 (b), these bands have reduced intensities and have moved slightly toward the lower frequency upon the progression of the lithiation process. The symmetric stretching, $\nu_s(\text{P-O-P})$ is observed around 739 cm^{-1} [63]-[65]. A new band around 940 cm^{-1} appears for this lithiated MP400 anode. This band is assigned to the symmetric stretching of the PO_4 , $\nu_s(\text{PO}_4)$ [63]-[65]. Based on claims from literatures [7], [25], [36], tin phosphate based anode is said to be reduced to form the lithium phosphate phases (Li_3PO_4 and LiPO_3) and Sn particles upon initial reaction with Li. The changes and presence of bands related to the P-O groups observed in this spectrum is due to the changing of the coordination from $\text{P}_2\text{O}_7^{4-}$ to PO_4^{3-} and PO_3^- . This spectrum showed strong evidence that upon reaction with Li, SnP_2O_7 is reduced to form Li_3PO_4 and LiPO_3 around 1.1 V.

The spectrum for the fully discharged MP400 anode at 0 V is shown in Figure 5.5 (c). Apart from the bands at 1170 and 858 cm^{-1} which are attributed to the lithium alkylcarbonate residuals, there are three bands observed for the phosphate groups at 983 , 910 and 739 cm^{-1} . The band at 983 cm^{-1} was assigned to the symmetric stretching, $\nu_s(\text{PO}_3)$ [63]-[65]. The band at 910 cm^{-1} is ascribed to the symmetric stretching of the PO_4 , $\nu_s(\text{PO}_4)$ [63]-[65]. When these two bands are compared to their identical counterparts in the spectrum shown in Figure 5.5 (b), it was observed that these two bands have moved to the lower frequency region implying a decrease in bond order of the terminal P-O bonds. The symmetric stretching vibration, $\nu_s(\text{P-O-P})$ with a broader band profile remains the same at around 739 cm^{-1} [63]-[65].

The spectrum for the charged MP400 is shown in Figure 5.5 (d). It was observed that the characteristics bands for $\text{P}_2\text{O}_7^{4-}$ anion around 1142 , 1007 and 742 cm^{-1} originally displayed in Figure 5.5 (a) for the pristine MP400, are no longer apparent in the spectrum in Figure 5.5 (d), attesting to the destruction of the $\text{P}_2\text{O}_7^{4-}$ anion upon cycling. This spectrum only exhibited a band around 979 cm^{-1} which was assigned to the symmetric stretching of PO_3^- , $\nu_s(\text{PO}_3)$ [63]-[65]. The bands at 853 and 1170 cm^{-1} are referred to the alkylcarbonate groups from the electrolyte residuals.

To aid explanation on the phosphate phases formed during the electrochemical charging and discharging of the mesoporous SnP_2O_7 anode, interpretations of IR spectral features in the IR investigation on a series of mixed zinc alkali pyrophosphate glasses by A.M. Efimov [65] are applied. The IR spectra were interpreted based on the equilibrium between the $P_2O_7^{4-}$ anions and their disproportion products in the melt during the glass formation. The equilibrium equation is given as below;



For SnP_2O_7 anode, the above equilibrium is shifted to the right when it first reacts with Li. This change in environment is indicated by a decrease in intensity of the 1142 and 1007 cm^{-1} band (PO_3 asymmetric and symmetric stretch, respectively) in the pristine MP400 and its slight shift towards the lower frequency at 1130 and 1002 cm^{-1} as observed in Figure 5.5. (b). Additional evidence for displacing the equilibrium to the right is the appearance of the band at 940 cm^{-1} which is assigned to the symmetric stretching of PO_4 , $\nu_s(PO_4)$. The findings from this FTIR spectrum confirms the analysis made based on cyclic voltammograms and differential capacity plots from sections 5.2 and 5.3 which suggested that upon initial reaction with Li, the $P_2O_7^{4-}$ anion of the SnP_2O_7 anode material is dissociated to form the irreversible Li_3PO_4 and LiPO_3 .

5.5 Comparison on Cycling Behavior between Mesoporous and Non-Mesoporous Tin Phosphate Anodes

The cycling performance of the amorphous, mesoporous SnP_2O_7 anodes (MP200, MP300, MP400 and MP4004) were compared with that of the semi-crystalline and crystalline non-mesoporous SnP_2O_7 (MP500 and TP500) and the graphite anode as well. Graphite is currently the most common anode material used in the commercial Li-ion battery. In this part of the study, the graphite anode was assembled in the same manner as the synthesized SnP_2O_7 anodes, based on a lithium half-cell configuration as described in Chapter 3 (section 3.5).

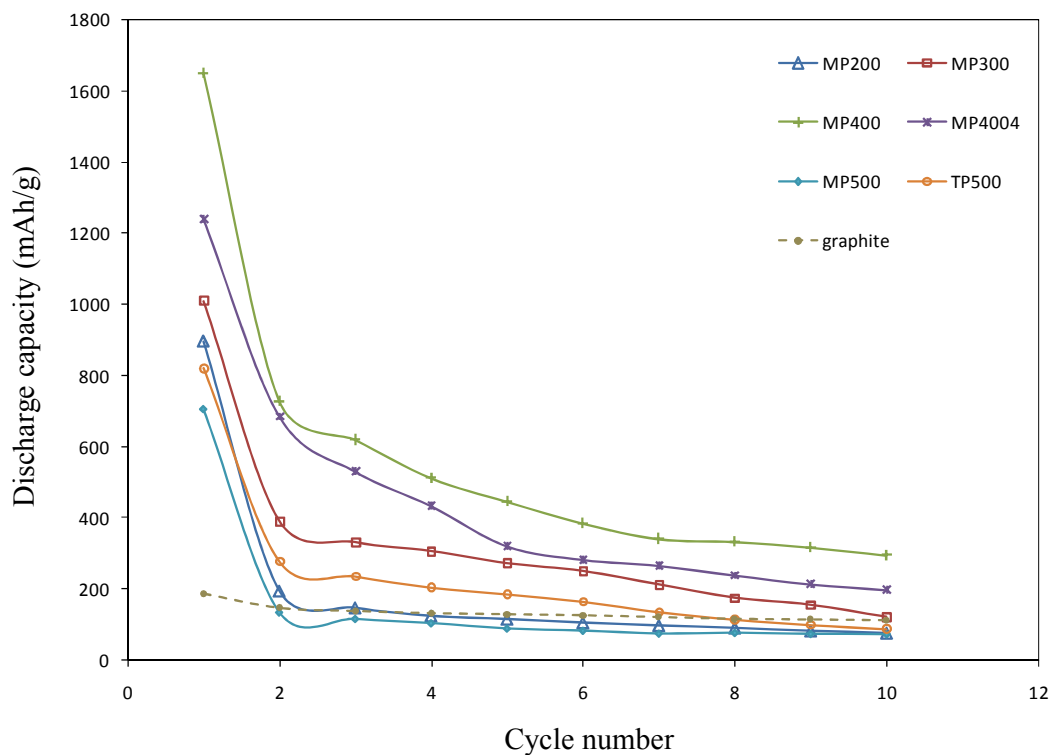


Figure 5.6: Discharge capacity of mesoporous SnP_2O_7 anodes (MP200, MP300, MP400 and MP4004), non-mesoporous SnP_2O_7 anodes (MP500 and TP500) and graphite anode.

Figure 5.6 shows the specific discharge capacities (per gram of active anode material) obtained from the mesoporous and non-mesoporous SnP_2O_7 anodes along with graphite anode, when cycled between 0.0 to 2.0 V with a constant current of 0.5 mA for 10 cycles. Variation in discharge capacity with cycle number for all the anodes tested showed that the best cycling performance with the highest value in discharge capacity was observed for MP400 anode. This was duly followed by MP4004, MP300, graphite, TP500, MP200 and MP500 anodes. Tables 5.2 and 5.3 summarize the discharge and charge capacity collected for all the SnP_2O_7 anodes and the graphite anode from the first to the tenth cycle.

Table 5.2: Discharge and charge capacities for MP200, MP300, MP400 and MP4004 anodes

Cycle no.	MP200		MP300		MP400		MP4004	
	D	C	D	C	D	C	D	C
1	897	182	1010	350	1650	590	1240	508
2	195	145	391	311	728	541	685	498
3	148	110	332	309	620	491	530	407
4	125	99	307	280	512	423	433	381
5	116	92	273	267	446	382	320	311
6	108	88	251	248	385	340	282	270
7	98	82	213	206	341	325	265	233
8	91	77	176	170	333	298	238	204
9	83	71	156	149	317	283	213	185
10	77	68	122	119	295	267	197	179

Table 5.3: Discharge and charge capacities for MP500, TP500 and graphite anodes

Cycle no.	MP500		TP500		Graphite	
	D	C	D	C	D	C
1	705	150	821	275	188	153
2	135	88	278	251	148	145
3	117	83	236	220	139	136
4	105	79	205	194	133	129
5	90	72	186	180	130	127
6	84	68	165	160	127	125
7	76	65	136	135	122	121
8	78	66	115	115	117	116
9	75	65	100	100	115	113
10	74	63	88	78	113	111

The mesoporous SnP_2O_7 (MP400) shows remarkably high initial Li storage capacity of 1650 mAh/g. Both MP400 and MP4004 delivered relatively high reversible charge capacity of 590 mAh/g and 508 mAh/g, respectively when charged to 2.0 V. This shows that the lamellar, mesoporous SnP_2O_7 synthesized could host larger amount of Li^+ in-between their interlayer spacing. The reversible charge capacity in the first cycle indicates how much Li^+ could be extracted from the SnP_2O_7 anodes. All the SnP_2O_7 anodes exhibited enormous loss in irreversible capacities in the first cycle. MP400 anode suffered a loss of 1060 mAh/g in irreversible capacities whereas MP4004 lost about 732 mAh/g. First cycle irreversible capacity losses experienced by MP300 and MP200 are 660 mAh/g and 715 mAh/g whereas non-mesoporous anodes of MP500 and TP500 suffered losses of 555 mAh/g and 546 mAh/g, respectively. A higher Li^+ storage capacity is an indication of additional loss of irreversible capacity. Although the graphite anode delivered low initial discharge capacity of 188 mAh/g when compared to the SnP_2O_7 based anodes, it only

experienced a loss about 35 mAh/g in irreversible capacities in the first cycle as observed from Table 5.3.

The large losses in irreversible capacity in the first cycle are caused by formation of SEI passive film and the reaction between Li and SnP_2O_7 to form irreversible lithium phosphate phases and metallic Sn. As have been discussed earlier in section 5.2-5.3, for amorphous, mesoporous SnP_2O_7 anodes, the irreversible reaction follows the reaction as shown in Equation (5.2) and (5.3). For non-mesoporous, crystalline SnP_2O_7 anodes however, the irreversible reaction takes place according to Equation (5.1). Findings obtained from cyclic voltammograms from Figure 5.1 and 5.2 support that the initial irreversible reduction reaction contributes to large losses in capacity as indicated by the large gap observed between the irreversible peaks in the first cycle with the curves in subsequent cycles. Cyclic voltammogram results also pointed out that electrolyte decomposition on the active anode surface may also add to the first cycle capacity loss. Graphite anodes do not experience large initial losses in irreversible capacities like tin-based anodes because they have different electrochemical reaction mechanism with Li^+ . The working mechanism of graphite anode is based on the intercalation concept whereby Li^+ can be reversibly intercalated and de-intercalated from the graphite host during charging and discharging process and this reaction does not involve formation of irreversible phases [16]. When tin-based anode materials react with Li^+ , they are first reduced to form irreversible phases and their reversible reaction is based on the concept Li_xSn alloying and dealloying [25], [26]. The irreversible losses experienced by graphite anode are due to the formation of the passive SEI film upon interaction with the electrolyte [16]-[18].

Upon further cycling, capacity fading was evident for all the SnP_2O_7 anodes as displayed in Figure 5.6. The reversible discharge capacity gradually decreases from the second cycle to the tenth cycle based on the data shown in Tables 5.2 and 5.3. Upon reaching the 10th cycle, a discharge capacity of 295 mAh/g was retained for MP400. This value is still comparatively higher than that obtained from the other synthesized anodes such as MP200, MP300, MP4004, MP500 and TP500. The graphite anode in this experiment retained about 113 mAh/g upon the 10th cycle with

minimal capacity fading during cycling. Although the graphite anode has a much lower discharge capacity in the first cycle when compared to all the SnP_2O_7 anodes in this experiment, it did not exhibit rapid capacity fading upon reaching the 10th cycle. The stable cycling behavior and low capacity fading rate are the main advantages graphite anodes have over tin-based anode materials [16], [17].

The detrimental effects of tin aggregation on capacity fading shall be explained based on investigations carried by Dahn's group on tin based anode host materials [25], [26], [62]. The discharging and charging process which involves the insertion and extraction of large amount of Li^+ causes the tin based anode host material to expand and contract. This causes volume changes in the host material that induces mechanical stresses which leads to rapid decay in mechanical stability. The anode then suffers from cracking and pulverization, resulting in rapid capacity loss and failure after a few cycles [25], [26]. One potential solution to solve the cracking problem is to embed active tin based anode material in an inactive matrix to buffer volume changes. In this regard, investigation on the electrochemical behaviour of glassy tin based materials ($\text{SnO-B}_2\text{O}_3\text{-P}_2\text{O}_5$) where the glass network formers, $\text{B}_2\text{O}_3\text{-P}_2\text{O}_5$ acts as the inactive matrix was conducted by Dahn *et al.* [62]. Although this investigation has shed light on some aspects of the structural changes during reversible Li insertion and extraction reaction, significant capacity fading upon cycling has been observed. Based on their analysis on the cycled tin oxide composite glasses anode using the ex-situ XRD method, they suggested that the loss of capacity upon cycling with this anode material is associated with the aggregation of Sn atoms to form clusters in the anode material [62]. As the repeated reversible reaction of Li proceeds with the anode, these clusters grow in size resulting in large volume changes. The volume change imparts large mechanical strain on the anode material which can lead to cracking and such morphological changes cause partial disconnection or full disconnection in electrical and ionic contacts between the anode particles [19], [25], [26], [62]. In the latter case, active anode material is lost thus resulting in poor charge-discharge cycling performance. In the glassy ($\text{SnO-B}_2\text{O}_3\text{-P}_2\text{O}_5$) anodes, the atoms other than Sn such as Oxygen (O), Boron (B) and

Phosphorus (P) do not appear to participate in the reversible electrochemical reaction [62]. These atoms that remain inert during the reversible electrochemical redox reaction are known as spectator atoms [62]. The presence of these spectator atoms are said to hinder the motion of Sn particles to form aggregates based on results presented by Dahn *et al.* that showed that the rate of tin aggregation and capacity fade decreases with increasing number of spectator atoms [62]. Tin aggregates slower and into the smaller clusters in anode material with the most number of spectator atoms [62]. This is probably because these spectator atoms form a matrix that disperse tin initially and keeps tin atoms far apart. Thus, the Sn particles have to move over greater distances to aggregate into clusters. However, the increased of spectator atoms will result in lower contents of active Sn particles for the reversible Li-Sn alloying and de-alloying reaction. There is a trade-off between good cyclability and large specific capacity when tin phosphate is used as anode material instead of tin oxide.

Upon initial reaction with Li, the structure of both mesoporous and non-mesoporous SnP_2O_7 anode was altered to form lithium phosphate matrix that dispersed the Sn particles. The lithium phosphate (Li_3PO_4 and LiPO_3) phases formed in the initial cycle were expected to play a similar role as the lithium oxide irreversible phase (Li_2O) in tin oxide systems, namely as a glue that keeps the tin alloy particles mechanically connected and retard aggregation of Sn particles into large agglomerates during large volume changes in alloying and de-alloying [25]. However, it was discovered through this study these matrices alone were not able to minimize the rate of Sn atoms clustering upon further cycling thus resulting in capacity fading.

Other factors that contribute to capacity fading upon cycling are the usage of Li metal as counter electrode which forms dendritic deposition that could contaminate the electrolyte or the break-off of the solid electrolyte interface (SEI) passive film during charge and discharge [66]. Volume changes that cause anode material to crack will be followed by filming of the passive film. Whenever fresh surface of active material gets into contact with the electrolyte new passive film formation takes place and the cracked film is repaired. As a consequence, filming reactions will extend over

a number of cycles and this will cause gradual losses in capacity as Li^+ are consumed irreversibly for this formation [66]. Based on the capacity data for SnP_2O_7 anodes from the second cycle onwards in Tables 5.2 and 5.3, it was noticed that the reversible charge capacity is much lower compared to the discharged capacity of the same cycle. This indicates that not all of the Li^+ inserted for the Li-Sn alloying formation can be efficiently removed during the de-alloying process upon charging to 2.0 V. Some Li^+ are trapped in the structure as Li_xSn alloys (where x is much lower than 4.4) and they remain electrochemically inactive towards further Li reaction. The capacity which can actually be cycled decreases as the remaining amount of active Li^+ for the reversible Li-Sn alloy formation is reduced.

It was mentioned earlier in section 5.2 that the cyclic voltammetric response of all the mesoporous SnP_2O_7 is not influenced by the difference in mesostructure. The cycling performance of the SnP_2O_7 on the other hand was found to be influenced by the structural features of the SnP_2O_7 material. The mesoporous SnP_2O_7 anodes performed averagely better than the non-mesoporous SnP_2O_7 anodes as observed from Tables 5.2 and 5.3. The best charge-discharge performance was contributed by MP400 which delivered the highest capacity. This promising performance is believed to be due to the complex mesostructure from the SDS synthesized SnP_2O_7 that was formed upon calcination at 400°C that enabled this anode material to host a large number of Li^+ during the discharging process and effectively extracting it upon the charging process. The structure of the anode material has an important influence in facilitating the Li^+ insertion and extraction from the anode host material during the discharging and charging process.

5.6 Ex-Situ FESEM Analysis on Cycled Mesoporous and Non-Mesoporous Tin Phosphate Anodes

As discussed in the previous section 5.5 above, the capacity fading observed for both mesoporous and non-mesoporous SnP_2O_7 anodes were attributed to the detrimental effects of Sn aggregates growth during charge-discharge cycling which caused considerable volume changes in the anode that resulted in fragmentation and disintegration of the anode material. The morphologies of the cycled SnP_2O_7 anodes were analyzed in order to substantiate this claim cited in literatures [25], [26], [62], that volume change effects resulting in morphological degradation causes the anode to lose its reversibility and capacity upon further cycling. Ex-situ analysis on the cycled anodes were carried out using FESEM on pristine SnP_2O_7 , SnP_2O_7 anode after one cycle and SnP_2O_7 anode after 10 cycles. Figure 5.7 shows FESEM micrographs magnified at 10,000 times obtained for mesoporous MP400 anodes and Figure 5.8 shows the micrographs for non-mesoporous TP500 anodes.

Both anode material, MP400 and TP500 consist of a mixture of the active anode material and teflonized acetylene black as the conductive binder. The surface morphology of the pristine, uncycled MP400 and TP500 anodes are shown in the FESEM micrographs in Figures 5.7 (a) and 5.8 (a), respectively. Pristine MP400 anode displayed an image of interconnected particles in a porous network whereas TP500 displayed compact, rough surface features.

After both MP400 and TP500 cells were subjected to one cycle of discharging and charging, the cell was disassembled and the anode was taken out and dried before placing under FESEM examination. Ex-situ analysis on MP400 anode surface revealed segregation of particle aggregates with some string-like morphology scattered over the surface as shown in the FESEM image in Figure 5.7 (b). The segregation of aggregates were held further apart in the TP500 anode after one cycle, as observed in the FESEM image in Figure 5.8 (b). The string-like morphology observed for both anodes are ascribed to the crystals of the dried residual electrolyte. The segregation effects for both MP400 and TP 500 are attributed to the formation of

the irreversible lithium phosphates matrices and the after effects of Li^+ extraction upon charging to 2.0 V. The voids and isolation of aggregates are wider for that observed for TP500 anode compared to MP400 anode. This is not desirable since it signifies connectivity loss between particles which is likely to be one of the causes of decreased capacity of the SnP_2O_7 anode upon cycling.

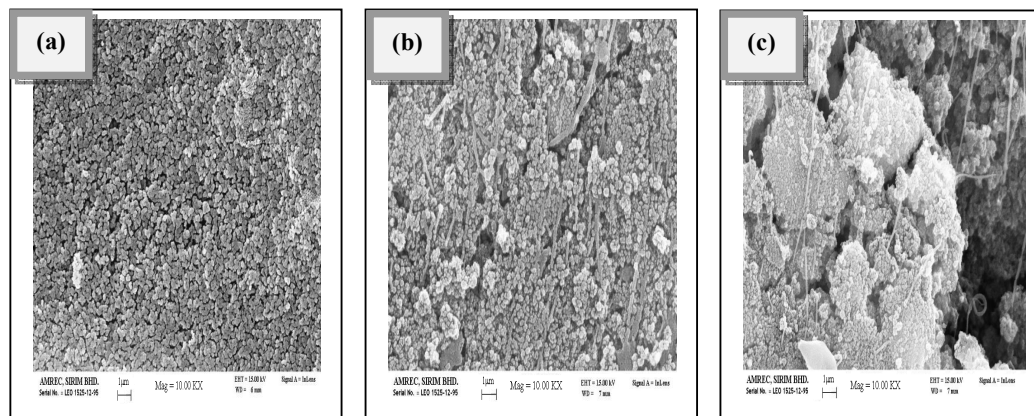


Figure 5.7: FESEM images of MP400 anode (a) before cycling, (b) after 1 cycle and (c) after 10 cycles.

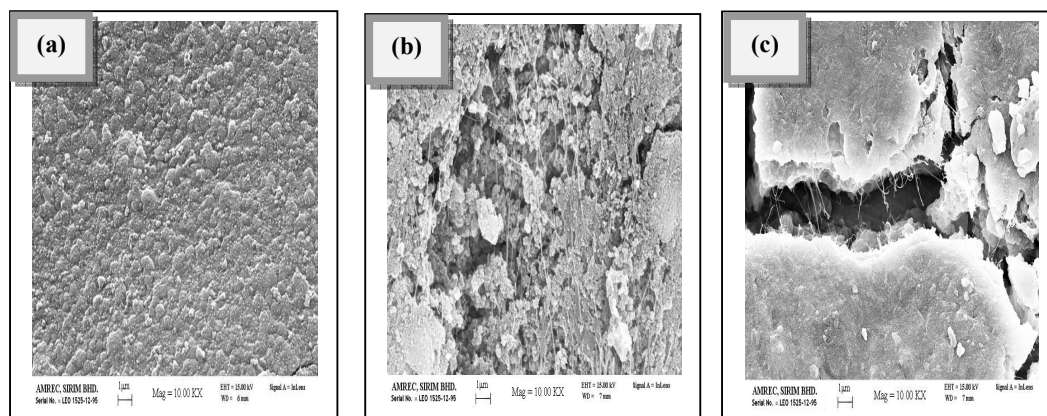


Figure 5.8: FESEM images of TP500 anode (a) before cycling, (b) after 1 cycle and (c) after 10 cycles.

Significant changes were observed on the surface of both anodes cycled up to 10 cycles. The FESEM images revealed micro-cracks for both MP400 and TP500 anodes after 10 cycles, as displayed in Figures 5.7 (c) and 5.8 (c), respectively. The fractures displayed by the cycled TP500 anode was more pronounced and larger by several micrometers thick than that observed for MP400. The fracture propagates in all directions, indicating that the whole expansion and contraction process occurs in three dimensions (x, y and z). The process where Li^+ is inserted into the anode host material causes the bulk structure to expand and upon removal of Li^+ , subsequent contraction follows. During cycling, electrochemically active Sn particles aggregate to form sequentially larger agglomerates which cause the bulk structure to become disproportioned. The repeated cycling process eventually led to cracking and pulverization of the anode material. This morphology degradation causes active Sn particles to become detached electrically and ionically thus resulting in rapid capacity fading. Observation on FESEM images of MP400 powder in section 4.6 from Chapter Four showed that MP400 comprises of nanoparticles of around 30 nm. The cracking and pulverization effects are less extensive in the case of MP400 anode because the nanometer sized cavities within the anode material could absorb some extent of volume changes during cycling.

The ex-situ FESEM analysis on the cycled anodes supports the earlier assumption that the capacity fading upon cycling is due to Sn particles agglomeration that induced undesirable mechanical degradation to the SnP_2O_7 anode. The morphology degradation for MP400 was less extensive when compared to TP500 which explained the higher retention of reversible capacity obtained MP400 as shown in Table 5.2. The mesoporous structure of SnP_2O_7 plays an important role as buffer structures to alleviate large volume changes.

5.7 Effects of Voltage Cutoff on Charge-Discharge Performance of Mesoporous Tin Phosphate Anode

The previous section 5.5 covers the electrochemical behavior of all the fabricated mesoporous and non-mesoporous SnP_2O_7 anode cycled between 0.0 V to 2.0 V. The chosen potential interval is quite large but it provides a good starting point for further experimentation to investigate the effect of different upper voltage cutoff on the charge-discharge performance. It was reported that the reversibility of tin oxide based materials is strongly related to the operating voltage range [25], [26], [62]. For a more focused study, the mesoporous SnP_2O_7 sample MP400 was singled out for charging and discharging tests within different potential range. Three electrochemical cells with MP400 as anode were cycled separately at a constant current of 0.5 mA in three different potential ranges; between 0-1.2 V, 0-1.6 V and 0-2.0 V. Voltage profiles of the three cells for 10 cycles are shown in Figure 5.9.

The initial discharge capacities obtained for the different MP400 cells when discharged from open circuit voltage (OCV) to 0 V showed different values, as observed from Figures 5.9 (a)-(c). The first cell which was discharged from an OCV of 2.97 V to 0 V, delivers an initial capacity of 1418 mAh/, as shown in Figure 5.9 (a). The second cell which was discharged from an OCV of 2.88 V to 0 V exhibited a discharge capacity of 1360 mAh/g as observed from Figure 5.9 (b). Figure 5.9 (c) shows the third cell which was discharged from an OCV of 3.10 V delivers a discharge capacity of 1650 mAh/g. This third cell was the same cell studied in the above Section 5.5. Although all three cells consists of the same MP400 material and were all discharged to 0 V initially, they each have different OCV values and therefore delivered different initial discharge capacity values. The different OCV values are due to ohmic polarization arising from contact between cell casing and anode material and also from the connection between the cell to the battery cycler equipment. The difference in initial specific discharge capacity (per gram of active MP400 material) obtained for all three cells was also caused by some minor difference in active material weight used in fabricating the electrodes. As only a small amount of SnP_2O_7 powder (~ 20 mg) was used to fabricate the anode, it is difficult to

fabricate all the anodes with identical active material weight due to the human factor. The anodes fabricated here have active material weight which varies around 20-22 mg.

This investigation concentrates on the effect of the upper voltage cutoff value on the reversible charge capacity of the MP400 anodes. Subsequent Li^+ extraction reaction of the first cell up to 1.2 V returned a reversible charge capacity 580 mAh/g, as observed from Figure 5.9 (a). The second cell when charged to 1.6 V exhibited a reversible capacity of 480 mAh/g as observed from Figure 5.9 (b). Upon charging to 2.0 V, the third cell showed a reversible charge capacity of 590 mAh/g indicated in Figure 5.9 (c). Although the reversible capacity of the third cell is near to that obtained for the first cell charged to 1.2 V, the loss experienced by the third cell is greater. Irreversible capacity losses here refer to the difference between Li^+ insertion capacity during discharging with the Li^+ extraction capacity during charging. The first cell experienced irreversible losses of about 848 mAh/g (59.4%) whereas the third showed losses about 1060 mAh/g (64.2%). The second cell charged to 1.6 V experienced first cycle losses of about 880 mAh/g (64.7%). The causes that contribute to the first cycle losses have been discussed extensively in the above sections 5.2, 5.3 and 5.5.

For clarity of presentation in this discussion, the corresponding discharge capacities computed from the voltage profile shown in Figure 5.9 is plotted versus cycle number, as shown in Figure 5.10. The capacities of the first cycle were not plotted here because it contains a large part in irreversible capacities associated with the initial irreversible formation of the passive film and lithium phosphate matrix that is irrelevant in investigating the effect of upper voltage cutoff value on the reversibility of the mesoporous SnP_2O_7 anode.

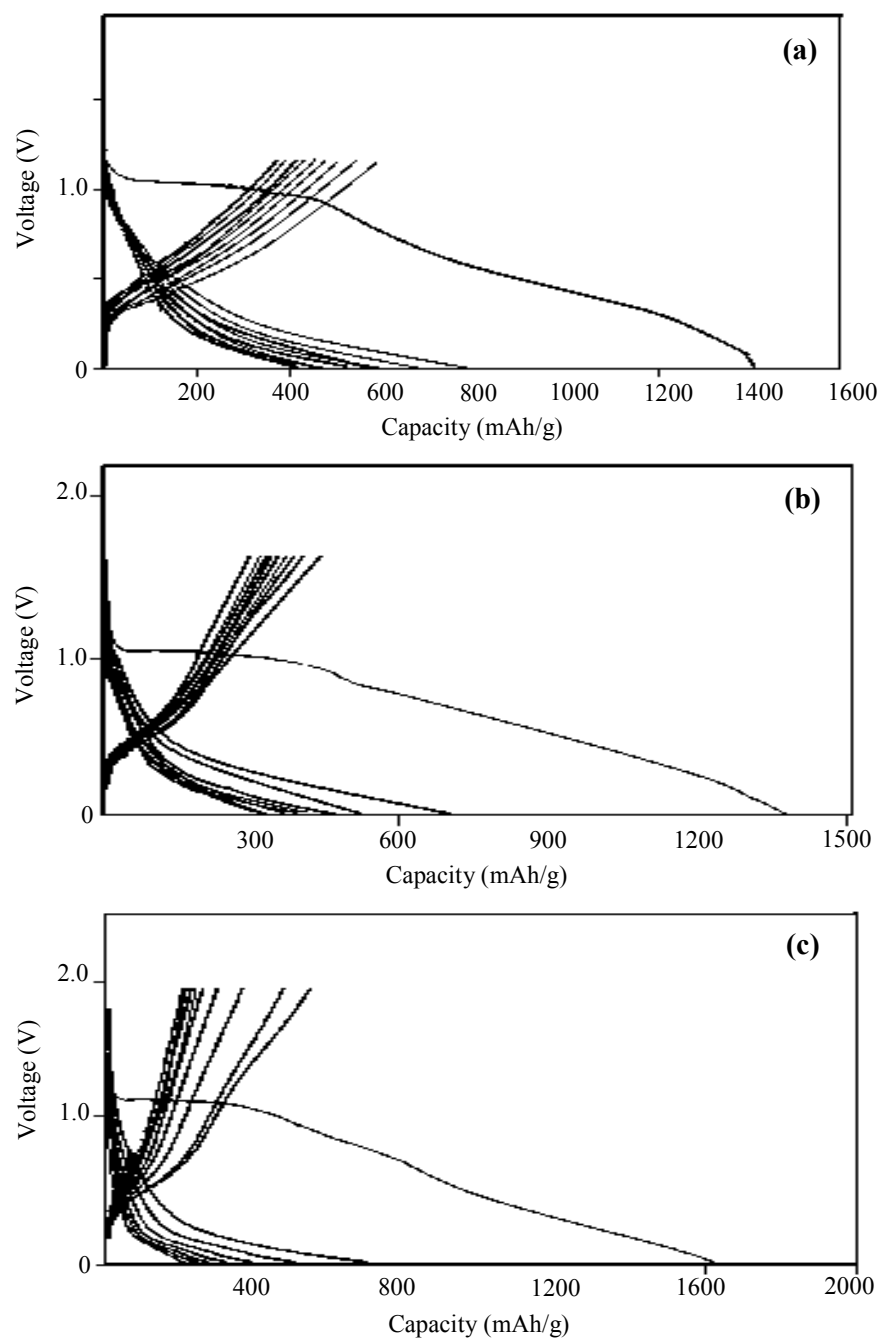


Figure 5.9: Voltage profile for MP400 cycled between (a) 0-1.2 V, (b) 0-1.6 V and (c) 0-2.0 V.

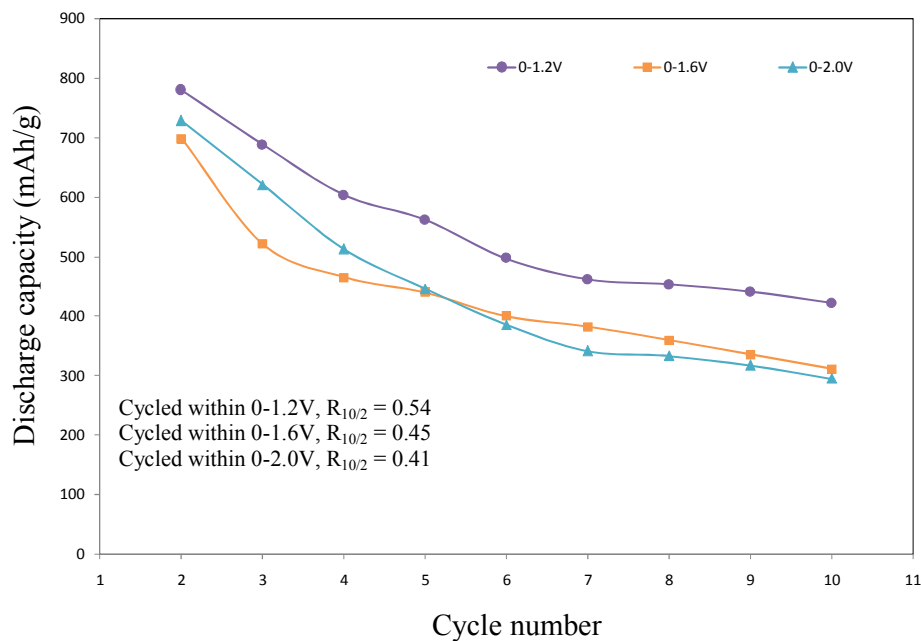


Figure 5.10: Discharge capacity vs. cycle number of MP400 anode cycled between 0-1.2V, 0-1.6 V and 0-2.0 V. $R_{10/2}$ denotes the capacity retention index.

As observed from this Figure 5.10, there is noticeable difference in the decrease of discharge capacities with increasing cycle number, for the three cells that were cycled within potential range. A capacity retention index, $R_{10/2}$ shall be used herein to help quantify the cycling stability of the cells cycled within different potential range. $R_{10/2}$ is defined as the ratio of discharge capacity from the tenth cycle to the capacity of second cycle, as depicted below;

$$\text{Capacity Retention Index, } R_{10/2} = \frac{\text{Tenth cycle discharge capacity}}{\text{Second cycle discharge capacity}} \quad (5.6)$$

Cells that cycled efficiently should therefore have $R_{10/2}$ equals to one. When MP400 was cycled within 0-1.2 V, the $R_{10/2}$ obtained was 0.54 whereas for that cycled within 0-1.6 V has a $R_{10/2}$ of 0.45. The MP400 cycled between 0 to 2.0 V has a $R_{10/2}$ of 0.41, which is the lowest of all three cells cycled. Despite exhibiting relatively high reversible discharge capacity upon the second cycle, this cell displayed rapid capacity fading upon reaching the 10th cycle. These results indicate that the mesoporous SnP_2O_7 anode is quite sensitive to potential limits of cycling, with too wide a voltage

region leading to more rapid capacity fading. When the cells are cycled for complete removal of Li^+ at higher upper voltage cutoff, they displayed unstable cycle behavior. The unstable cycle behavior is ascribed to the aggregation of tin clusters which deteriorates the discharge characteristics as the cycle number increases. Differential plots are sensitive detectors for changes in the voltage profiles from cycle to cycle and the constancy of the plots is indicative of good reversibility of the anode material in repetitive charge and discharge operations. In order to analyse the cell's performance and the influence of upper voltage cutoff on aggregation of Sn particles during cycling, differential capacity plots of the cells cycled within the different potential range were constructed based on the second and tenth charge-discharge cycle data, as shown in Figure 5.11.

Differential capacity plot for the second cycle for MP400 cycled within 0-1.2 V showed a broad discharge peak around 0.15 V indicative of the existence of Li-Sn alloy phases but when the anode reaches the tenth cycle, the peak has a jagged feature, as observed from Figures 5.11 (a) and (a'). The smoother peak in the second discharge cycle indicates the Sn particles are finely dispersed in the Li_3PO_4 and LiPO_3 matrices whereas the rougher peak profile upon the tenth cycle indicates the Sn particles has formed aggregates. The formation of aggregates implies a fade in capacity. The differential capacity plot at the tenth cycle for the cell cycled within 0-2.0 V as shown in Figure 5.11(c') displayed more pronounced disordered peak profile when compared to the differential capacity plot at the tenth cycle for cell cycled within 0-1.2 V and 0-1.6 V, as depicted in Figures 5.11 (a') and (b'), respectively. These peaks indicate rapid aggregation of metallic Sn clusters. The higher voltage cutoff of 2.0 V certainly accelerated this process. Disordered peak profile was observed for the cell cycled within 0-1.6 V, although they were not developed as chaotic as that noticed for the cell cycled within 0-2.0 V. It appears that the peaks are the sharpest when the upper voltage cutoff is higher. The capacity fade of MP400 is the most rapid when cycled between 0 V to 2.0 V. The strong peaks in differential plots are undesirable since they indicate phase changes. These changes are caused by the aggregation of tin atoms into larger and larger clusters with cycle number. As

regions of tin clusters grow larger, bulk Li-Sn alloy phases will begin to form and the coexistence regions between them will be observed as strong peaks in the differential capacity [25], [26], [62]. Coexistence of bulk Li-Sn alloy phases within the same particles creates a phase boundary between adjacent phases which have different crystal structures and Li:Sn ratios [25], [26], [62]. As a result, regions within a particle become detached (electrically and ionically) and become inactive as a lithium alloy material [25], [26], [62]. The fragmentation of the alloy based anode materials is believed to be the source of poor reversibility.

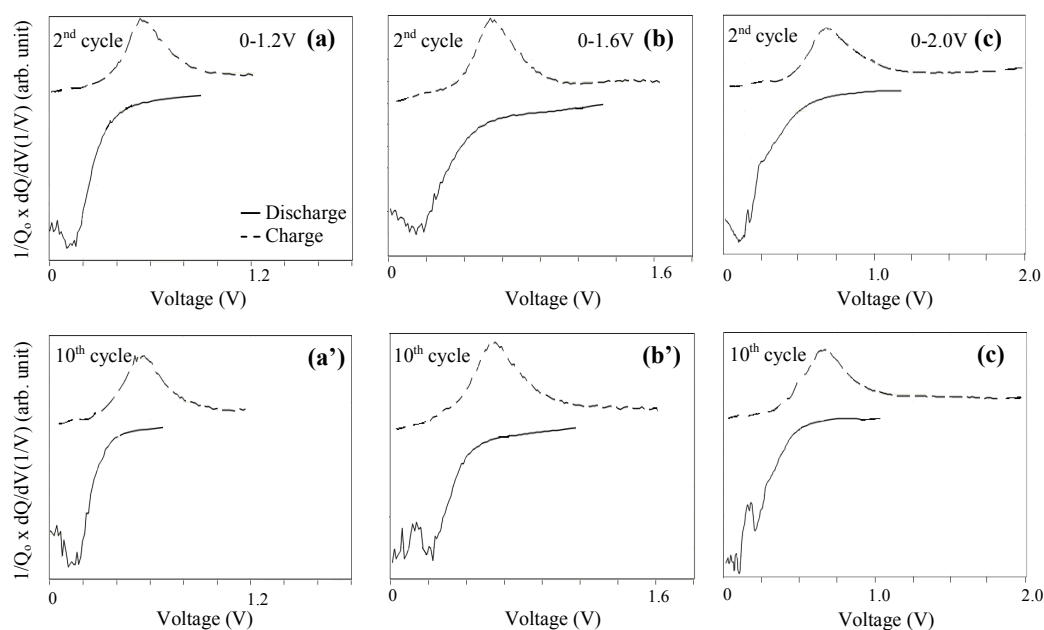


Figure 5.11: Differential capacity plots of MP400 cycled within specified voltage range; (a) 2nd cycle (0-1.2V), (a') 10th cycle (0-1.2V); (b) 2nd cycle (0-1.6V), (b') 10th cycle (0-1.6V) and; (c) 2nd cycle (0-2.0V) and (c') 10th cycle (0-2.0V).

The cycling performance of the mesoporous SnP_2O_7 is sensitive to the choice of voltage limit. Good cycling behavior with stable differential capacity plots was obtained if the voltage was cutoff at 1.2 V. When the voltage cutoff was raised to 1.6 V or 2.0 V, additional peaks appeared in the differential capacity plots. The more abrupt changes in the differential capacity plots are the results of increased aggregation of tin. The aggregation would cause fragmentation and crack propagation in the material leading to eventual capacity losses. It was reported for tin oxide based anodes that at potential cutoff higher than 1.5 V have caused reformation of unalloyed Sn and the destruction of the Li_2O matrix which results in the loss of protection against volume changes in the charge and discharge [25]. The reformation of Sn particles creates problems because Sn is ductile and has a low melting point, suggesting good atomic mobility at room temperature [25]. By contrast, the Li-Sn alloy phases all have higher melting point than Sn and are more brittle [25]. Thus, charging to the limit of metallic tin (> 1.2 V) may aid the Sn aggregation process. Once the aggregates grew too large, two coexisting phase regions are observed, along with volume mismatch resulting in capacity fade [25]. These are the factors that contribute to the rapid decrease in cyclability and poor capacity retention of MP400 anodes cycled between 0 to 2.0 V.

5.8 Cycling Profile of Mesoporous Tin Phosphate Anode

As discussed in section 5.7, capacity fading was least significant when MP400 was cycled within the potential limit of 0 - 1.2 V. Galvanostatic cycling test was extended up to 50 cycles for MP400 in order to obtain an overview on the charge-discharge performance of mesoporous SnP_2O_7 anodes upon prolonged cycles. Dependence of Coulombic efficiency on cycle number was also analyzed in this section. The cycling profile of the MP400 as represented by the charge-discharge capacity and Coulombic efficiency versus cycle graph is shown in Figure 5.12. For clarity of presentation only the first ten cycles plus every fifth cycle onwards till the 50th cycle were shown in this figure.

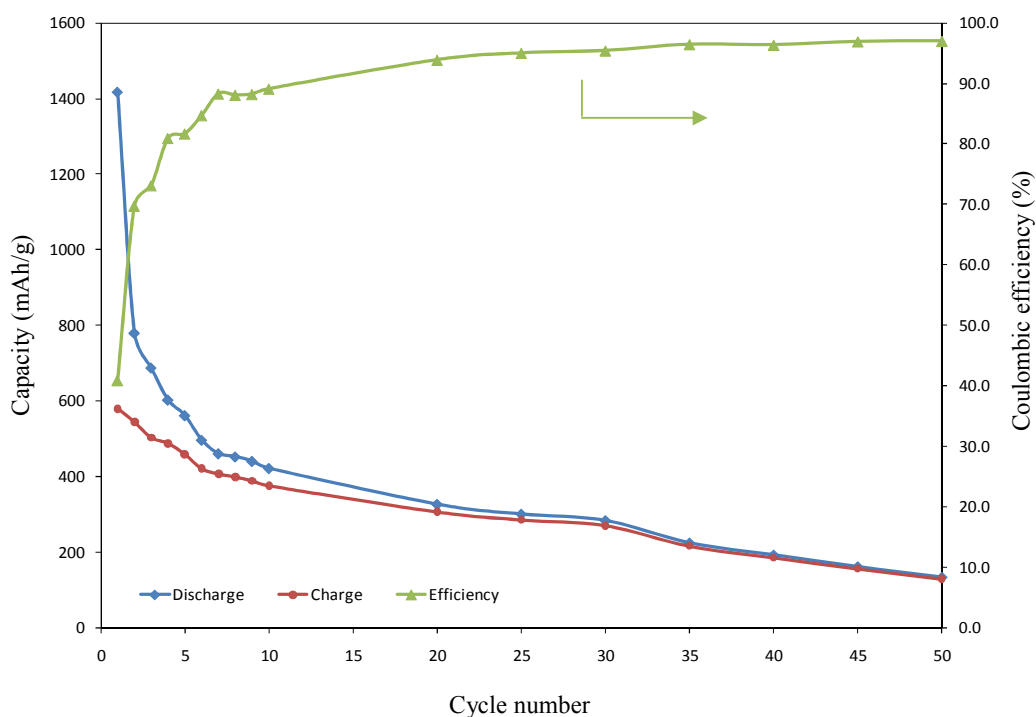


Figure 5.12: Charge-discharge capacity and Coulombic efficiency versus cycle number for MP400 cycled within 0-1.2 V.

Coulombic efficiency is the ratio of charge capacity over discharge capacity of the same cycle. The initial discharge capacity obtained for this MP400 sample was 1418 mAh/g which decreases to 580 mAh/g upon charging to 1.2 V. The corresponding Coulombic efficiency of this first cycle was about 41 %. Large losses in the first cycle are attributed to passive film formation and reduction of SnP_2O_7 to form irreversible lithium phosphate matrices (Li_3PO_4 and LiPO_3) and metallic Sn. The discharge capacity obtained from the second cycle at 780 mAh/g was observed to decrease at a significant rate until it reaches the 7th cycle with a discharge capacity of 461 mAh/g. From the 8th cycle onwards, the rate of capacity fading has become slower and stabilizes after the 35th cycle. Rate of capacity fading upon cycling is related to tin aggregation effects as discussed earlier. However, after a certain number of cycles, the growth of tin aggregates into clusters appears to reach a saturated size. It has been proposed that the clusters grow until cluster-cluster separation reaches a distance over which motion of tin atoms can no longer be supported [62]. When this stage is reached, the capacity fading rate becomes much slower. Referring to Figure 5.12, this mesoporous SnP_2O_7 anode retained a Li^+ storage capacity of 134 mAh/g upon reaching the 50th cycle. The charge capacity obtained at the 50th cycle was 130 mAh/g, which is very close to the discharge capacity value. In contrast to the gradual decrease of capacity with increasing cycle, the Coulombic efficiency improves from the second cycle onwards at 70% right up to the 50th cycle at 97%. The efficiencies become near constant after the 20th cycle. This shows that the mesoporous SnP_2O_7 anode exhibited excellent reversibility from the 20th cycle onwards however, at the expense of reduced capacities values.

The lower discharge capacity at prolonged cycles is also related to the decreased amount of active Li^+ for the Li-Sn alloying reaction. Apart from the initial lost of Li^+ that was consumed to form the irreversible SEI passive film and lithium phosphate matrices (Li_3PO_4 and LiPO_3), Li^+ was also continuously lost during formation of new SEI films when the old films crack due to volume change resulting from the growth of tin clusters during cycling. Upon charging process, it was noticed not all of the inserted Li^+ can be efficiently extracted out and this further reduces the capacity

during cycling. A prolonged duration is consumed for galvanostatic cycling at higher cycles and this eventually led to the depletion of Li^+ supply from the electrolyte for the reversible electrochemical Li-Sn alloying and de-alloying reaction. All these factors discussed above when combined will lead to the eventual failure of this anode upon prolonged cycling conditions

5.9 Summary

Cyclic voltammetry measurements were carried out on mesoporous and non-mesoporous SnP_2O_7 samples to detect irreversible and reversible reactions. Upon reaction with Li, there were irreversible and reversible reactions identified in cyclic voltammograms. The irreversible reactions were ascribed to the formation of the SEI passive film and the reduction of SnP_2O_7 to produce irreversible lithium phosphate (Li_3PO_4 and LiPO_3) phases whereas the reversible reaction is ascribed to the alloying and dealloying of Li-Sn. The galvanostatic experiments clearly demonstrate that the electrochemical performance of SnP_2O_7 anodes is influenced by their morphological features. The mesoporous SnP_2O_7 (MP400) displayed the best electrochemical performance when compared to other mesoporous and non-mesoporous anode cycled within 0 - 2.0 V as it retained comparatively higher discharge capacity of 295 mAh/g upon reaching the 10th cycle. Capacity fading upon cycling was attributed to effects of Sn particles aggregation to form larger clusters that caused volume changes which eventually led to the disintegration of the anode material. This effect was observed to be less extensive in mesoporous SnP_2O_7 anodes. The cycling performance of the mesoporous SnP_2O_7 is sensitive to the choice of voltage limit. When the cells are cycled for complete removal of Li at higher upper voltage cutoff, they displayed unstable cycling behavior. When MP400 was cycled within 0 - 1.2 V, it retained a discharge capacity of 134 mAh/g upon reaching the 50th cycle.

CHAPTER 6

STRUCTURAL INFLUENCE OF MESOPOROUS TIN PHOSPHATE ON ITS ELECTROCHEMICAL PROPERTIES

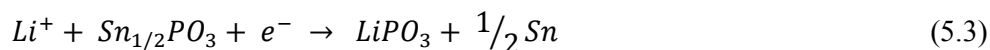
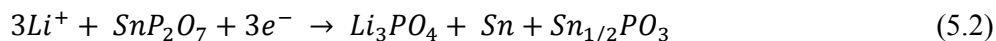
6.1 Overview

In Chapter 5, based on the galvanostatic cycling performance of the mesoporous and non-mesoporous SnP_2O_7 anodes, it can be deduced that the structural features the SnP_2O_7 anode has a distinctive influence on its charge-discharge cycling performance. The mesoporous SnP_2O_7 anodes performed averagely better than the non-mesoporous SnP_2O_7 anodes yielding higher reversible capacity upon prolonged cycles. This chapter correlates the electrochemical properties discussed in Chapter 5 with the structural features of the synthesized SnP_2O_7 as discussed in Chapter 4. The crystallographic and porosity features of both mesoporous and non-mesoporous SnP_2O_7 anodes are related to their corresponding electrochemical performance results to determine the influence of the structural feature. Results obtained for amorphous, mesoporous SnP_2O_7 anode (MP200, MP300, MP400 and MP4004) are compared with that obtained for the non-mesoporous SnP_2O_7 anodes (semi-crystalline MP500 and the crystalline TP500) to highlight the advantages of the mesoporous SnP_2O_7 anode.

6.2 Crystallographic Features and the Electrochemical Properties of the Tin Phosphate Anodes

Based on the XRD patterns obtained in Chapter 4 (section 4.4), the SDS synthesized SnP_2O_7 powders that were calcined at 200, 300 and 400°C displayed mesostructure characteristics based on the presence of a single low angle reflections of (100) around $2\theta = 1.6^\circ$. These mesostructured SnP_2O_7 powders (MP200, MP300, MP400 and MP4004) are largely amorphous as no obvious peaks were observed in the wide angle diffraction patterns ($2\theta = 10-80^\circ$). Prolonged calcination duration resulted in reduced ordering along with a slight contraction in the mesostructure as observed in the XRD patterns for SDS synthesized SnP_2O_7 calcined at 400°C for 2 hours and for 4 hours (MP400 and MP4004). When this powder was fired at 500°C, the mesoporous structure collapsed due to complete decomposition of the SDS surfactant. The powder calcined at 500°C (MP500) did not display any obvious mesoporous characteristics instead it exhibited a mixed crystalline and amorphous phase based on its wide angle XRD pattern as shown in Figure 4.4. The non-SDS synthesized SnP_2O_7 on the other hand, produced non-mesoporous powders. The non-mesoporous SnP_2O_7 powders showed increased degree of crystallinity when calcination temperature was increased. The powder calcined at 500°C (TP500) has the highest degree of crystallinity in this batch.

The electrochemical reaction of SnP_2O_7 with Li first involves the irreversible reduction of SnP_2O_7 to form lithium phosphate phases and metallic tin. The tin particles further react with Li based on the reversible reaction of Li_xSn alloying and dealloying reaction.



Based on analysis from Chapter 5 (sections 5.2 and 5.3), the two irreversible SnP_2O_7 reactions expressed in Equations 5.2 and 5.3 were observed to occur for the mesoporous SnP_2O_7 anodes (MP200, MP300, MP400 and MP4004) and the semi-crystalline SnP_2O_7 anode (MP500). In the initial reaction of these anodes with Li, the SnP_2O_7 is partially reduced to form the unstable $\text{Sn}_{0.5}\text{PO}_3$ phase as shown in Equation 5.2. Further reaction with Li causes the unstable $\text{Sn}_{0.5}\text{PO}_3$ phase to be reduced to Sn particles and lithium phosphate phase, as expressed in Equation 5.3. Although MP200, MP300, MP400, MP4004 and MP500 anodes have different microstructures, they all exhibited similar electrochemical reactions with Li. The common structural feature that they all share is the presence of the amorphous phase. Amorphous materials are generally characterized by their random orientation of atoms or molecules [44]. The complex order of the amorphous phase in mesoporous SnP_2O_7 anodes was assumed to provide more than one energetically active sites for reaction with Li to occur during the electrochemical reaction within the specified potential limit of 0 - 2.0 V. The residual amorphous structure of the MP500 anode may be responsible in providing the extra energetic environment for the reduction of SnP_2O_7 . Based on results obtained from Chapter 5 (sections 5.2 and 5.3) for TP500, the reduction of non-mesoporous SnP_2O_7 occurred as expressed in Equation 5.1. The difference in voltammetric response of the TP500 when compared to that of the MP200, MP300, MP400, MP4004 and MP500 anodes as observed from Figures 5.3 and 5.4, is believed to be due to their different crystallographic features. Crystalline materials as opposed to amorphous material have fixed geometric arrangements of atoms or molecules [44]. The crystalline TP500 has only one energetic site for reaction with Li whereas the other SnP_2O_7 anodes in comparison have two active sites. The cyclic voltammogram profile for the crystalline TP500 is similar with that obtained by Behm and Irvine [36] in their work on crystalline SnP_2O_7 synthesized via a solid state reaction.

6.3 Mesoporous Morphology and the Electrochemical Properties of the Tin Phosphate Anodes

The mesoporous SnP_2O_7 powders produced in this study consist of spherical particles in an array that contains periodic nanopores as indicated by morphological analysis by means of physisorption technique and FESEM in Chapter 4 (sections 4.5 and 4.6). Galvanostatic charge discharge tests in Chapter 5 (section 5.5) revealed the potential of mesoporous SnP_2O_7 as a superior Li^+ storage host material due to its higher discharge capacity when compared to the non-mesoporous SnP_2O_7 and the commercial graphite anode used in Li-ion batteries.

Based on the initial charge and discharge capacities shown in Table 5.1, the mesoporous SnP_2O_7 anodes delivered relatively higher capacities when compared to the non-mesoporous anode, MP500 and TP500. For the MP300, MP400 and MP4004 anodes, the equivalent moles of Li^+ (x) to form the Li_xSn alloy are higher than the theoretical stoichiometry of $\text{Li}_{4.4}\text{Sn}$ proposed by Courtney and Dahn [25]. The initial discharge capacities of these mesoporous SnP_2O_7 anodes were higher than the theoretical capacity of SnP_2O_7 at 993 mAh/g. The non-mesoporous anodes, MP500 and TP500 however delivered lower initial discharge capacities than the theoretical capacity value. The mesoporous anodes in this study even delivered higher initial discharge capacity than the crystalline, cubic SnP_2O_7 anode produced by Behm and Irvine [36] via a solid state reaction method at 936 mAh/g. Mesoporous SnP_2O_7 have larger surface areas than the non-mesoporous SnP_2O_7 and the larger surface areas provide increased Li reaction sites which explain the enormous discharge capacity delivered by these anodes.

The capacities for the mesoporous and non-mesoporous SnP_2O_7 and graphite anode tabulated in Tables 5.2 and 5.3 for 10 cycles showed that MP400 has the best cycling performance. Upon the 10th cycle, MP400 retained a discharge capacity of 197 mAh/g whereas TP500 only retained that of 88 mAh/g and graphite retained about 113 mAh/g in discharge capacity. The pore sizes determined for MP200, MP300, MP400 and MP4004 based on the BJH method reported in Chapter 4 (section

4.5) are 10.6, 13.5, 15.8 and 17.9 nm, respectively. Relating this pore size data with the cycling behaviour of the mesoporous SnP_2O_7 anodes observed in Figure 5.6 and the tabulated data in Tables 5.2 and 5.3, revealed that discharge capacity retention tends to increase with increasing pore size, except for the case of sample MP4004. Despite having the smallest average pore size and the largest surface area as shown in Table 4.1 and 4.2, MP200 showed the worst capacity retention upon the 10th cycle. It can be deduced that the smaller pores of the synthesized mesoporous SnP_2O_7 have thicker pore wall dimensions and this provides a pathway that enable easier Sn particle migration to form aggregates thus resulting in connectivity losses and significant capacity fading during cycling. For sample MP4004, XRD results from Chapter Four (section 4.4), suggests that this SnP_2O_7 mesostructure experienced a slight contraction in the mesostructure when fired at 400°C for a prolonged duration of 4 hours. The disrupted order in the interconnectivity of the porous network for MP4004 may have affected the ability of this anode to retained higher reversible capacity during cycling. This indicates that the design of the mesostructure attained during the synthesis of the mesoporous SnP_2O_7 is critical in determining improved electrochemical performance of the SnP_2O_7 anode during charge-discharge cycling.

It was reported that the reversibility of tin-based anode materials is related to the grain size of the starting material [19]-[21]. In tin-based anode materials with very fine particle size, even large changes of dimensions of the crystal structure due to repeated insertion or removal of Li^+ will not necessary cause cracks and pulverization, as absolute changes in particle dimensions are still small [19]-[21]. The diffusion path length for Li^+ insertion and charge-transfer resistance of the anode material is decreased in nanoparticles [19]-[21]. The faster diffusion of Li^+ delivers higher value of reversible capacity. Observations made based on FESEM images in Chapter Four (section 4.6) showed that the synthesized mesoporous SnP_2O_7 anode composed of loose clusters of nanoparticles with an average size of around 30 nm whereas non-mesoporous SnP_2O_7 consists of larger particle size of 0.2 μm . In line with this, the nanoparticles that make-up the mesoporous SnP_2O_7 anode are thought to also play a

role in preserving better capacity and reversibility when compared to the rapid capacity fading of larger sized particles of non-mesoporous SnP_2O_7 anode.

Capacity fading for both mesoporous and non-mesoporous SnP_2O_7 anodes are associated with aggregation of Sn particles to form larger clusters that causes volume change which eventually led to the disintegration of the anode material. This effect was observed to be less extensive in mesoporous SnP_2O_7 anodes as evidenced by the galvanostatic charge-discharge results and the ex-situ FESEM analysis on the cycled anodes in Chapter 5 (sections 5.5 and 5.6). The ability of mesostructured SnP_2O_7 anode to store high amount of Li^+ and retain higher reversible capacity is attributed to its complex mesostructured network which was believed to be able to facilitate diffusion of Li^+ and maintain high dispersion of Sn particle in the anode. Sn particles are dispersed far apart in the matrix of mesoporous anode therefore the migration of Sn particles to form aggregates was made slower. Another interesting property shown by the mesoporous SnP_2O_7 anode material is its ability to accommodate the volume change effects. The lamellar and porous structure can undergo reversible swelling during the repeated insertion and extraction of Li^+ process. This reduces the extent of anode material fragmentation by minimizing mechanical strain effects thus improving the reversibility of this anode material. It was reported that the mesoporous framework was able to dissipate the mechanical stress induced by the volume changes during the Li_xSn alloying and de-alloying reactions through reversible pore expansion and contraction mechanism [42], [51], [67]. During the discharging process, Li^+ are electrochemically inserted into the mesopores and this causes the structure to be slightly expanded and upon charging, the extraction of Li^+ resulted in the contraction of the mesoporous anode structure [42], [51], [67]. It is likely that the mesopores act as a mechanical buffer and effectively prevent the electrical disconnection between active materials induced by the volume expansion during electrochemical reactions. This mechanism reduces the extent of volume change effects that cause disintegration of the anode material upon prolonged charge discharge cycling.

Despite the added advantages, there is one major drawback observed for the mesoporous SnP_2O_7 anodes which is the colossal losses in irreversible capacity when compared to non-mesoporous SnP_2O_7 anodes. The high surface area of the mesoporous SnP_2O_7 results in extensive formation of the SEI passive film and this contributes to large initial irreversible capacity losses. During extended charge-discharge cycling, the strain from volume changes become significant enough to crack the old SEI films and this causes new SEI filming to take place. This in turn causes excessive losses in irreversible capacity during cycling.

The non-mesoporous anodes, MP500 and TP500 displayed large losses in reversible capacity upon cycling. This may be associated with its crystalline structure as this ordered structure may present a path where Sn atoms can easily migrate and gather in one plane thus facilitating formation of larger tin aggregates. These large tin clusters will in turn result in massive volume change effects that lead to formation of electrically disconnected parts thus leading to rapid capacity fading upon cycling.

6.4 Summary

The amorphous, mesoporous SnP_2O_7 and the semi-crystalline SnP_2O_7 anodes have two energetic environments for reactions with Li whereas the crystalline SnP_2O_7 has only one energetic site. The structural feature of SnP_2O_7 anode material has a strong influence on its electrochemical performance. The success of mesoporous anode in comparison with the non-mesoporous anode is that the lamellar, mesostructure of the starting anode material manages to minimize migration of Sn particles to form aggregates while it still allows transport of Li^+ and electrons, thereby retaining higher capacity. The mesopores are able to accommodate volume changes during the Li^+ insertion and extraction process and this result in less extensive mechanical degradation on the SnP_2O_7 anode structure upon prolonged cycles when compared to the non-porous SnP_2O_7 anode. Based on this study, it was observed that the mesoporous SnP_2O_7 anode with the smallest pore size and the largest surface area

does not necessarily delivers the best charge-discharge cycling behaviour. It is critical to achieve a specific mesostructure during the synthesis to produce a mesoporous SnP_2O_7 anode that not only delivers higher discharge capacity but also manages to retain high capacity upon prolonged cycling. In this study it was discovered the MP400 anode with an average pore size distribution of 15.8 nm delivered the highest discharge capacity of 197 mAh/g upon the 10th cycle.

CHAPTER 7

CONCLUSION

7.1 Review of Study

This thesis reports the electrochemical behavior of a lamellar, mesoporous tin (IV) phosphate (SnP_2O_7) as anode material for Li-ion battery. The mesoporous SnP_2O_7 was synthesized via surfactant templating method where sodium dodecyl sulfate (SDS) was applied as the surfactant. Amorphous, mesoporous structure was successfully obtained when the powders were calcined at 200, 300 and 400°C however when fired up to 500°C, the mesoporous structure collapses as indicated by XRD analysis. For reference purpose, another batch of tin phosphate was synthesized without the SDS surfactant. This yielded non-mesoporous SnP_2O_7 powders which presented crystalline structure with increasing calcination temperature. Isotherms of Type IV were obtained from nitrogen sorption measurement, which further confirms the mesoporous characteristics of SDS synthesized SnP_2O_7 powders calcined at 200, 300 and 400°C. The mean pore size of the mesoporous SnP_2O_7 calcined at 200 (MP200), 300 (MP300) and 400°C (MP400) for 2 hours and that calcined at 400°C (MP4004) for 4 hours was 10.6, 13.5, 15.8 and 17.9 nm, respectively, as calculated based on the Barrett-Joyner-Halenda (BJH) model. The mean pore size increases with increasing calcine temperature. Data and discussions on the structural and morphological properties of mesoporous SnP_2O_7 analyzed by means of TG-DTA, XRD, nitrogen sorption and FESEM are extensively covered in Chapter Four.

The core study of this research is presented in Chapter Five which investigates the electrochemical behavior of mesoporous SnP_2O_7 . It was proposed that initial reaction of SnP_2O_7 with Li causes the SnP_2O_7 to be reduced to form the irreversible LiPO_3 and Li_3PO_4 phases and metallic Sn. The Sn atoms dispersed in the LiPO_3 and Li_3PO_4 matrices are hosts for further reversible alloying and de-alloying reaction of Li-Sn. Cyclic voltammetry measurements carried out on all the mesoporous SnP_2O_7 samples exhibited similar voltammetric responses. Three irreversible reactions were identified during the initial potential scan which were attributed to formation of the solid electrolyte interface (SEI) passive film on the anode surface and the reduction of SnP_2O_7 to produce irreversible lithium phosphate (Li_3PO_4 and LiPO_3) phases. The non-mesoporous, crystalline SnP_2O_7 only showed two irreversible reactions attributing to the formation of the SEI and lithium phosphate phases. This implies that the amorphous, mesoporous SnP_2O_7 structure may have more energetically active site for lithium ions reaction. Both mesoporous and non-mesoporous SnP_2O_7 showed similar reversible redox reactions potential at around 0.18 V and 0.52 which are assigned to the reversible alloying and de-alloying of Li_xSn (where $x \leq 4.4$). FTIR analysis carried out on discharged and charged MP400 anode showed dissociation of $\text{P}_2\text{O}_7^{4-}$ during the insertion of Li^+ into the SnP_2O_7 host and formation of irreversible lithium phosphate phases.

Galvanostatic cycling tests carried out on all the mesoporous SnP_2O_7 samples along with the non-mesoporous SnP_2O_7 showed that MP400 has the best performance. The cycling performance of the mesoporous SnP_2O_7 is sensitive to the choice of voltage limit. When the cells are cycled for complete removal of Li at higher upper voltage cutoff, they displayed unstable cycle behavior. Good cycling behavior with stable differential capacity plots was obtained if the voltage was cutoff at 1.2 V; when the potential cutoff was raised to 1.6 or 2.0 V, cycling performance deteriorates and additional peaks appeared in the differential capacity plots. The abrupt changes in the differential capacity plots are the results of increased aggregation of Sn particles. The aggregation would cause fragmentation and crack propagation in the material leading to eventual capacity losses. Galvanostatic cycling of MP400 within 0 - 1.2 V up to the

10th cycle returned a reversible discharge capacity of 422 mAh/g whereas that cycled within 0 - 1.6 V and 0 -2.0 V delivered reversible discharge capacity of 311 mAh/g and 295 mAh/g, respectively. When the MP400 anode was further cycled up to the 50th cycle within 0 - 1.2 V, it retained a discharge capacity of 134 mAh/g. Apart from the detrimental effects of Sn particles aggregation, capacity fading at prolonged cycles was also attributed to the decreased amount of active Li⁺ for the Li-Sn alloying reaction. Li⁺ are lost during the formation of the SEI film and lithium phosphate matrixes and also during the insertion process where some Li⁺ remains trapped in the mesoporous anode structure.

Overall, the good reversibility observed for the mesoporous SnP₂O₇ anode is related to the porous network, the operating voltage range, particle size and inactive matrix. The ability of mesostructured tin phosphate anode to store much higher amount of Li⁺ when compared to non-mesoporous SnP₂O₇ was attributed to its complex mesostructured network that provided larger surface area for reactions with Li. The mesoporous network proved to be more effective in preventing large scale aggregation and is able to accommodate large volume changes during the Li insertion and extraction process, thus retaining higher reversible discharge capacity. A lower cutoff in the upper voltage is able to retard the aggregation of Sn particles. The application of nanoparticles and the lithium phosphate matrices can further minimize the growth of Sn aggregates thereby reducing the saturated size of Sn clusters that could lead to severe cracking and crumbling of the SnP₂O₇ anode.

7.2 Suggestions for Future Studies

Research on mesoporous tin phosphate as alternative anode material for Li-ion battery is still in its early days. There are a few aspects that should be explored to fully understand the electrochemical reaction mechanism of SnP_2O_7 based anode. Some of these are suggested below;

- The SnP_2O_7 anode materials have only been galvanostatically cycled in half cell configuration, against metallic Li as counter electrodes. Further studies are needed on the whole cell where the mesoporous SnP_2O_7 is cycled against a lithium transition metal oxide, cathode material.
- Several question marks remain in determining the exact electrochemical reaction mechanism of the mesoporous SnP_2O_7 anode material. Several other sophisticated techniques such as the Mossbauer spectroscopy, nuclear magnetic resonance (NMR) and small-angle x-ray scattering (SAXS) could be used in combination with electrochemical measurements to ascertain the mechanism of Li insertion and extraction.
- The scope of this thesis has been to investigate the electrochemical properties of the mesoporous SnP_2O_7 anode but the surface chemistries remain unexplored. It is crucial to understand the active surface reaction with electrolyte species in order to reduce irreversible capacities upon cycling. Detailed FTIR studies combined with electrochemical impedance spectroscopy (EIS) would be of great importance in understanding the surface reactions and the irreversible reactions occurring in these systems.

REFERENCES

- [1] M. Winter and R.J. Brook, "What are Batteries, Fuel Cells, and Supercapacitors?," *Chem. Rev.*, vol. 104, pp. 4245-4269, 2003.
- [2] J.M. Tarascon and M. Armand, "Issues and Challenges Facing Rechargeable Lithium Batteries," *Nature*, vol. 414, pp. 359-367, 2001.
- [3] Rechargeable Battery. http://en.wikipedia.org/wiki/Rechargeable_battery
- [4] D. Linden and T.B. Reddy, Eds., *Handbook of Batteries*, 3rd ed., New York: McGraw-Hill, 2001, pp. 22.3-22.24.
- [5] Advanced Storage Battery Market: From Hybrid/Electrical Vehicles to Cell Phones. <http://www.mindbranch.com/Advanced-Rechargeable-battery-R460-205/>
- [6] G.A. Nazri and G. Pistoia, Eds., *Lithium Batteries Science and Technology*, USA: Kluwer, 2003, pp. 88-180.
- [7] Y.W. Xiao, J.Y. Lee, A.S. Yu and Z.L. Liu, "Electrochemical Performance of Amorphous and Crystalline $\text{Sn}_2\text{P}_2\text{O}_7$ Anodes in Secondary Lithium Batteries," *J. Electrochem. Soc.*, vol. 146, no. 10, pp. 3623-3629, 1999.
- [8] M.S. Whittingham, "Electrical Energy Storage and Intercalation Chemistry," *Science*, vol. 192, no. 4244, pp. 1126-1127, 1976.
- [9] J.O. Besenhard and H.P. Fritz, "Cathodic Reduction of Graphite in Organic Solution of Alkali and NR_4^+ Salt," *J. Electroanal. Chem.*, vol 53, pp. 329-333, 1974.
- [10] M. Lazzari and B. Scrosati, "A Cyclable Lithium Organic Electrolyte Cell based on Two Intercalation Electrodes," *J. Electrochem. Soc.*, vol. 127, no. 3, pp.773-774, 1980.
- [11] S. Basu, "Ambient Temperature Rechargeable Battery," U. S. Patent 4,423,125, December 27, 1983.

- [12] T. Nagaura and K. Tozawa, "Lithium Ion Rechargeable Battery," *Prog. Batt. Solar Cells*, vol. 9, pp. 209, 1990.
- [13] M. Armand, J.M. Chabagno and J.M. Duclot, "Poly-ethers as Solid Electrolytes," in *Proc. Fast Ion Transport in Solids Electrodes and Electrolytes Conf.* Amsterdam, North Holland, 1976, pp. 131-136.
- [14] I.E. Kelly, J.R. Owen and B.H. Steel, "Poly(ethyleneoxide) Electrolytes for Operation at Near Room Temperature," *J. Power Sources*, vol. 14, pp.13-21, 1985.
- [15] J.M. Tarascon, A.S. Gozdz, C. Schmutz, F. Shokoohi and P.C. Warren, "Performance of Bellcore's Plastic Rechargeable Li-ion Batteries," *Solid State Ionics*, vol. 86-88, pp. 49-54, 1996.
- [16] Schematic diagram of graphite structure. <http://www.tutorvista.com/content/science/science-ii/carbon-compounds/allotropes-carbon.php>
- [17] S. Flandrois and B. Simon, "Carbon Materials for Lithium-ion Rechargeable Batteries," *Carbon*, vol. 37, pp. 165-180, 1999.
- [18] J.O. Besenhard and M. Winter, "Insertion Reactions in Advanced Electrochemical Energy Storage," *Pure & App. Chem.*, vol. 70, no. 3, pp. 603-608, 1998.
- [19] M. Winter and J.O. Besenhard, "Electrochemical Lithiation of Tin and Tin-based Intermetallics and Composites, *Electrochim. Acta*, vol. 45, pp. 31-50, 1999.
- [20] J. Yang, M. Winter and J.O. Besenhard, "Small Particle Size Multiphase Li-Alloy Anodes for Li-ion Batteries," *Solid State Ionics*, vol. 90, pp. 281-287, 1996.
- [21] J.O. Besenhard, J. Yang and M. Winter, "Will Advanced Lithium-Alloy Anodes Have a Chance in Lithium-ion Batteries?" *J. Power Sources*, vol. 68, pp. 87-90, 1997.
- [22] B.A. Boukamp, G.C. Lesh and R.A. Huggins, "All-Solid Lithium Electrodes with Mixed-Conductor Matrix," *J. Electrochem. Soc.*, vol. 128, pp. 725-729, 1981.

- [23] Y. Idota, "Nonaqueous Secondary Battery," U. S. Patent 5,478,671, November 11, 1997.
- [24] Y. Idota, T. Kubota, A. Matsufuji, Y. Maekawa and T. Miyasaka, "Tin-Based Amorphous Oxide: A High-Capacity Lithium-Ion-Storage Material," *Science*, vol. 276, pp. 1395-1397, 1997.
- [25] I.A. Courtney and J.R. Dahn, "Electrochemical and In Situ X-Ray Diffraction Studies of the Reaction of Lithium with Tin Oxide Composites," *J. Electrochem. Soc.*, vol. 144, pp. 2045-2052, 1997.
- [26] I.A. Courtney and J.R. Dahn, "Key Factors Controlling the Reversibility of the Reaction of Lithium with SnO₂ and Sn₂BPO Glass," *J. Electrochem. Soc.*, vol. 144, pp. 2943-2948, 1997.
- [27] Sony Press Release. <http://www.sony.net/SonyInfo/News/Press/200502/05-006E>
- [28] O. Mao, R.A. Dunlap and J.R. Dahn, "Mechanically Alloyed Sn-Fe(-C) Powders as Anode Materials for Li-Ion Batteries I. The Sn₂Fe-C System," *J. Electrochem. Soc.*, vol. 146, pp. 405-413, 1999.
- [29] O. Mao and J.R. Dahn, "Mechanically Alloyed Sn-Fe(-C) Powders as Anode Materials for Li-Ion Batteries II. The Sn-Fe System," *J. Electrochem. Soc.*, vol. 146, pp. 414-427, 1999.
- [30] K.D. Kepler, J.T. Vaughey and M.M. Thackeray, "Li_xCu₆Sn₅ (0<x<13): An Intermetallic Insertion Electrode for Rechargeable Lithium Batteries," *Electrochem. Solid-State Lett.*, vol. 2, no.7, pp. 307-309, 1999.
- [31] K.D. Kepler, J.T. Vaughey and M.M. Thackeray, "Copper-Tin Anodes for Rechargeable Lithium Batteries: An Example of the Matrix Effect in an Intermetallic System," *J. Power Sources*, vol. 81-82, pp. 383-387, 1999.
- [32] J. Yang, M. Wachtler, M. Winter and J.O. Besenhard. Sub-Microcrystalline Sn and Sn-SnSb Powders as Lithium Storage Materials for Lithium-Ion Batteries," *Electrochem. Solid-State Lett.*, vol. 2, no. 4, pp. 161-163, 1999.
- [33] I. Rom, M. Wachtler, I. Papst, M. Schmied, J.O. Besenhard, F. Hofer and M. Winter, "Electron Microscopical Characterization of Sn/SnSb Composite

- Electrodes for Lithium-ion Batteries,” *Solid State Ionics*, vol. 143, pp. 329-336, 2001.
- [34] K. Wan, S.F.Y. Li, Z.Q. Gao and K.S. Siow, “Tin-Based Oxide Anode for Lithium-ion Batteries with Low Irreversible Capacity,” *J. Power Sources*, vol. 75, pp. 9-12, 1998.
- [35] F.J.F. Madrigal, C.P. Vicente and J.L. Tirado, “On the Structure and Electrochemical Reactions with Lithium of Tin (II) Phosphate Chloride,” *J. Electrochem. Soc.*, vol. 147, no. 5, pp. 1663-1667, 2000.
- [36] M. Behm and J.T.S. Irvine, “Influence of Structure and Composition Upon Performance of Tin Phosphate Based Negative Electrodes for Lithium Batteries,” *Electrochim. Acta*, vol. 47, pp. 1727-1738., 2002.
- [37] K.S.W. Sing, “Reporting Physisorption Data for Gas/Solid Systems with Special Reference to the Determination of Surface Area and Porosity,” *Pure & Appl. Phys.*, vol. 57, pp. 603-619, 1985.
- [38] C.T. Kresge, M.E. Leonowicz, W.J. Roth, J.C. Vartuli and J.S. Beck, “Ordered Mesoporous Molecular Sieves Synthesized by a Liquid-Crystal Template Mechanism,” *Nature*, vol. 359, pp. 710-712., 1992.
- [39] A. Huczko, “Template-Based Synthesis of Nanomaterials,” *Appl. Phys. A*, vol. 70, pp. 365-376, 2000.
- [40] P.D. Yang, D.Y. Zhao, D.I. Margolese, B.F. Chmelka and G.D. Stucky. “Generalized Syntheses of Large-Pore Mesoporous Metal Oxides with Semicrystalline Frameworks,” *Nature*, vol. 396, pp. 152-155, 1988.
- [41] H. Yang, X.Y. He and M.H. Cao, “Microemulsion-Mediated Solvothermal Synthesis of Tin (IV) Hydrogen Phosphate Rose-Like Three Dimensional Nanostructures and Their Electrochemical Properties,” *Mater. Res. Bull.*, vol. 44, no. 3, pp. 509-514, 2009.
- [42] E. Kim, D. Son, T.G. Kim, J. Cho, B. Park, K.S. Ryu and S.H. Chang, “A Mesoporous/Crystalline Composite Material Containing Tin Phosphate for Use as the Anode in Lithium-Ion Batteries, *Angew. Chem. Int. Ed.*, vol. 43, pp.5987-5990, 2004.

- [43] C. Velásquez, F. Rojas, V.H. Lara and A. Campero, "On the Textural and Morphological Properties of Crystalline and Amorphous α -Tin Phosphate," *Phys. Chem. Chem. Phys.*, vol. 6, pp.4714-4721, 2004
- [44] C. Giacobazzo, H. Monaco, D. Viterbo, F. Scordari, G. Gilli, G. Zanotti and M. Catti, Eds., *Fundamentals of Crystallography*, Oxford University Press, USA, 1992.
- [45] C.R. Brundle, C.A. Evans Jr. and S. Wilson, Eds., Imaging Techniques (Microscopy), *Encyclopedia of Materials Characterization: Surfaces, Interfaces, Thin Films*. Butterworth-Heinemann, Greenwich, 1992
- [46] J. Rouquerol, D. Avnir, C.W. Fairbridge, D.H. Everett, J.H. Haynes, N. Pernicone, J.D.F. Ramsay, K.S.W. Sing and K.K. Unger, "Recommendations for the Characterization of Porous Solids," *Pure & Appl. Chem.*, vol. 66, pp. 1739-1758, 1994.
- [47] Gas Sorption Process.
http://www.quantachrome.com/pdf_brochures/07101.pdf
- [48] Handbook of Analytical Methods for Materials-Fourier Transform Infrared Spectroscopy. <http://mee-inc.com/ftir.html>
- [49] A.J. Bard and L.R. Faulkner. *Electrochemical Methods: Fundamentals and Applications*, 2nd ed., John Wiley and Sons Inc, USA, 2000, pp. 156-255.
- [50] C.L. Bianchi, S. Ardizzone and G. Cappelletti, "Nanocrystalline Oxides: Surfactants-Assisted Growth," *Dekker Encyclopedia of Nanoscience and Nanotechnology*, CRC Press, New York, 2004, pp. 1-10.
- [51] M. Tiemann and M. Froba, "Mesostructured Aluminophosphates Synthesized with Supramolecular Structure Directors," *Chem. Mater.*, vol. 13, pp. 3211-3217, 2001.
- [52] C. Serre, A. Auroux, A. Gervasini, M. Hervieu and G. Férey, "Hexagonal and Cubic Thermally Stable Mesoporous Tin (IV) Phosphates with Acidic and Catalytic Properties," *Angew. Chem. Int. Ed.*, vol. 41, no. 9, pp. 1594-1597, 2002.
- [53] Q. Huo, D.I. Margolese, U. Ciesla, P. Feng, T.E. Gier, P. Sieger, R. Leon, P.M. Petroff, F. Schuth and G.D. Stucky, "Generalized Synthesis of Periodic

- Surfactant/Inorganic Composite Materials,” *Nature*, vol. 368, pp. 317-321, 1994.
- [54] Q. Huo, D.I. Margolese, U. Ciesla, P. Feng, T.E. Gier, P. Sieger, A. Firouzi, B.F. Chmelka, F. Schuth and G.D. Stucky, “Organization of Organic Molecules with Inorganic Molecular Species into Nanocomposite Biphase Arrays,” *Chem. Mater.*, vol. 6, no. 8, pp. 1176-1198, 1994.
- [55] A. I. Bortun, S. A. Khainakov, L. N. Bortun, E. Jaimez, J. R. García and A. Clearfield, “Synthesis and Characterization of a Novel Layered Tin (IV) Phosphate with Ion Exchange Properties,” *Mater. Res. Bull.*, vol. 34, no. 6, pp. 921-932, 1999.
- [56] W.W. Wendlandt and L.W. Collins, Eds., *Thermal Analysis*, vol. 2. Stroudsburg, Pennsylvania: Dowden, Hutchinson & Ross Inc., 1976, pp. 152-155.
- [57] J. M. Patterson, Z. Kortylewicz and W.T. Smith Jr, “Thermal Degradation of Sodium Dodecyl Sulfate,” *J. Agric. Food Chem.*, vol. 32, pp. 782-784, 1984.
- [58] L. Körösi, S. Papp, V. Meynen, P. Cool, E. F. Vansant & I. Dékány, “Preparation and Characterization of SnO₂ Nanoparticles of Enhanced Thermal Stability: The Effect of Phosphoric Acid treatment on SnO₂.nH₂O,” *Colloids and Surfaces A: Physicochem. Eng. Aspects*, vol. 268, pp. 147-154, 2005.
- [59] D.H. Chen, Z. Li, Y. Wan, X.J. Tu, Y.F. Shi, Z.X. Chen, W. Shen, C.Z. Yu, B. Tu and D.Y. Zhao, “Anionic Surfactant induced Mesophase Transformation to Synthesize highly ordered Large Pore Mesoporous Silica Structures,” *J. Mater. Chem.*, vol. 16, pp. 1511-1519, 2006.
- [60] E. Kim, Y. Kim, M.G. Kim and J.Cho, “Elimination of Extraneous Irreversible Capacity in Mesoporous Tin Phosphate Anode by Amorphous Carbon Coating,” *Electrochem. Solid-State Lett.*, vol. 9, no. 3, pp. A156-A159, 2006.
- [61] J.Z. Li, H. Li, Z.X. Wang, X.J. Huang and L.Q. Chen, “The Interaction between SnO Anode and Electrolytes,” *J. Power Sources*, vol. 81-82, pp. 346-351, 1999.

- [62] I.A. Courtney, W.R. McKinnon and J.R. Dahn, "On the Aggregation of Tin in SnO Composite Glasses Caused by the Reversible reaction with Lithium," *J. Electrochem. Soc.*, vol. 146, no. 1, pp. 59-68, 1999.
- [63] P.S. Attidekou, P.A. Connor, P. Wormald, D.P. Tunstall, S.M. Francis and J.T.S. Irvine, "Solid State Studies of Phosphate/Tin Matrix Formed on Electrochemical Insertion into SnP_2O_7 ," *Solid State Ionics*, vol. 175, pp. 185-190, 2004.
- [64] M. Gabelica-Robert, "Infrared Spectrum of Crystalline and Glassy Pyrophosphates: Preservation of the Pyrophosphate Group in the Glassy Structure," *J. Molecular Struct.*, vol. 79, pp. 251-254., 1982.
- [65] A.M. Efimov, "IR Fundamental Spectra and Structure of Pyrophosphate Glasses along the $2\text{ZnO} \cdot \text{P}_2\text{O}_5$ - $2\text{Me}_2\text{O} \cdot \text{P}_2\text{O}_5$ Join (Me being Na and Li)," *J. Non-Cryst. Solids*, vol. 209, no. 3, pp. 209-226, 1997.
- [66] M. Wachtler, J.O. Besenhard and M. Winter., "Tin and Tin-Based Intermetallics as New Anode Materials for Lithium-Ion Cells," *J. Power Sources*, vol. 94, pp. 189-193, 2001.
- [67] H. Kim, G.S. Park, E. Kim, J. Kim, S.G. Doo and J. Cho, "Observation of Reversible Pore Change in Mesoporous Tin Phosphate Anode Material during Li Alloying/Dealloying," *J. Electrochem. Soc.*, vol. 153, no. 9, pp. A1633-A1636, 2006.